STRUCTURAL AND RNA-BINDING CHARACTERISTICS OF THREE YEAST LA MOTIF DOMAINS

EVAN PACHECO

A THESIS SUBMITTED TO THE FACULTY OF GRADUATE STUDIES IN PARTIAL FULFILLMENT OF THE REQUIREMENTS

FOR THE DEGREE OF

MASTER OF SCIENCE

GRADUATE PROGRAM IN BIOLOGY

YORK UNIVERSITY

TORONTO, ONTARIO

AUGUST 2025

ABSTRACT

La-related proteins (LARP) are a conserved class of RNA-binding proteins that function in RNA metabolism, including mRNA stabilization, translation regulation, and non-coding RNA processing. In humans, La-related protein 1 (LARP1) regulates translation and stability of 5′ terminal oligopyrimidine (TOP) tract-containing mRNAs linked to cell growth and proliferation. Although its role as a downstream effector of the mTORC1 pathway is established, the molecular interactions of LARP1 and yeast homologs remain poorly defined. This thesis examines the structure–function relationship of the La motif domain (LaM) in yeast proteins Slr1p, Slf1p, and Sro9p using isothermal titration calorimetry (ITC), circular dichroism (CD), nuclear magnetic resonance (NMR), and differential scanning calorimetry (DSC). Findings show these proteins share conserved features and bind RNA and ligands with high affinity (low micromolar K_d). NMR line broadening observed for Slf1p–RNA interactions suggests conformational sampling. Collectively, these results advance understanding of conserved mechanisms underlying LARP1-mediated translational regulation.

ACKNOWLEDGEMENTS

Completing this thesis has been a rewarding journey, and I am deeply grateful to the many individuals who supported, inspired, and guided me along the way.

First and foremost, I would like to express my sincerest gratitude to my supervisor, Dr. Logan Donaldson, for being an exceptional mentor, teacher, and researcher. Your unwavering dedication to excellence, insightful guidance, and patience have shaped not only this project but also my growth as a scientist. The lessons you've taught me, both in and out of the lab, will stay with me throughout my career and life.

I am thankful for Dr. Bayfield's advice and insight early on in this project, with the helpful progress meetings. I am also immensely thankful to Dr. Yi Sheng, Dr. Georg Zoidl, and Dr. Phillip Johnson for their invaluable willingness to support my research and for joining my committee, which has been instrumental in bringing this work to completion.

A special thanks to my dear friend Tatiana, Dr. Nirusha Thavarajah, and Dr. Lana Mikhaylichenko, whose passion for lab work and research ignited my own enthusiasm for scientific discovery. Your belief in setting ambitious goals, no matter how daunting, has been a constant source of motivation.

I owe a tremendous debt of gratitude to Dr. Aron Shoara, whose expertise in DSC, ITC, and countless other techniques was the backbone of this thesis. Your patience, generosity, and problem-solving brilliance were indispensable. To Emily Hoi Pui Chao, thank you for your kindness and critical assistance with the Ap4a ITC experiments; your contributions were invaluable.

Finally, none of this would have been possible without the unconditional love and support of my parents. Your encouragement, wisdom, and belief in me have shaped the person I am today. Thank you for always standing by my decisions and pushing me to reach higher.

This journey has been a collective effort, and I am forever grateful to everyone who played a part in it.

TABLE OF CONTENTS

LIST OF FIGURES

LIST OF TABLES

LIST OF ABBREVIATIONS

4E-BP	Eukaryotic translation initiation factor 4E
4E-BP1	Eukaryotic translation initiation factor 4E-binding protein 1
5'-TOPs	5’ Terminal oligopyrimidine
α	Alpha
Å	Angstrom
ANN	Artificial neural network
Ap4a	Di-adenosine tetra phosphate
β	Beta
BLAST	Basic local alignment search tool
FFT	Fast Fourier transform
CEST	Chemical exchange saturation transfer
CD	Circular dichroism
CSP	Chemical shift perturbation
DEST	Dark-state exchange saturation transfer
DNA	Deoxyribonucleic acid
DMSO	Dimethyl sulfoxide
DSC	Differential scanning calorimetry
eIF3I	Eukaryotic translation initiation factor 3 subunit 1
eIF4F	Eukaryotic initiation factor 4F
eIF4G	Eukaryotic translation initiation factor 4G
EDTA	Ethylenediaminetetraacetic acid
EMT	Epithelial-mesenchymal transition
ER	Endoplasmic reticulum
ε	Extinction coefficient
hLARP1	Human La-related protein
HMQC	Heteronuclear multiple quantum coherence
HSQC	Heteronuclear single quantum coherence
IDR	Intrinsically disordered regions
IMAC	Immobilized metal affinity chromatography
IPTG	Isopropyl β-D-thiogalactopyranoside
ITC	Isothermal titration calorimetry
K_d	Equilibrium dissociation constant
K_{on}	Association rate constant
K_{off}	Dissociation rate constant
kDa	Kilo Dalton
LARP	La-related protein
LaM	La motif
LB	Lysogeny broth
m7G	7-methylguanosine
MRE	Mean residue ellipticity
MRI	Magnetic resonance imaging

mRNA	Messenger RNA
mTOR	Mammalian target of rapamycin
mTORC1	Mammalian target of rapamycin complex 1
MW	Molar weight
MWCO	Molecular weight cut off
NADPH	Nicotinamide adenine dinucleotide phosphate
NMR	Nuclear magnetic resonance
NOE	Nuclear Overhauser effect
NOESY	Nuclear Overhauser effect spectroscopy
OD_{600nm}	Optical density at 600 nanometers
ORF	Open reading frame
PABP	Poly A binding protein
PAM2w	Poly A binding protein interacting motif 2
PAR-CLIP	Photoactivatable ribonucleoside-enhanced crosslinking and immunoprecipitation
PBS	Phosphate buffered saline
pI	Isoelectric point
pLDDT	Predicted local distance difference test
ppm	Parts per million
φ	Phi
ψ	Psi
Ras-MAPK	Rat sarcoma Mitogen Activated Protein Kinase
RMSD	Root mean square deviation
RNA	Ribonucleic acid
rpm	Revolution per minute
RRM	RNA-Recognition motif
ROS	Reactive oxygen species
SEC	Size exclusion chromatography
STRIDE	Structural identification
TALOS+	Torsion angle likeliness obtained from shift and sequence similarity
Tm	Melting Temperature
TOCSY	Total correlation spectroscopy
Tris	Tris(hydroxymethyl)aminomethane
UTR	Untranslated region
V	Volt
ΔG	Change in Gibbs free energy
ΔH	Change in enthalpy
ΔS	Change in entropy

1. INTRODUCTION

1.1 Introduction to the La-Related Protein (LARP) Family

Almost all eukaryotes share a class of RNA-binding proteins called La-related proteins (LARPs). Characterized by a modular domain organization, LARPs play essential roles in RNA maturation, processing, and regulation. Based on their structural and functional features, they are classified into five main subgroups: LARP1, LARP3 (also known as La), LARP4, LARP6, and LARP7. (Bousquet-Antonelli & Deragon, 2009).

All LARPs share an RNA Recognition Motif (RRM1) that is attached to their highly conserved winged-helix domain, the La-Motif (LaM). This domain is essential in recognizing RNA targets. In addition, every LARP family has a distinct structure, including additional domains and family-specific sequences (Maraia et al., 2017). The La motif is conserved among all LARPs, but the RRM exhibits member-specific traits (Figure 1). While LARPs exhibit structural diversity overall, structural similarities are more evident within individual families because of shared domains. The variety of structures within LARP enables a broad range of different binding formations and the ability to perform specific functions.

The La motif (LaM) is about 80 amino acids long (Bousquet-Antonelli & Deragon, 2009). This motif adopts a winged helix-turn-helix architecture, a common structural feature in many RNA-binding proteins. The RRM1 is also responsible for the binding of RNA, as previously described and is approximately 90 amino acids in length (Maraia et al., 2017). This domain has the typical fold found in RNA-binding proteins, consisting of a β-sheet flanked by α-helices.

There is remarkable versatility of the La motif and associated RRM domains in recognizing a wide array of RNA structures and sequences, including 3'-poly(A) tails, 3'-

oligo(U)-OH, specific stem-loops, and even 5'-ends of small RNAs (Kozlov et al., 2022; Alfano et al., 2004; Teplova et al., 2006). These domains have adapted to bind a broad range of RNA ligands and protein partners, enabling them to fulfill their diverse physiological activities. For example, LARP6 combines its La motif, RRM1, and the interdomain linker to recognize a specific stem-loop structure in collagen mRNAs (Martino et al., 2014). LARP4A also utilizes disordered regions and a PAM2w motif to interact with the poly(A) tail, potentially competing with or modulating PABP binding (Cruz-Gallardo et al., 2019) (Figure 1).

As a result, the combination of conserved domains and unique structural features in LARPs underlies their broad RNA recognition capabilities and enables their involvement in a wide range of cellular processes.

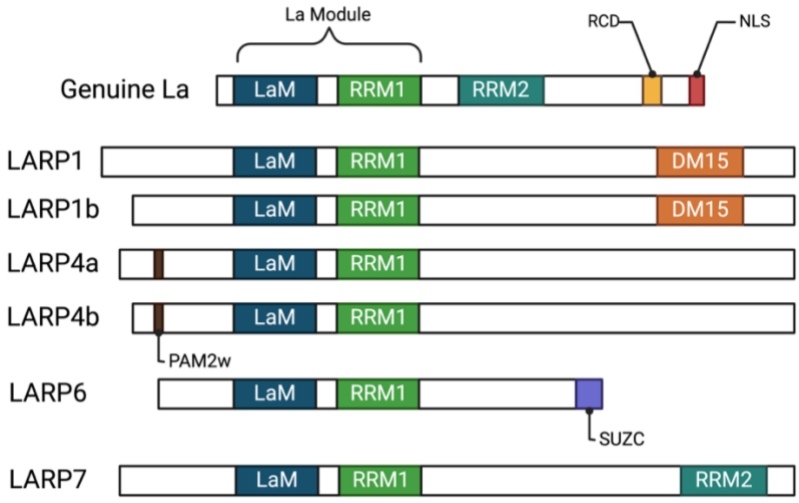

Figure 1. La-related protein domains. Domains within the La-related protein families. Abbreviations: LaM: La module, RRM: RNA Recognition Motif, RCD: RNA chaperone domain, NLS: Nuclear Localization Domain, SUZC: SUZC domain, PAM2w: PAM2w domain, DM15: DM15 containing region (Stavraka & Blagden, 2015). Figure adapted from (Stavraka & Blagden, 2015) and created using BioRender.

1.2 Comparative Analysis of LARP Family Functions in Translational Regulation

Although all LARP proteins possess a conserved LaM that enables RNA binding, distinct family-specific domains and sequence variations have driven the functional diversification of this protein family across eukaryotic species.

LARP1 is typically specialized for repression and selective regulation of ribosome-associated mRNAs. Proteins from this subclass bind 5'-terminal oligopyrimidine (5'TOP) motifs and translationally repress target mRNAs by competing with initiation factors, a mechanism conserved across eukaryotes that interfaces with TOR signaling pathways. (Berman et al., 2020; Fonseca et al., 2015). By contrast, LARP4 and its close relative LARP4B generally promote translation elongation and mRNA stability. LARP4 contains a PAM2 motif allowing direct interaction with PABP, and it localizes to poly(A)-enriched ribonucleoprotein granules that support mRNA stabilization and enhance translational output, especially under stress recovery (Yang et al., 2011; Stavraka & Blagden, 2015).

Other LARP family members, such as LARP6 and LARP7, control translation at distinct steps and cellular compartments. LARP6's LaM and RRM domains specifically recognize structured elements in collagen and other extracellular matrix mRNAs, coupling their cytoplasmic trafficking with translation on ER-associated ribosomes (Martino et al., 2014). LARP7, on the other hand, binds to non-coding 7SK RNA and inhibits transcription elongation, indicating that some LARP proteins indirectly influence translation by restricting RNA polymerase II (He et al., 2008).

Despite their differences, all LARP families exert a level of control over protein synthesis. Whether through cap- or poly(A)-tail interactions, they link environmental sensing (cellular stressors) to translational responses. This diversity of function allows LARP proteins to fine-tune gene expression across cellular compartments, ensuring that protein production is adapted to appropriate cellular needs.

1.3 The LARP1 Subclass

1.3.1 Overview & Introduction to LARP1

LARP1 was first discovered and identified in fruit flies (*Drosophila*), where it has been shown to play several key biological roles, including spermatogenesis, mitochondrial segregation, oogenesis, production of poles of mitotic spindles, embryogenesis, and promoting the synthesis of nuclear-encoded mitochondrial proteins (Blagen et al., 2009; Chauvet et al., 2000; Ichihara et al., 2007). It also plays an important role in mRNA translation, as it can bind to poly(A)-binding protein (PABP), a key regulator of mRNA stability and translational efficiency (Ogami et al., 2022). LARP1 knockout has been found to decrease overall protein synthesis while increasing levels of hypophosphorylated 4E-BP1, indicating its involvement in cap-dependent translation (Tcherkezian et al., 2014). This conclusion is further supported by evidence showing that LARP1 interacts with proteins that are associated with the 5' cap of mRNAs from ribosomal proteins and translation initiation factors (Iadevaia et al., 2008).

1.3.2 LARP1 in Plants and Metazoans

LARP1's role extends to plant-specific mRNA cohorts. The 5'TOP motifs present in humans are less prominent in plants. Despite this, LARP1 has been observed to function within a conserved TOR-LARP1-TOP axis, particularly within *Arabidopsis thaliana*. mRNA profiling

within this species shows that plant TOR activates ribosomal protein mRNA translation via LARP1, influencing TOP transcripts and plant-specific mRNAs. When TOR is inhibited, it impairs TOP mRNA tail length control and the reactivation of translation following cellular stress (Scarpin et al., 2020).

LARP1 in *C. elegans* (roundworm) modulates mRNA turnover and developmental signalling pathways by localizing to granules associated with mRNA decapping and degradation, specifically DCAP-1 (mRNA decapping enzyme) (Nykamp et al. 2008). LARP1 knockout disrupts the assembly of these granules. It alters the degradation of key mRNAs that are crucial within the rat sarcoma (RAS)- mitogen-activated protein kinase (Ras-MAPK) signalling pathway during oogenesis. Suggesting LARP1 influences the repression of translation and developmental pathways via mRNA stability.

1.3.3 Domains and Functions of hLARP1 and Slr1p, Sro9p, and Slf1p

Human LARP1 (hLARP1) possesses the La module alongside a DM15 region that plays a role in regulating RNA stability (Werneck-de-Castro et al., 2021). Its known RNA targets include 5' mRNAs with oligopyrimidine tracts (5'-TOPs), which mainly code for translation factors and ribosomal proteins, and mTOR-kinase responsive mRNAs characterized by pyrimidine-rich 5' untranslated regions (UTRs) (Alfano et al., 2004). Despite this, current studies on the translation of 5'-TOP mRNAs lack clarity and are characterized by conflicting findings. A potential regulatory role for LARP1 indicates that the DM15 region attaches to a 5'-TOP sequence, hindering access to the 7-methylguanosine cap of the 5'-TOP mRNA and obstructing eIF4F (Eukaryotic initiation factor 4F) assembly (Werneck-de-Castro et al., 2021) (Figure 2). However, upon phosphorylation of LARP1, the methyl guanosine cap separates from the DM15

region, allowing it to engage with eIF4F. This regulatory mechanism is essential for the management of ribosome biogenesis and modulates cell proliferation and cancer.

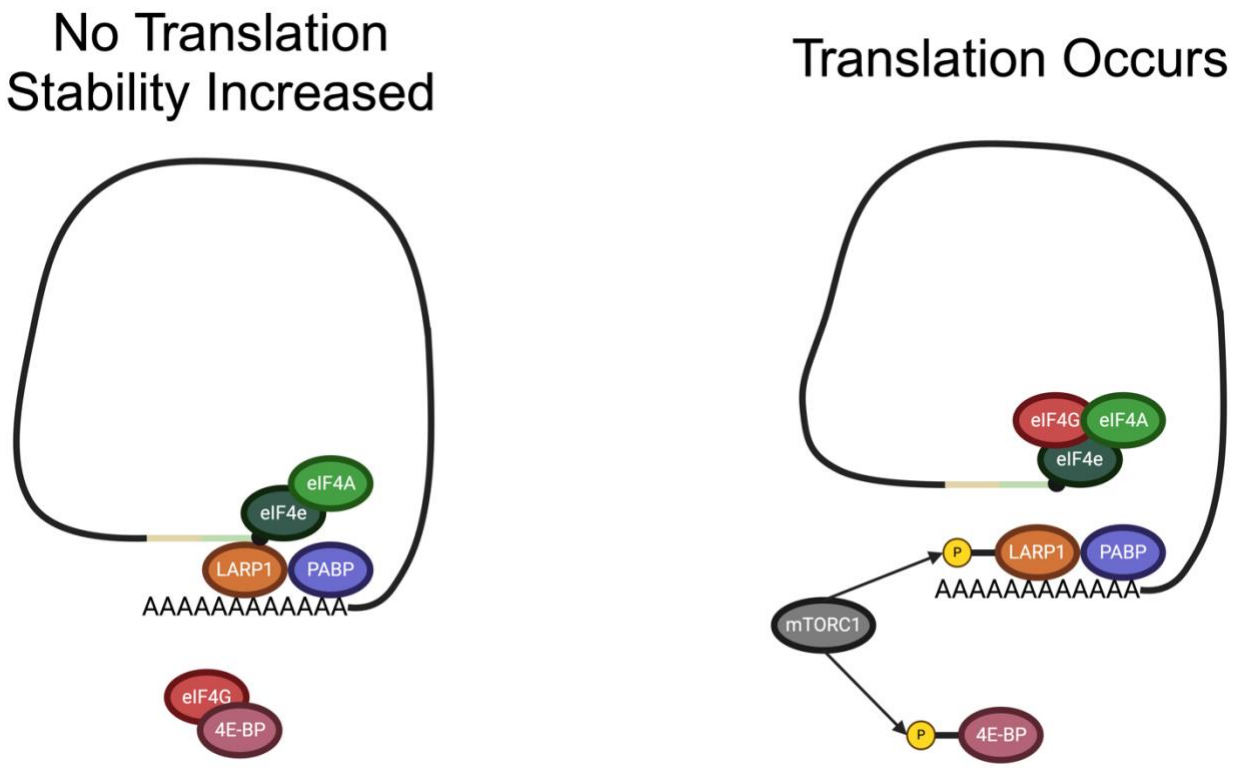

Figure 2. Function of LARP1 within the regulation of 5'-TOP mRNAs. Dephosphorylated LARP1 binds the 5' ends of TOP mRNAs, suppressing their translation and enhancing their stability by preserving the length of poly(A) tails. When mTORC1 is inactive, eIF4G is destabilized via 4E-BPs. When mTORC1 is activated, the phosphorylation of LARP1 stops its inhibitory function, which enables eIF4G to attach TOP mRNAs and start translating again. Adapted from (Berman et al., 2020) and created using BioRender.

Unlike hLARP1, yeast-derived LARP1-like Slr1p, Sro9p and Slf1p lack a DM15 motif and are thought to be the evolutionary precursor to LARP1 in higher eukaryotes (Mansouri-Noori et al., 2023). Despite the lack of this region, Slr1p has been observed to still maintain regulation of the translation and stability of mRNAs that encode proteins like 5′TOP mRNAs found in higher eukaryotes, since they possess the mRNAs that are functionally like those 5′TOP mRNAs (Mansouri-Noori et al., 2023). Due to the lack of DM15 and 5'-TOP sequence, Slr1p is

associated with several factors to help with the modulation of mRNA translation, such as eIF4G, components of eIF3I, and PABP. Dysregulation in the regulatory roles of LARP1 has been associated with a positive correlation with cell proliferation and cancer.

1.4 LARP1 and its Response to Cellular Stress

Organisms must be able to adapt to their environmental surroundings, and many employ a variety of mechanisms to protect themselves from harmful conditions. In 1985, the term "oxidative stress" was coined by Helmut Sies, and he referred to it as the imbalance between the net production of an organism's oxidant (most common is reactive oxygen species) compared to its antioxidant defence mechanisms (Krishnamurthy et al., 2024; Pizzino et al., 2017). Reactive oxygen species (ROS) serve multiple physiological functions, such as cell signalling, and are typically produced as by-products of oxygen metabolism. However, environmental stressors, including ionizing radiation, ultraviolet light, pollutants, heavy metals, and xenobiotics, significantly enhance ROS production. Certain biological processes also contribute to the production of ROS, including the electron transport chain, NADPH oxidases, and peroxisomes. This increase can result in an imbalance that causes cellular and tissue damage. The damage caused by this imbalance can lead to serious conditions such as cardiovascular disease, cancer, and various neurological, respiratory, and renal disorders (Liu et al., 2018). Antioxidants are used to combat the imbalance and build-up of ROS, and they work by donating electrons to free radicals to help stabilize them and prevent them from causing damage to other tissues (Lobo et al., 2010). These antioxidants can be either enzyme-derived (e.g. superoxide dismutase) or non-enzyme-derived (Vitamins C and E) (Ighodaro & Akinloye, 2018).

Typically, cells employ antioxidant defence mechanisms that enhance the expression of antioxidant genes. Recent findings have shown that LARP1 proteins, including Slf1p and Sro9p, play key roles in adapting to oxidative stress by associating with translating ribosomes and binding to highly translated mRNAs, particularly those encoding antioxidant enzymes (Jennings et al., 2023). Specifically, Slf1p plays a crucial role in maintaining the correct reading frame of ribosomes. In the absence of Slf1p, frameshifting is enhanced at multiple sites along mRNA sequences, which may result in the production of truncated protein forms that are likely targeted for degradation (Jennings et al., 2023). This could explain the observation within Slf1p knockout cells, where ribosomes continue to engage with antioxidants and other mRNAs under stress conditions, yet protein levels remain low. Sro9p uniquely plays a role in the formation of stress granules, which are cytoplasmic clusters of RNA and proteins that assemble in response to stress (Röther et al., 2010). These granules sequester non-essential mRNAs and translation factors, halting protein synthesis during stress. Sro9p helps regulate this process, ensuring the cell can effectively manage its stress response.

1.5 Differences and Similarities in the Functions and Structures of Slr1p, Slf1p, and Sro9p

1.5.1 Structural and Functional Similarities and Comparisons Between Slr1p, Sro9p, and Slf1p

Slf1p and Sro9p are La-related proteins in *Saccharomyces cerevisiae* (brewer's yeast) and are considered paralogs, having arisen from a gene duplication event and retaining related but distinct roles. These paralogs share a high degree of sequence similarity and are evolutionarily related to LARP1 and LARP4 proteins (Jennings et al., 2023). Lhp1p is another canonical La protein found in *Saccharomyces cerevisiae*, where it is localized in the nucleus and functions to protect precursor RNAs from exonucleases and nucleases, as well as to act as an RNA chaperone

(Yoo & Wolin, 1997). Slr1p is found in *Schizosaccharomyces pombe*, which shares a common ancestor with *Saccharomyces cerevisiae* dating back approximately 330 to 420 million years ago (Figure 3). While Slr1p shares some similarity with Slf1p and Sro9p, these are not as pronounced as the structural similarities typically observed between paralogs.

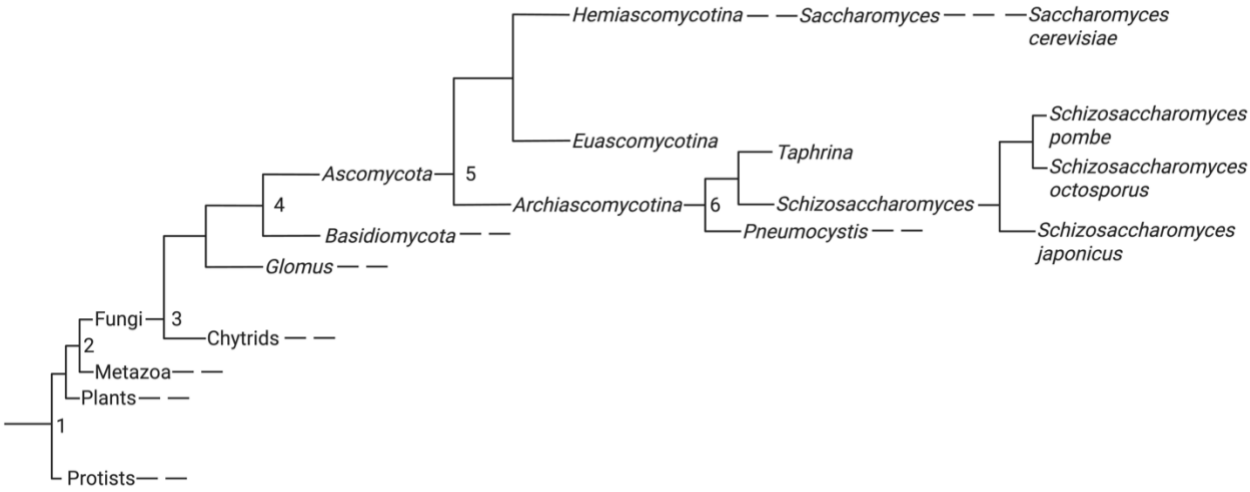

Figure 3. Phylogeny of fission yeast species. Numbers 1-6 represent the time points of genetic divergence. (1) 1.2 billion years ago, (2) 1.1 to 1 billion years ago, (3) 600 to 500 million years ago, (4) 400 million years ago, (5) 420 to 330 million years ago, (6) 250 million years ago. Figure adapted from (Sipiczki, 2000) and created using BioRender.

Structurally, Slr1p, Slf1p and Sro9p possess a relatively simple domain organization, lacking the complex regulatory regions observed in hLARP1, which features a multi-domain structure (Jennings et al., 2023). The absence of complex regulatory domains in yeast LARPs suggests they may utilize alternative mechanisms to regulate protein synthesis and RNA stability. Sequence alignment further reveals two conserved short regions near the N-terminus, which are shared between Slf1p, Sro9p, and their homologs in other yeast species. Homologs are defined as an umbrella term for a group of proteins that have a common evolutionary origin; all LARP1 proteins are homologous to each other. The LaM of Slf1p, Sro9p and Slr1p is specifically responsible for mRNA-binding, while a novel 40S ribosomal subunit binding motif,

located within the N-terminus of Slf1p, is also present in Sro9p (Sobel & Wolin, 1999). In this study, Slr1p, Slf1p, and Sro9p genes were cloned to include only their LaM regions, which retain RNA-binding functionality.

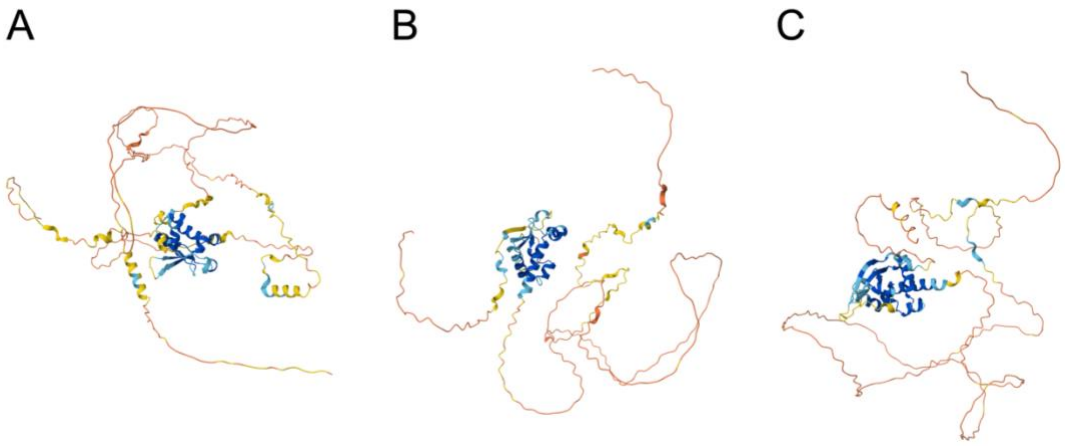

Figure 4. AlphaFold prediction of Slr1p, Sro9p, and Slf1p structures. **(A)** Predicted structure of Slr1p. (**B)** Predicted structure of Sro9p. (**C)** Predicted structure of Slf1p. For **(A)-(C)** Confidence: dark blue = very high (pLDDT> 90), light blue = confident (90> pLDDT > 70), yellow = low (70> pLDDT > 50), orange =very low (pLDDT < 50) (Jumper et al., 2021).

1.5.2 Differences in functions of Slr1p, Slf1p and Sro9p

Although the proteins of interest are structurally similar, they exhibit different functions. Slf1p mainly acts as a translational modulator, promoting the translation of stress-responsive mRNAs and stabilizing ribosomes that have stalled (Jennings et al., 2023) (Figure 5). Conversely, Sro9p plays a role in transcription, mRNA export, and translation, among other facets of gene expression (Sobel & Wolin, 1999). As previously mentioned, Slr1p has been observed in the regulation of proto-5′TOP mRNAs, those with features akin to mammalian 5′TOP transcripts (Mansouri-Noori et. al, 2023). However, Slf1p and Sro9p are distinctly associated with polysomes when under high-stress conditions (Table 1). These functions differ

from those of hLARP1 previously described, which associates with top mRNAs and other elongation factors, playing a role in mRNA stabilization. Disruption of this process can lead to cell proliferation.

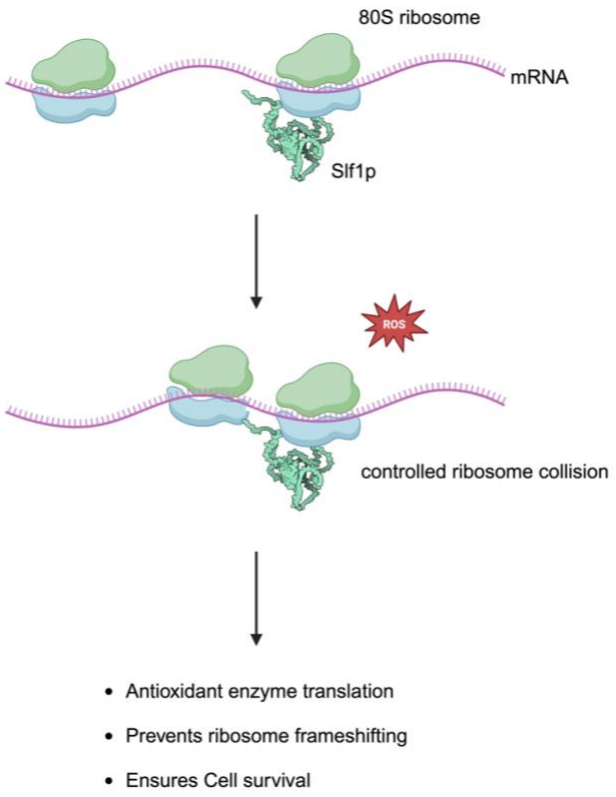

Figure 5. Interaction between Slf1p and colliding ribosomes. Slf1p stabilizes ribosomes that are translating antioxidant enzyme mRNAs, aiding in the cell's adaptation to stress. Sro9p is suspected to utilize the same pathway when under stress conditions. Figure created using BioRender.

Table 1. Function and cellular localization of Slr1p, Slf1p, and Sro9p.

Protein	**Function**	**Localisation**
Slr1p	Involved in ribosome biogenesis and translation regulation of proto-5′TOP mRNAs.	Cytoplasmic
Slf1p	Stabilizes ribosomes translating antioxidant enzyme mRNAs, promoting cellular adaptation to stress.	Cytoplasmic
Sro9p	Involved in mRNA metabolism. Plays a role in RNA-binding and processing.	Cytoplasmic

1.6 RNA Targets and Binding Regions

Unlike other LARP subfamilies, the LaM of LARP1 binds to RNA as an independent domain that favours poly(A) sequences (Kozlov et al., 2022). It binds in such a way that in the absence of connections from an adjacent RNA recognition motif (RRM) domain, the terminal and penultimate adenylate nucleotides (positions 1 and 2 from the 3′-end) interact in a manner analogous to uridylates in other La-related proteins (LARP). In hLARP1, the terminal (1) ribose is stabilized through polar interactions with Asp346, while its adenine ring stacks on Phe348. The penultimate (2) adenine ring is positioned by a hydrogen bond with Gln333 and stacking interactions with Tyr336 (Kozlov et al., 2024). The arrangement of the preceding nucleotides exhibits considerable variability, with either the (3) or (4) nucleotide stacking between His368 and the (1) adenine (Kozlov et al., 2024). The stacking mechanism, often involving phenylalanine and tyrosine, plays a key role in increasing binding affinity and stabilizing the structure. Mutational analyses demonstrated that alterations in these residues significantly impacted the binding affinity, underscoring their essential roles in the recognition process (Kozlov et al., 2024).

As previously mentioned, there has been some insight into how LARP1, such as Sro9p and Slf1p, work within stress response mechanisms. They specifically associate with the open reading frames (ORFs) of a shared subset of actively translated mRNAs, including stress response mRNAs that are transcriptionally upregulated in response to stress (Jennings et al., 2023). Their binding sites are generally positioned similarly to ribosome footprints and are enriched toward the 3' ends of ORFs. The YGSU motif is present in almost half of the ORF binding sites, suggesting that this motif has significance in binding target mRNAs (Jennings et al., 2023).

Recent analysis has also shown an unexpected preference for sequences containing single guanine substitutions within a poly(A) strand. The addition of more guanines within the tract did not improve or augment the binding affinity. This suggests that LARP1 may play a role in the stabilizing effect of poly(A) tail guanylation (Kozlov et al., 2024). A similar study sought to investigate a wider variety of RNA oligonucleotides and their binding affinities to the LaM of LARP1. The results showed that internal uridine or cytosine residues within a poly(A) strand exhibited the best binding affinity, followed by long poly(A) strands, poly(U) strands, poly(G) strands, and poly(C) strands (Kozlov et al., 2022). A single mutation of one of the critical residues for binding within the hLARP1 LaM to an alanine (Q333A) showed a significant drop in affinity compared to wildtype, and a double mutation of residues 333 and 348 to alanine showed no binding whatsoever (Kozlov et al., 2022). This indicates that residues Q333, Y336, R345, F348, and H368 identified through crystal and NMR solution structure are key to binding within the LARP1 LaM.

1.7 Protein NMR

The identification of protein structure is essential for comprehending its function, particularly the binding mechanisms it employs and their specific locations. NMR spectroscopy provides structural insights through two-dimensional heteronuclear single-quantum coherence (^{15}N-HSQC) spectroscopy and various three-dimensional experiments. Most peaks observed in the ^{15}N-HSQC spectrum can be correlated to their respective amino acids using AI-based software such as NMRtist. This program facilitates the identification of most of the protein backbone (specifically NH groups) by processing Bruker NMR data. However, the remaining nitrogen, hydrogen, and carbon atoms require manual assignment.

Manual assignment of the protein backbone is primarily conducted using HNCACB, CBCA(CO)NH, HN(CA)CO, and HNCO experiments (Cavanagh et al., 2010). The HNCACB spectrum provides information on the alpha and beta carbon peaks of a given amino acid as well as those of its preceding residue (Table 2). This data is typically analyzed in conjunction with CBCA(CO)NH, which serves to differentiate the alpha and beta carbons originating from the preceding residue (i-1) (Table 2). The identification of carbonyl carbon (CO) resonances is typically achieved using HNCACO and HNCO experiments. Specifically, the HNCACO spectrum contains CO peaks corresponding to both the amino acid under observation and its preceding residue, whereas the HNCO spectrum contains CO peaks exclusively from the preceding residue (Table 2). By establishing a continuous sequence of alpha and beta carbon assignments within regions not identified by NMRtist, a complete backbone assignment can be achieved.

Once the protein backbone has been assigned, further structural characterization, including the identification of side chains, aromatic residues, and additional hydrogen atoms, can be performed using three-dimensional spectra such as (H)CCH-TOCSY, ^{13}C-HMQC, and HBHA(CO)NH (Cavanagh et al., 2010) (Table 2). The (H)CCH-TOCSY spectrum provides chemical shift correlations between side-chain hydrogen atoms and their directly bonded carbon atoms, as well as the resonances of other carbon atoms within the same side chain. These hydrogen resonances can be further examined by comparing the alpha and beta carbon shifts in the (H)CCH-TOCSY spectrum with those in the HNCACB spectrum. This approach facilitates the assignment of residues in the ^{13}C and ^{15}N HSQC spectra if they have not been previously assigned.

NMR-derived structural constraints, particularly those from the nuclear Overhauser effect (NOE) and torsion angles, provide further insights into protein conformation. The NOE describes the intensity change of one resonance upon perturbation of a neighbouring resonance, while torsion angles represent bond rotations. The ^{15}N edited 3D NOESY experiment provides distance constraints between hydrogen atoms within the protein, specifically amide hydrogen atoms. Similarly, the ^{13}C edited 3D NOESY experiment determines distance restraints between hydrogen atoms bound to carbon atoms (Cavanagh et al., 2010) (Table 2). The combination of backbone and side-chain assignments, along with NOESY cross-peak intensity data, ultimately facilitates NOE assignments and enables the determination of an ensemble of three-dimensional protein structures.

Table 2. Nuclear Magnetic Resonance (NMR) experiments and their respective magnetization pathways (amino acid on left = i-1, amino acid on right = i). The white atoms are not participating in the magnetization pathway. The green atoms are the chemical shifts that are measured and used for assignment and the yellow atoms are bonded partners that enable magnetization transfer but are not recorded in the experiment (Cavanagh et al., 2010).

Experiment	Magnetization pathway	
^{1}H-^{15}N HSQC (left) HBHA(CO)NH (right)	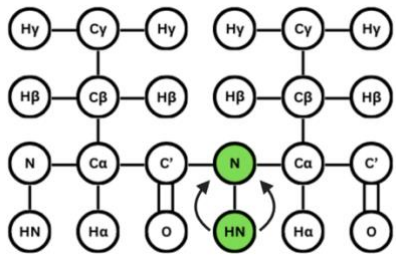	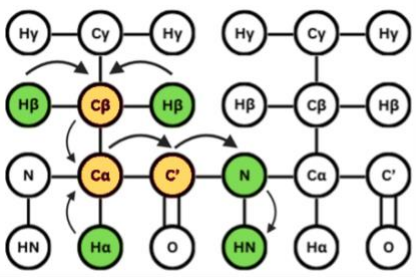
CBCA(CO)NH /HN(CO)CACB (left) HN(CO)CA (right)	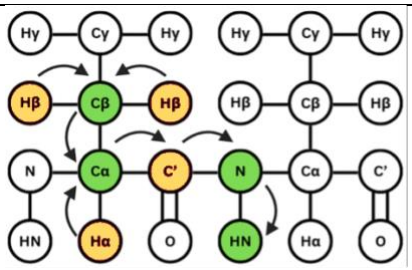	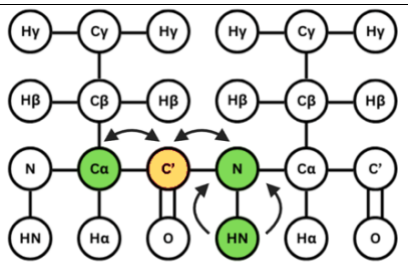

CBCANH/HNCACB (left) HNCO (right)	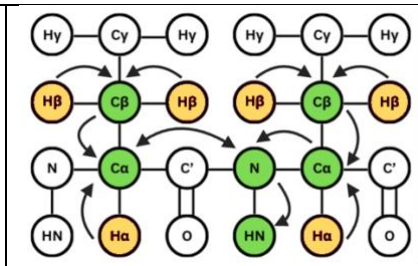	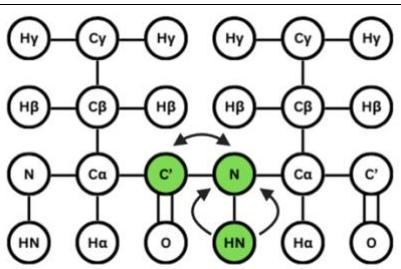
HN(CA)CO (left) HNCA (right)	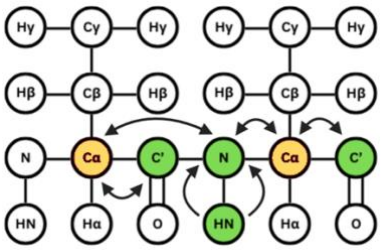	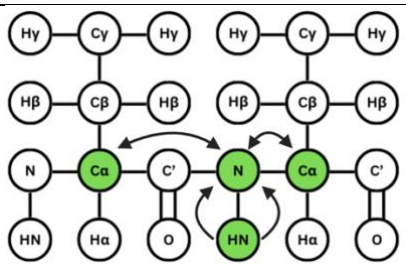
^{15}N edited 3D NOESY (left) ^{13}C edited 3D NOESY (right)	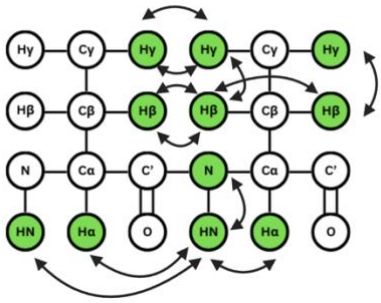	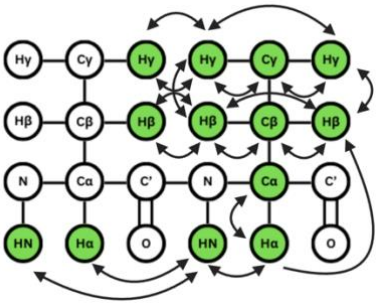
^{13}C-HMQC (left) CC(CO)NH (right)	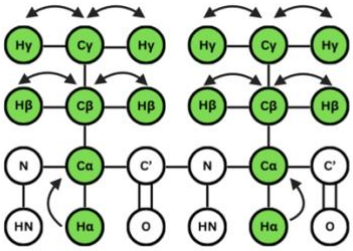	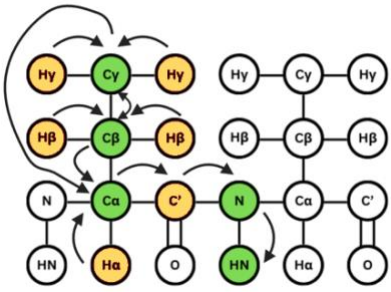
^{15}N-TOCSY-HSQC	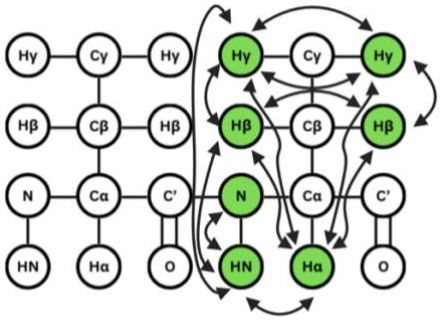	

1.8 Objectives and Hypothesis

This thesis aimed to investigate the LaM structures of Slr1p, Slf1p, and Sro9p, along with their binding interactions with a selected set of RNA and small-molecule ligands: RNA15 (UUUUUCCACCACCAA), RNA6 (UCGGUA), diadenosine tetraphosphate (Ap4A), and hexa-adenosine (6A). The RNA15 and RNA6 oligonucleotides are named based on their lengths, 15 and 6 nucleotides, respectively. RNA15 contains a U-rich sequence that has structural similarity to 3' U-rich RNA tails known to interact with La motif domains, while RNA6 is based on the YGSU motif, which Slf1p and Sro9p have been shown to prefer. Diadenosine tetraphosphate (Ap4A), a well-characterized stress-response molecule, was included based on prior evidence of its interaction with LARP proteins in specific stress-related pathways. Hexa-adenosine (6A), a homopolymeric adenosine RNA, was selected for testing because of the binding preferences of poly-A tails common in some LARPs. The hypothesis was that these proteins employ conserved RNA-binding patches to recognize the 3' ends of RNA with similar affinities, due to their structural homology.

Yeast LARP1 homologs represent an effective model system due to their genetic tractability, rapid growth, and reduced structural complexity relative to hLARP1. They also provide valuable insight into hLARP1 due to the evolutionary conservation of key RNA-binding domains. Additionally, the absence of certain regulatory domains, such as the DM15 domain, allows for a focused investigation of the fundamental roles of the conserved motifs without interference from higher-order regulatory elements.

To achieve the objectives outlined below, we employed a range of methods including NMR protein residue assignment, chemical shift perturbation (CSP), isothermal titration calorimetry (ITC), differential scanning calorimetry (DSC), and circular dichroism (CD).

- Unbound structure of Slr1p and Slf1p and the identification of beta-sheet networks within both of their structures using NMR spectroscopy.
- Identification of binding-site residues in Slr1p and Slf1p through CSP analysis of unbound and ligand-bound NMR spectra.
- Secondary structure composition of all proteins using CD.
- The T_m and the thermodynamics of all three proteins of interest using DSC.
- The K_d and binding thermodynamics of all three proteins when bound to RNA6, RNA15, 6A and Ap4a using ITC.

These findings expand the understanding of the structures and RNA-binding mechanisms of yeast LARP1 homologs.

2. MATERIALS

2.1 Solutions and Chemicals

Table 3. Buffers and Applications for Nickel Column and Gel Chromatography.

Buffer	**Application**	**Composition**	**Source**
T300	Nickel Column Chromatography (Resuspension and Wash Buffer)	50 mM Tris, 300 mM NaCl, 0.001% NaN_3 (w/v), pH 7.6	BioShop, ThermoScientific
Imidazole Nickel Column Wash Buffer	Nickel Column Chromatography (Wash Buffer)	20 mM Imidazole, 49 mM Tris, 294 mM NaCl, 0.001% NaN_3 (w/v), pH 7.6	BioShop, ThermoScientific
Nickel Column Elution Buffer	Nickel Column Chromatography (Elution Buffer)	500 mM imidazole, 25 mM Tris, 150 mM NaCl, 0.0001% NaN_3 (w/v), pH 7.6	BioShop, ThermoScientific
PBS Gel Filtration Buffer	Gel Filtration Buffer	150 mM NaCl, 20 mM NaP, pH 7.4	Fisher Reagents
NaOH Buffer	Nickel Column Chromatography (Regeneration and Cleaning Buffer)	200 mM NaOH	BioShop

2.2 Reagents

Table 4. Reagents for Bacteria Growth and Protein Expression.

Name	**Application**	**Source**
LB media	Cell Growth	BioShop
Kanamycin	Drug resistance	BioShop
Isopropylthio-β-galactoside (IPTG)	Induction	Sigma Aldrich

Table 5. Reagents for Transformation.

Name	**Application**	**Source**
pET-29	Slf1p, Sro9p	Novagen
pET-28	Slr1p	Gene Universal
BL21 cells	Electrocompetent cells	Cryogenic stock
LB media	Cell Growth	BioShop

Table 6. Reagents for Protein Quantification.

Name	**Application**	**Source**
Precision Plus Protein Dual Color Standards	Protein Ladder	Bio Rad
InstantBlue® Coomassie Protein Stain	Protein Gel Staining	Abcam
Mini-PROTEAN TGX Gels	Protein Gel	Bio Rad
Laemelli Sample Buffer	Sample Loading Buffer	Bio Rad

Table 7. Reagents for Structural and Binding Experimental Techniques.

Experiment	**Name**	**Source**
NMR	DMSO	Sigma Aldrich
	EDTA	Sigma Aldrich
	PBS Gel Filtration Buffer	Fisher Reagents
ITC	PBS Gel Filtration Buffer	Fisher Reagents
DSC	PBS Gel Filtration Buffer	Fisher Reagents
CD	PBS Gel Filtration Buffer	Fisher Reagents

2.3 Protein Sequences and Oligonucleotides

Table 8. Protein sequences.

Name	**Sequence**	**Plasmid**	**Source & Catalog #**
Slr1p	MDVQAFLTSQLEYYFSIENLSKD MFLRKHMDDEGYVPLAFLASFN RIKSFSTDLNLLHAAAKASDIIDV AEDLQSPMSIKVRRKETWSPWIL PSESRLKFEMAKYLEHHHHHH	pET28	Gene Universal SPAC1527.03
Slf1p	MKSIESIKNQIEFYFSEENLKTDE FLRSKFKKANDGFIPMSLIGKFY RMVNLSLGGDPNLILASMREVL QHKETNHLEIALGSIEGAQKNM ADDFNPLENYFIRRENWAEYAM ESNFDENDDETEKYNIEKLLGPN DLDNYSYLEHHHHHH	pET29	Novagen Q12034
Sro9p	MAINNIARQIEYYFSEENLTVDN YLRSKLSKDGFAPLSLISKFYRV VNMSFGGDTNLILAALREIVANE AATVNVAEGTLAAKEGDNVTG EAKEPSPLDKYFVRSKSWSNWL	pET29	Novagen P25567

	PETFETEINIEKELVGDALDQFMI LEHHHHHH		

Table 9. Oligonucleotides.

Name	**Sequence**	**Source**
RNA15	UUUUUCCACCACCAA	Bio-synthesis
RNA6	UCGGUA	Bio-synthesis
6A	AAAAAA	Horizon Biosciences
Ap4a	AppppA	GenScript

2.4 Equipment and Software

Table 10. Equipment for Transformation and Cell Lysis.

Name	**Application**	**Source**
BTX™ ECM™ 399 Exponential Decay Wave Electroporator	Electroporation	Fisher Scientific
Electroporation Cuvettes Plus™	Electroporation	Fisher Scientific
Barnstead MaxQ 4000 A-Class Benchtop High	Incubator/Shaker	Thermo Scientific
J2-HS Centrifuge	Centrifugation	Beckman Coulter
French Pressure Cell Press	Lysis	Thermo Spectronic
Ultrasonic Liquid Processors XL-2000	Sonication	Misonix

Table 11. Equipment for Protein Expression, Purification, and Quantification.

Procedure	**Name**	**Source**
IMAC Purification	P-50 Pump	Amersham Biosciences

	PureCube 100 Ni-NTA Agarose	Cube BioTech
SEC Purification	ÄKTA pure™ chromatography system	GE
	HiPrep 16/60 Sephacryl S-100 HR	Cytvia
Concentration	5 kDa MWCO centrifugal concentrator column	Sigma Aldrich
	10 kDa MWCO centrifugal concentrator column	Sigma Aldrich
Protein Quantification	NanoDrop 2000 spectrophotometer	Thermo Scientific
Gel Visualization	AlphaImager HP	Alpha Innotech

Table 12. Equipment for Structure and Binding Experiments.

Application	**Name**	**Source**
NMR	Avance III 700 MHz NMR spectrometer	Bruker
DSC	Nano DSC	TA Instruments
ITC	MicroCal PEAQ-ITC	Malvern Panalytical
CD	J-815 CD Spectrometer	Jasco

Table 13. Software.

Application	**Name**	**Source**
Predicted Structure	AlphaFold	DeepMind
	pyMOL OpenSource	pyMOL
	TALOS+	NMRbox
NMR	TopSpin	Bruker
	CcpNMR	CCPN

	NMRtist	ETH Zurich
DSC	Nano DSC	TA Instruments
ITC	MicroCal PEAQ-ITC Analysis Software	Malvern Panalytical
CD	Spectra Manager	Jasco

3. METHODS

3.1 Transformation of Slr1p, Sro9p, and Slf1p into BL21 competent cells

10 ng of (Slr1p, Sro9p, and Slf1p) DNA was added to 100 µL of BL21 competent cells, and then 80 µL was transferred into a cold electroporation cuvette. The cells were electroporated at 1500 V for 4-5 ms. 1 mL of LB media was added to rescue the cells and was transferred into a 15 mL culture tube. The cells were incubated at 37 °C and 200 rpm for 45 minutes. 100 µL was then plated onto LB/Kan plates and incubated at 37 °C overnight. Selected colonies were transferred into cryogenic tubes containing 800 µL of LB media and 200 µL of DMSO, then stored at -80 °C. The remaining colonies on the plates were stored for up to a week at 4 °C.

3.2 Expression and Purification of Protein

3.2.1 Bacterial Cell Growth and Protein Expression

An initial volume of media (50 mL LB media + 50 µL kanamycin stock) was inoculated with cells derived from cryogenic stocks (either Slr1p, Slf1p, or Sro9p). This initial culture was grown overnight at 37 °C and 200 rpm and was transferred to a 1 L culture (LB + 1 mL kanamycin stock) where growth was allowed to continue at 37 °C and 200 rpm. Once the OD_{600nm} of the culture reached the mid-log phase, between 0.7-0.8, 1 mM of IPTG was added to the culture. After 3-4 hours, the culture was centrifuged at 6000 rpm for 10 minutes. The cell pellets were stored at -20 °C for future experimentation, while the supernatant was discarded.

To make single-labelled (^{13}C or ^{15}N) or double-labelled protein ($^{13}C^{15}N$), M9 media was used instead of LB media. To prepare 1 L of M9 minimal media, 6 g of Na_2HPO_4 (dibasic), 3 g of KH_2PO_4 (monobasic), 0.5 g of NaCl, 1 g of $^{15}NH_4Cl$ (for ^{15}N labeling), and 3.5 g of ^{13}C-labeled glucose (for ^{13}C labeling) were dissolved in water. 1 mL of $MgSO_4$ and $CaCl_2$, 0.2 mL of

trace minerals, and 1 mL of kanamycin were added afterwards. 50 mL of the M9 media was sterile filtered using a 0.2 μM filter syringe into a 250 mL flask, which was inoculated with cells from a cryogenic stock. The subsequent growth and expression procedures were identical to those used with LB media for protein production.

3.2.2 Protein Purification

Cell pellets were resuspended in about 30-40 mL of T300 buffer (50 mM Tris, 300 mM NaCl, 0.001% NaN_3, pH 7.6) and were first lysed using a French press cell disrupter, followed by 30 seconds of sonication. The cell solution was then centrifuged at 16,000 rpm for 10 minutes. Depending on the solubility of the protein, it was found either in the pellet or in the supernatant. If the protein was soluble, the pellet was discarded, and the supernatant was obtained. If the protein was insoluble, then the supernatant was discarded, and 6 mL of 8 M urea in T300 buffer was added to the pellet to resuspend. The resuspended mixture was then added to 240 mL of T300 buffer dropwise. The resulting solution was then centrifuged at 16,000 rpm for 5 minutes, and the supernatant was obtained.

Purification was performed using nickel affinity chromatography (Cube BioTech). The column was first washed with 75 mL of 0.2 M NaOH to remove residual proteins and microorganisms that may have resided within the resin, followed by 100 mL of T300 buffer. The lysate was pumped through the column, and a second cycle of washing with 100 mL of T300 followed afterwards. The column was then washed with 50 mL of 20 mM imidazole, and the purified protein was eluted with 35 mL of 500 mM imidazole. The pump rate throughout the chromatography process remained at a constant 15.0 mL/min.

The nickel column elute was then concentrated using either 5 or 10 kDa MWCO centrifugal concentrator columns to obtain a final volume of approximately 5-6 mL. The sample was then injected into the ÄKTA pure™ chromatography system (GE) for a final purification and buffer exchange using the HiPrep 16/60 Sephacryl S-100 HR column (Cytvia). The protein solution was eluted at 1.5mL/min into a 96-well plate (1.5 mL per well), where the protein was in a final solution consisting of PBS buffer (60 mM NaCl, 10 mM NaP, pH 7.4). The fractions with the highest concentrations of protein were analyzed using the ÄKTA pure™ chromatography system software and were pooled. The protein solution was then further concentrated using either 5 or 10 kDa MWCO centrifugal concentrator columns to achieve the desired concentrations required for further experimental techniques.

3.2.3 Visualization of Proteins

20 μL of purified protein sample was mixed with 20 μL of Laemelli Sample Buffer. Mini-PROTEAN.TGX™ 4-20% Precast Gel was set up in the gasket filled with SDS running buffer. 20 μL of the protein sample (with sample buffer) was loaded along with 4 μL of Precision Plus Protein Dual Colour Standards for the protein ladder. Separation of the protein through the gel was done at 180V for 40 minutes. The gel was then stained with InstantBlue®. Coomassie Protein Stain (Abcam) on a shaker and imaged using AlphaImager HP.

3.2.4 Protein Quantification

The NanoDrop 2000 spectrophotometer (Thermo Scientific) was used to quantify proteins using A_{280nm} readings. Using the values obtained from the spectrophotometer, the protein concentrations were calculated using the Beer-Lambert law.

3.3 Isothermal Titration Calorimetry

Thermodynamics and binding parameters of Slr1p, Sro9p, and Slf1p with RNA6, RNA15, Ap4a, and 6A ligands were examined utilizing a MicroCal Auto PEAQ-ITC instrument (Malvern) at 25 °C in PBS buffer (60 mM NaCl, 10 mM NaP, pH 7.4). All experiments consisted of an initial delay of 120 s, first purge injection of 0.2 μL and subsequent 18 injections of 2 μL titrant, spaced every 180 s between every injection. The first point was removed from all data sets due to having a different injection volume. For binding experiments, 120 μL of 100 - 200 μM protein variant solution was titrated into a 400 μL sample cell containing 5 - 20 μM RNA ligand. For reverse titration experiments, an RNA ligand was titrated into a protein solution in the sample cell. Thermograms were analyzed with the subtraction of the heat of dilution of the corresponding titrant. Acquired ITC data were analyzed by integrating heat of injection as a function of molar ratio of the titrant to quantify dissociation constant (K_d), enthalpy change (ΔH), entropy change (ΔS), and Gibbs free energy change (ΔG) using the supplied analysis software package.

All ligands were custom synthesized: RNA6 (derived from a YGSU motif, Bio-synthesis), RNA15 (previously reported sequence used in literature, Bio-synthesis), 6A (poly-A strand, Horizon Biosciences), and Ap4a (a known stress-signaling molecule, GenScript). When preparing for titrations with Ap4a and 6A, the previous procedure was followed, but titrant Ap4a solutions were at a concentration of 1.56 mM while the Slr1p sample was 100 μM. While titrations with 6A were conducted with 50-200 μM of protein and 5 - 20 μM of 6A ligand.

3.4 Circular Dichroism (CD) Spectroscopy

Slr1p, Slf1p and Sro9p protein samples were prepared at a concentration of 10 μM and 30 μM for Slr1p in a buffer consisting of 10 mM sodium phosphate and 60 mM NaCl at pH 7.4. These solutions (400 μL) were placed in a 0.1 cm quartz cell and analyzed using a Jasco J-815 spectrophotometer with a six-position temperature control unit. Thermal denaturation experiments were monitored at 208 nm and 222 nm during a temperature period of 40 °C - 90 °C, at a rate of 1 °C/min

3.5 Differential Scanning Calorimetry

Protein samples were prepared in PBS buffer (60 mM NaCl, 10 mM NaP, pH 7.4) as described above. Isobaric calorimetry experiments for 0.9 - 2 mg/mL Slr1p, Slf1p and Sro9p proteins, along with their bound forms to 6A, were individually performed utilizing a Nano DSC equipped with an autosampler (TA Instruments). Heating experiments were performed with a scan rate of 1 °C/min from 5 °C to 95 °C at 3 atm pressure of nitrogen gas. Blank samples of corresponding buffers were used for baseline controls. Data acquired from buffers were subtracted from each experiment. The thermal denaturation point (T_m) and enthalpy change (ΔH) values were quantified using the NanoAnalyze software package.

3.6 Nuclear Magnetic Resonance

A 400 μL sample of isotopically labeled protein solution, containing 40 μL of deuterium oxide, was prepared in a 5 mm NMR tube for NMR spectroscopy. When a 3 mm NMR tube was used, 200 μL of protein sample containing 20 μL of deuterium oxide was prepared. Utilizing the Avance III 700 MHz NMR spectrometer and TopSpin software (Bruker), a series of experiments

including ^{1}H-^{15}N HSQC, HBHA(CO)NH, CBCA(CO)NH/HN(CO)CACB, HN(CO)CA, CBCANH/HNCACB, HNCO, HN(CA)CO, HNCA, ^{15}N edited 3D NOESY, ^{13}C edited 3D NOESY, ^{13}C-HMQC, CC(CO)NH, and ^{15}N-TOCSY-HSQC were acquired.

The spectra generated from these experiments aided in residue identification and structural determination. The program CcpNMR was used to pinpoint and identify carbon, amide, and hydrogen residues across the collection of spectra. The coordinates of the residues were then used and input into software TALOS+ (Torsion Angle Likeliness Obtained from Shift and Sequence Similarity) to predict the relation between ^{13}C, ^{15}N and ^{1}H chemical shifts and backbone torsion angles ψ and φ.

To investigate the binding of Slf1p with RNA6, a titration of RNA6 into the NMR was done after a series of unbound spectra were collected first. The composition of the NMR tube after the titration was 360 μL of Slf1p at a concentration of 410 μM and 9 μL of RNA6 with a concentration of 425 μM. A similar process was followed with the RNA6 and RNA15 titrations with Slr1p, both titrations were done at a stoichiometric ratio of 1:1. All NMR experiments were done under 298 K conditions.

3.7 Amide and Methyl Chemical Shift Perturbation

Chemical Shift Perturbation (CSP) refers to changes in the NMR chemical shifts of nuclei (e.g., ^{15}N or ^{13}C) in a molecule upon interaction with another molecule, such as a ligand binding to a protein. Chemical shifts represent the resonance frequency of a nucleus relative to a reference compound, expressed in Hz (actual) or in parts per million (ppm) relative to the Larmor frequency of the nucleus. These shifts are sensitive to the electronic environment around

the nucleus; thus, ligand binding alters the local electronic environment, leading to observable changes in NMR chemical shifts.

To identify binding interfaces, the weighted chemical shift perturbations (Δδ) of backbone amides (^{15}N-HSQC) and methyl carbons (^{13}C-HSQC) between bound and unbound states of Slf1p and Slr1p were calculated using the equation:

$$\mathrm{CSP} = \sqrt{\frac{(\Delta\delta_H)^2 + (\alpha \cdot \Delta\delta_x)^2}{2}} \quad (1)$$

$\Delta\delta_H = |\delta_{H,perturbed} - \delta_{H,free}|$
$\Delta\delta_x = |\delta_{x,perturbed} - \delta_{x,free}|$, calculating shift change in ^{13}C-HSQC then, x = C. Calculating shift change in ^{13}N-HSQC then, x = N
$\alpha = 0.14$ when for ^{15}N and 0.3 for ^{13}C

4. RESULTS

4.1 AlphaFold structure predictions reveal similarities and differences between protein structures

AlphaFold was utilized to predict the full-length, wild-type 3D structures of Slr1p, Slf1p, and Sro9p. Given that the LaM domain mediates RNA binding in LARP1 proteins, this region was selected from the AlphaFold models and used in all subsequent experiments (Figure 6).

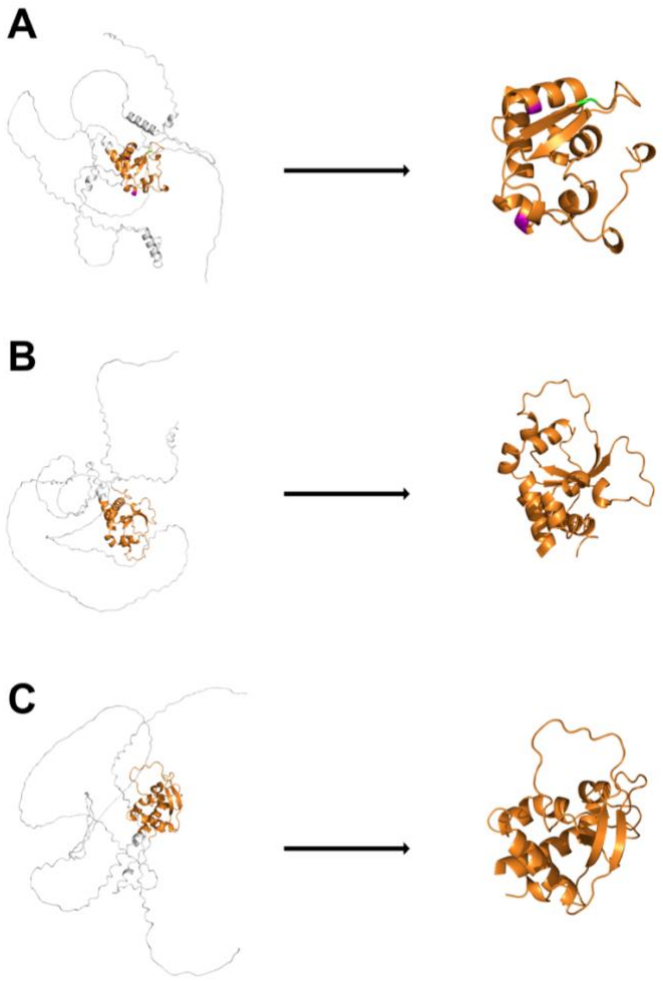

Figure 6. Full structures of Slr1p, Slf1p and Sro9p with the portion of the LaM of each protein being used for experimentation. (A) Full predicted AlphaFold structure of Slr1p with the region of interest highlighted in red (residues 324 - 427). Two cysteines were substituted for a serine and an alanine. Both are highlighted in purple (C343S, C383A). An isoleucine was substituted for a glutamic acid, highlighted in green (I392E). Thus, creating the Slr1p modified LaM. **(B)** Full predicted AlphaFold structure of Slf1p with the region of interest highlighted in red (residues 270 - 411). **(C)** Full predicted AlphaFold structure of Sro9p with the region of interest highlighted in red (residues 260 - 395). All structures were displayed using pyMOL OpenSource.

The predicted structural models of Slf1p and Sro9p had an RMSD of 1.2 Å, indicating strong structural similarity. This result aligns with the expectation that paralogous proteins, originating from gene duplication and exhibiting significant sequence similarity, should possess similar structures (Figure 7).

The differences between these two paralogs and Slr1p are more distinct. Slr1p does not possess a loop in the winged helix region that is seen within Sro9p and Slf1p (Figure 8A). It is also missing an entire beta-strand that is present in Slf1p and Sro9p (Figure 8B); this region comprises additional residues in the C-terminus that were introduced to enhance protein stability. Sro9p, Slr1p and Slf1p all maintain a conserved binding patch between them. The hypothesized binding patch between Sro9p and Slf1p is more like each other than to Slr1p, especially within residues 43, 45, and 48 (Figure 8C). The minor difference in their structures may be linked to their cellular functions.

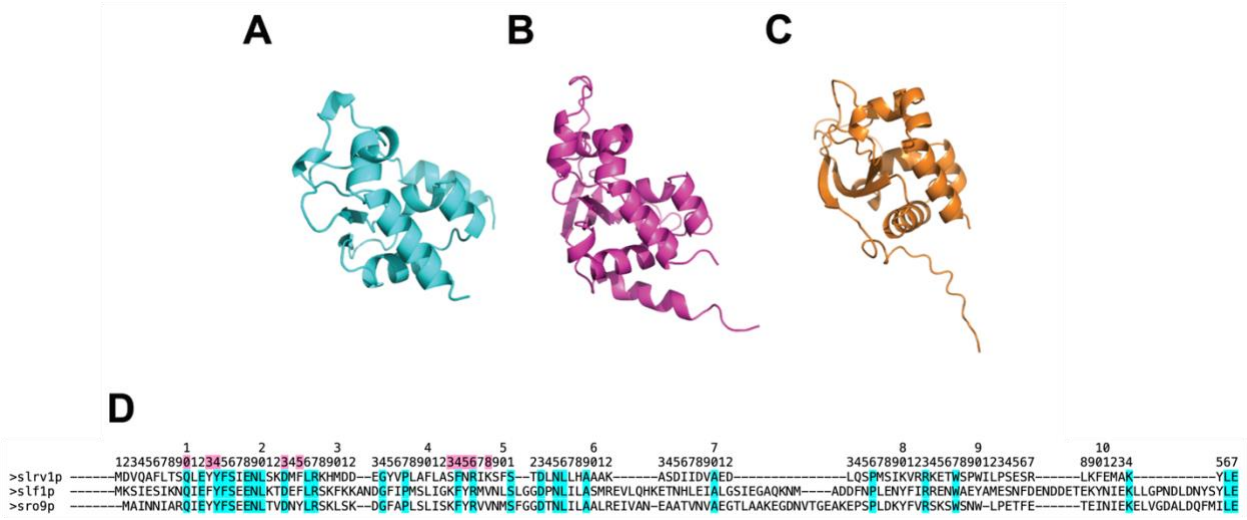

Figure 7. Alignment of Slr1p, Sro9p, and Slf1p structures and amino acid sequences. (A-C) Alignment of Slr1p (blue), Sro9p (purple), and Slf1p (orange). Structures generated with AlphaFold and displayed with pyMOL Opensource. **(B)** Alignment of Slr1p, Slf1p, and Sro9p sequences using BLAST. Residues highlighted in blue are shared across all proteins. Residue numbers highlighted in purple are hypothesized residues responsible for binding.

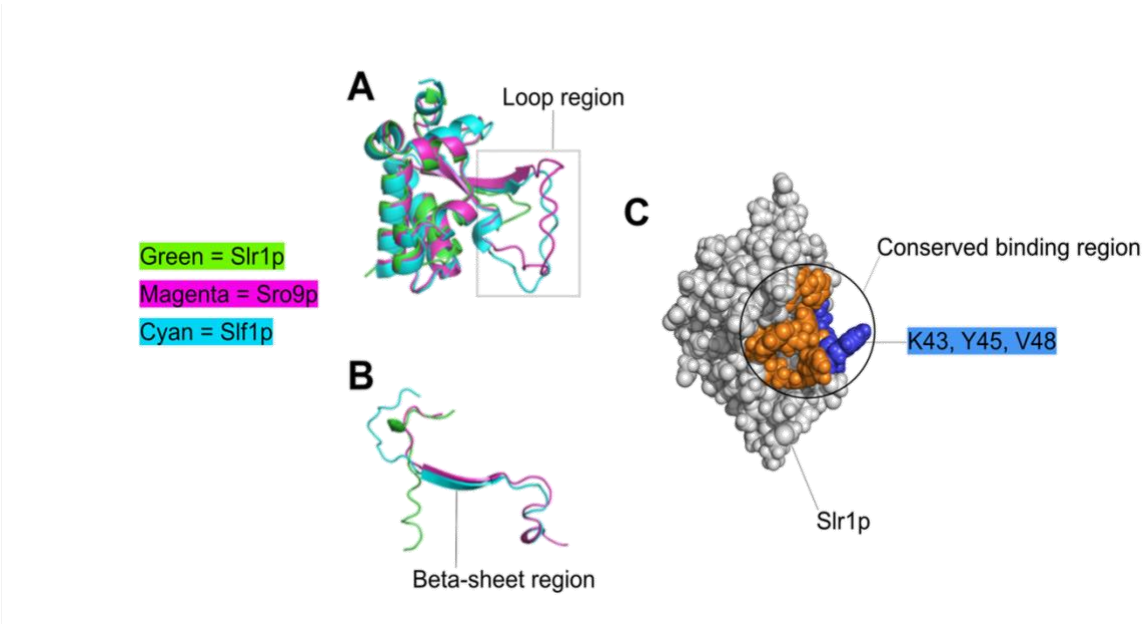

Figure 8. Comparison of Slr1p, Slf1p and Sro9p structures. (A) Alignment of Slr1p (green), Slf1 (cyan), and Sro9p (magenta) structures with the area boxed where Slr1p is missing a large loop that is seen in Slf1p and Sro9p. **(B)** Alignment of the beta-strand region shows that Slr1p is missing an entire beta strand that is seen within Sro9p and Slf1p. **(C)** Structure of Slr1p (without His-tag) with hypothesized conserved binding patch highlighted (Kozlov et al., 2022). Orange and blue residues are part of the active binding site. The blue residues represent the amino acids that differ between Sro9p and Slf1p proteins (K43, Y45, V48). All structures were generated using AlphaFold and displayed using pyMOL Open Source.

4.2 Expression and Purification of Proteins of Interest

4.2.1 Expression and purification of Slr1p

The Slr1p gene was transformed into *E. coli* BL21 electrocompetent cells, and a cryogenic stock was prepared and stored at −80 °C for subsequent experiments. Slr1p was expressed following a 3-hour induction at 37 °C with 1 mM IPTG. The 13.29 kDa protein was removed successfully using nickel affinity chromatography, followed by size exclusion chromatography, where most of the protein eluted between fractions B12-C10 that occurred between 70-85 minutes after the time of injection into the ÄKTA pure™ chromatography system (Figure 9). Storing the protein at -20 °C preserved its integrity for several months. Storage of the

protein under 4 °C conditions allowed the protein to be viable for upwards of one week before protein aggregation formed. Thus, storage at -20 °C was preferred.

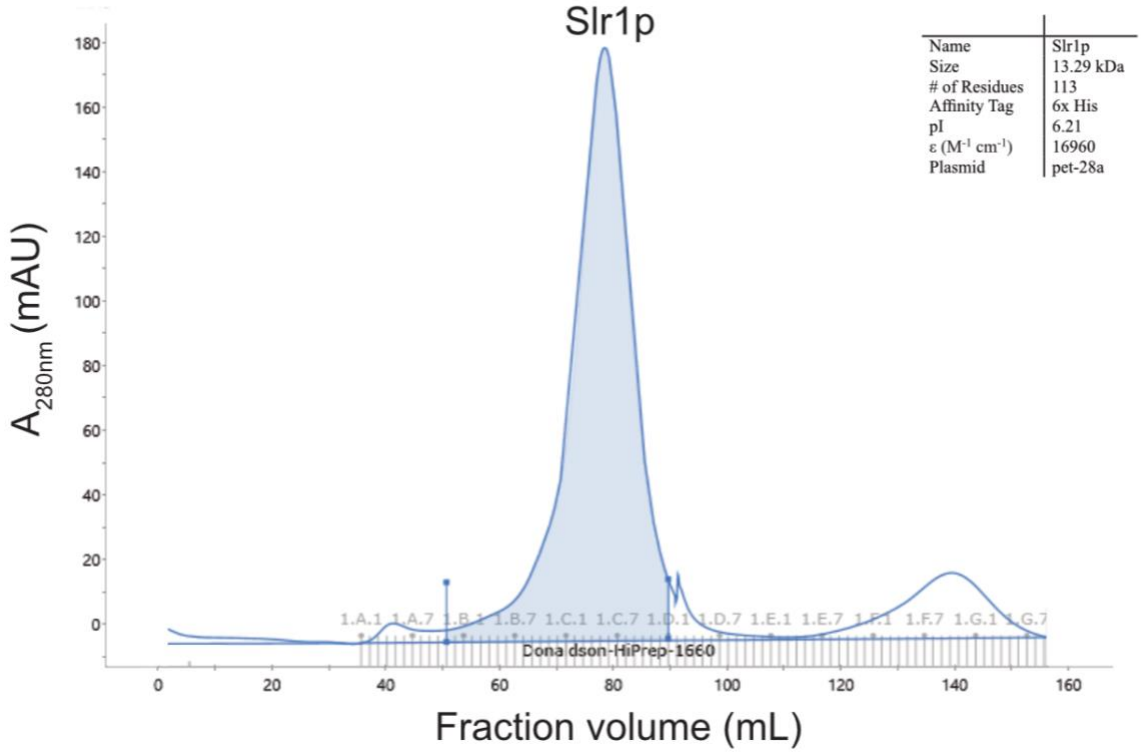

Figure 9. SEC elution profile of Slr1p. Obtained from the ÄKTA pure™ chromatography system, where all the protein was eluted between fractions A11 and C12. A table containing the chemical and structural properties of Slr1p is also displayed.

4.2.2 Expression and purification of Slf1p

The Slf1p gene was transformed into *E. coli* BL21 electrocompetent cells, and a cryogenic stock was prepared and stored at −80 °C for subsequent experiments. Slf1p was expressed following a 3-hour induction at 37 °C with 1 mM IPTG. However, changing the growth conditions (after induction) to 16 °C for overnight growth (16-18 hours) shifted the protein into a soluble state. The difference between these two growth conditions had little effect on the protein yield. The 17.80kDa protein followed the same purification protocol as Slr1p and

mostly eluted in fractions B5-C2 that occurred between 60-75 minutes after the time of injection into the ÄKTA pure™ chromatography system (Figure 10). Slf1p had the same storage conditions as Slr1p, which helped preserve the viability of the protein.

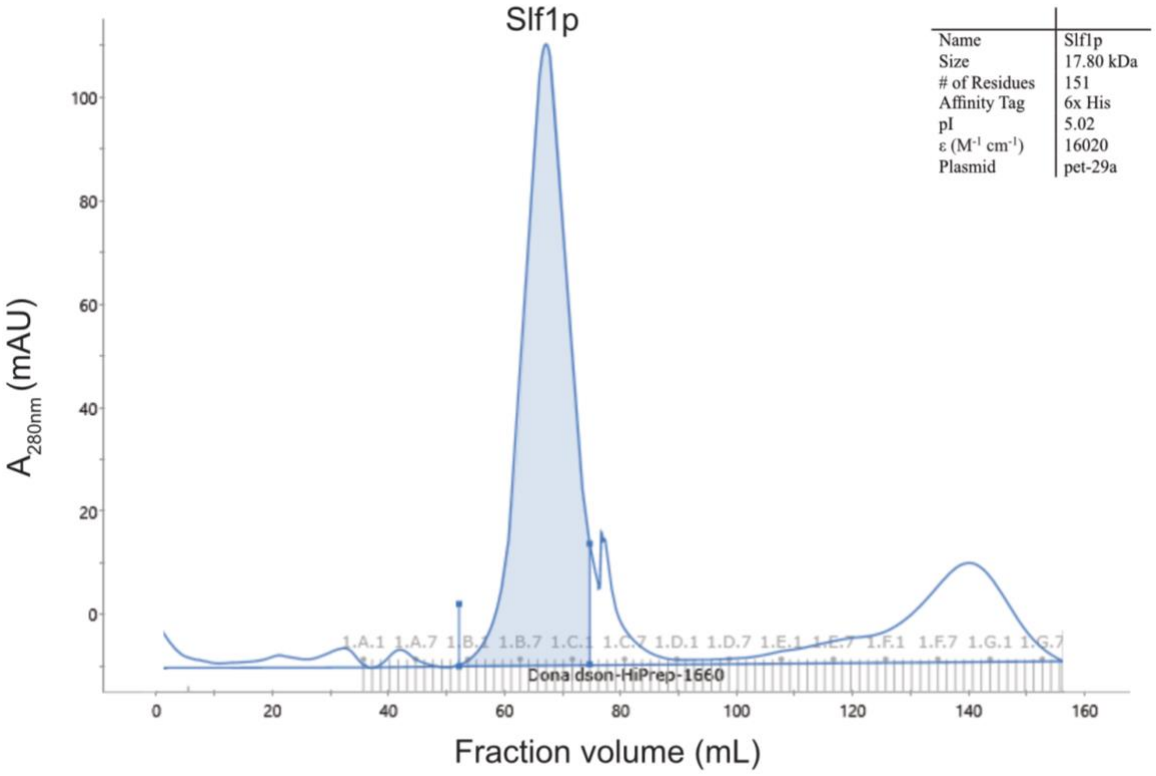

Figure 10. SEC elution profile of Slf1p. Obtained from the ÄKTA pure™ chromatography system, where all the protein was eluted between fractions A12 and C2. A table containing the chemical and structural properties of Slf1p is also displayed.

4.2.3 Expression and purification of Sro9p

The Sro9p gene was transformed into *E. coli* BL21 electrocompetent cells, and a cryogenic stock was prepared and stored at −80 °C for subsequent experiments. Slr1p was expressed following a 3-hour induction at 37 °C with 1 mM IPTG. Like Slf1p, Sro9p was insoluble when expressed under 37 °C conditions for 3 hours. Changing the growth conditions to 16 °C for overnight growth (16-18 hours) shifted the protein into a soluble state, just like what

was observed in Slf1p. However, overnight growth at 16 °C yielded less protein than a 3-hour growth at 37 °C. The 16.30 kDa protein was purified using the same protocol as Slr1p and Slf1p, eluting mostly in fractions B7 to C3 between 63 and 75 minutes following injection into the ÄKTA pure™ chromatography system (Figure 11). Sro9p had the same storage conditions as Slr1p and Slf1p but aggregated more quickly when stored at 4 °C compared to Slr1p and Slf1p.

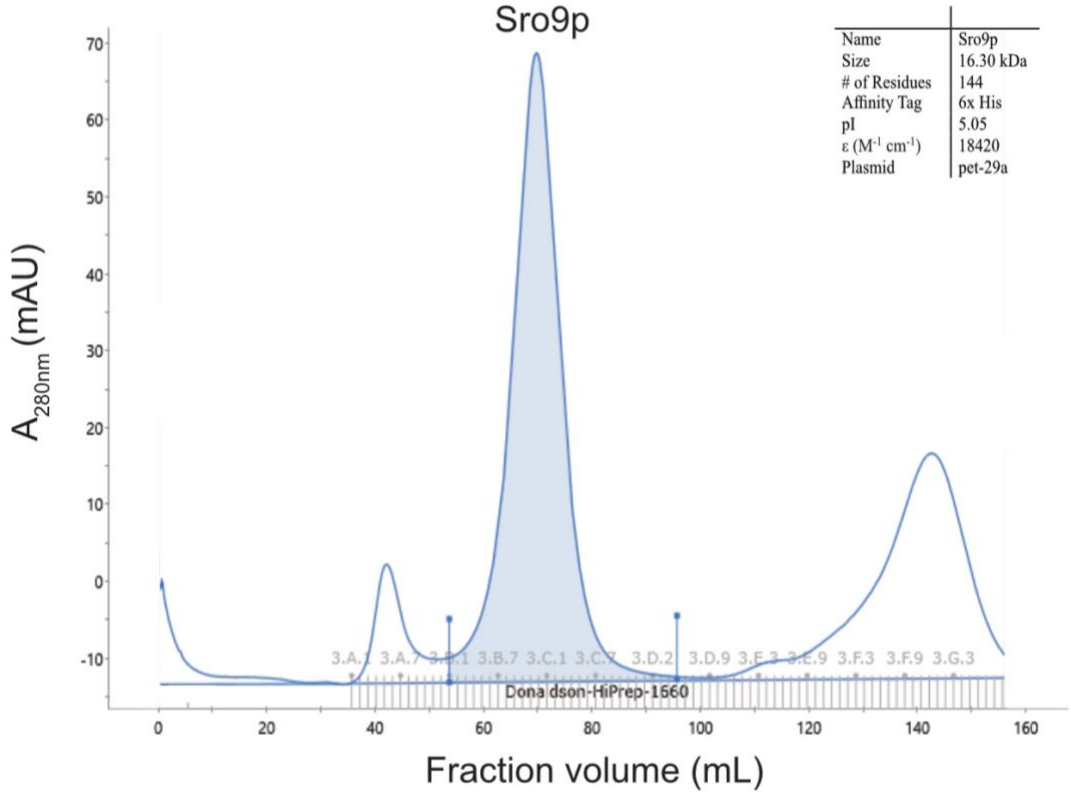

Figure 11. SEC elution profile of Sro9p. Obtained from the ÄKTA pure™ chromatography system, where all the protein was eluted between fractions B1 and D4. A table containing the chemical and structural properties of Sro9p is also displayed.

4.2.4 Visualization of Proteins on Gel

To observe the weight and integrity of the proteins, frozen samples of Slr1p, Slf1p and Sro9p were thawed out. Samples were mixed 1:1 with loading buffer, and 20 µL were loaded onto the gel, and electrophoresis was performed at 180 V for 40 minutes to ensure effective resolution of the protein bands. Sro9p displays one prominent band followed by a band that likely represents the dimer just beneath, while Slr1p and Slf1p have predominantly large single bands representative of the respective main protein (Figure 12). All bands are quite clear, indicating a strong presence of protein with little to no aggregation. Some smearing is observed, likely due to the high concentration of protein.

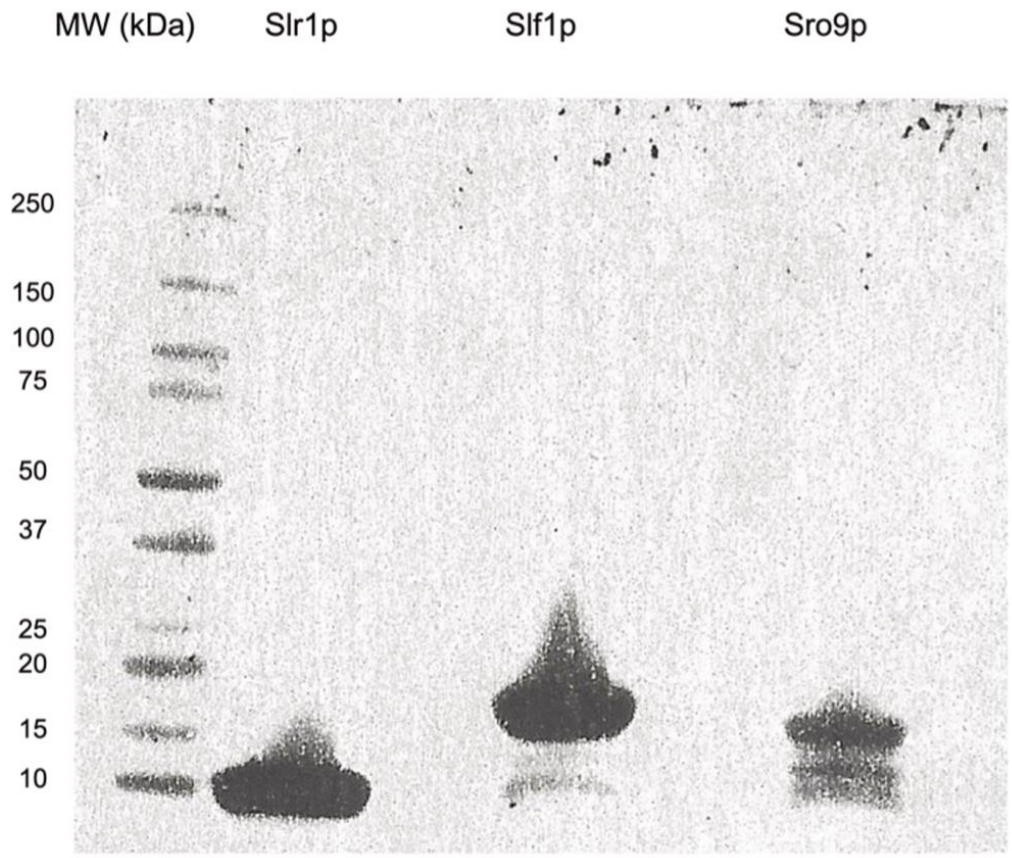

Figure 12. Bradford protein assay visualization of Slr1p (13.29 kDa), Slf1p (17.80 kDa) and Sro9p (16.30 kDa). The power supply was set at 180V for 40 minutes to achieve optimal separation, and the sample was then stained with Abcam Bradford Assay stain for 15 minutes. Imaging was performed with AlphaImager immediately after.

4.3 NMR spectra reveal an accurate structure model of Slr1p and the beta sheet-network in both Slr1p and Slf1p

4.3.1 Unbound Slr1p Structure

AlphaFold is an AI-based tool that accurately predicts protein structures from amino acid sequences (Jumper et al., 2021). It utilizes deep learning algorithms trained on known protein structures to model the spatial folding of proteins. The AlphaFold predicted structure of Slr1p was viewed, analyzed and modified using pyMOL Opensource. Secondary structures and inter-residual connections were further analyzed using 3D ^{15}N and ^{13}C edited NOESY spectra (Figure 13). The conjunction of the AlphaFold structure with the NMR spectra allowed for an accurate identification of which secondary structure residues were participating in and where they were on the structure. This structure was revealed to have several secondary structures, including six alpha-helices, three beta-sheet regions, and one 3_{10} alpha helix (Figure 13).

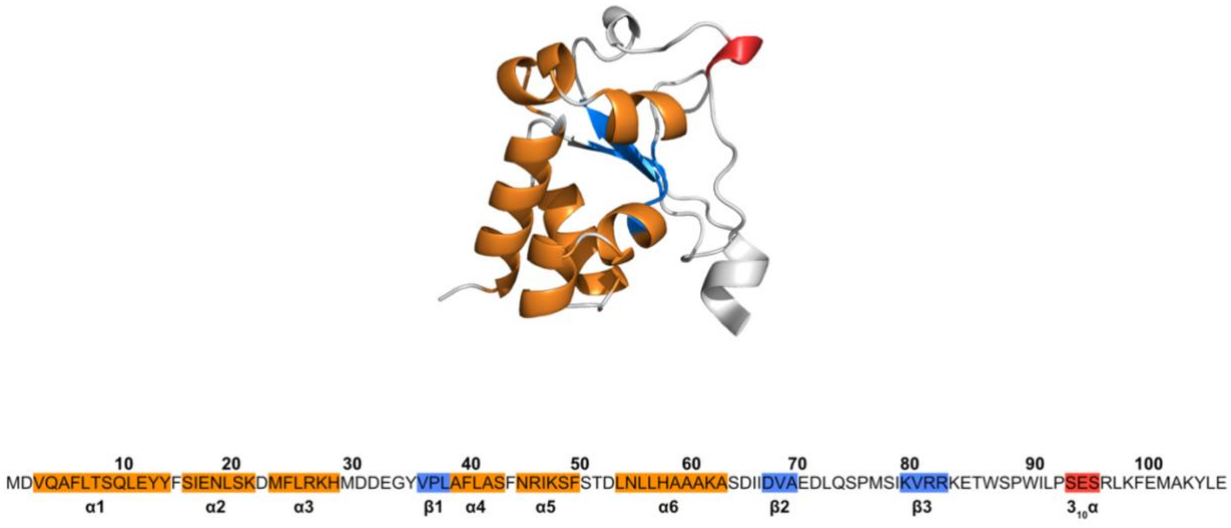

Figure 13. Unbound structure of Slr1p. The AlphaFold predicted structure of Slr1p displays and provides information on which residues are participating in secondary structures. These structures were confirmed with the use of ^{15}N and ^{13}C edited 3D NOESY spectra. Blue residues are within the beta-sheet structure, orange residues are within alpha-helices, and red residues are within a 3_{10} alpha helix.

4.3.2 Assignment of Identifiable Protein Backbone Residues

Assignment of the backbone residues within the collected NMR spectra is an essential part of understanding the structure of a protein. Assignment of residues used CcpNMR software. Utilizing ^{1}H-^{15}N HSQC, HNCO, HN(CA)CO, CBCA(CO)NH/HN(CO)CACB, and CBCANH/HNCACB, the atoms within amide groups (including nitrogen, alpha and beta carbons, and carbonyl carbons) can be identified. The strategy involves aligning the alpha and beta carbon peaks from the preceding amide group (CBCA(CO)NH/HN(CO)CACB) with the alpha and beta carbons of the selected amide group (CBCANH/HNCACB) (Figure 14). A similar strategy is employed to identify the carbonyl carbon of an amide by aligning the carbonyl carbon from the preceding amide group (HN(CA)CO) with the selected amide group (HNCO)

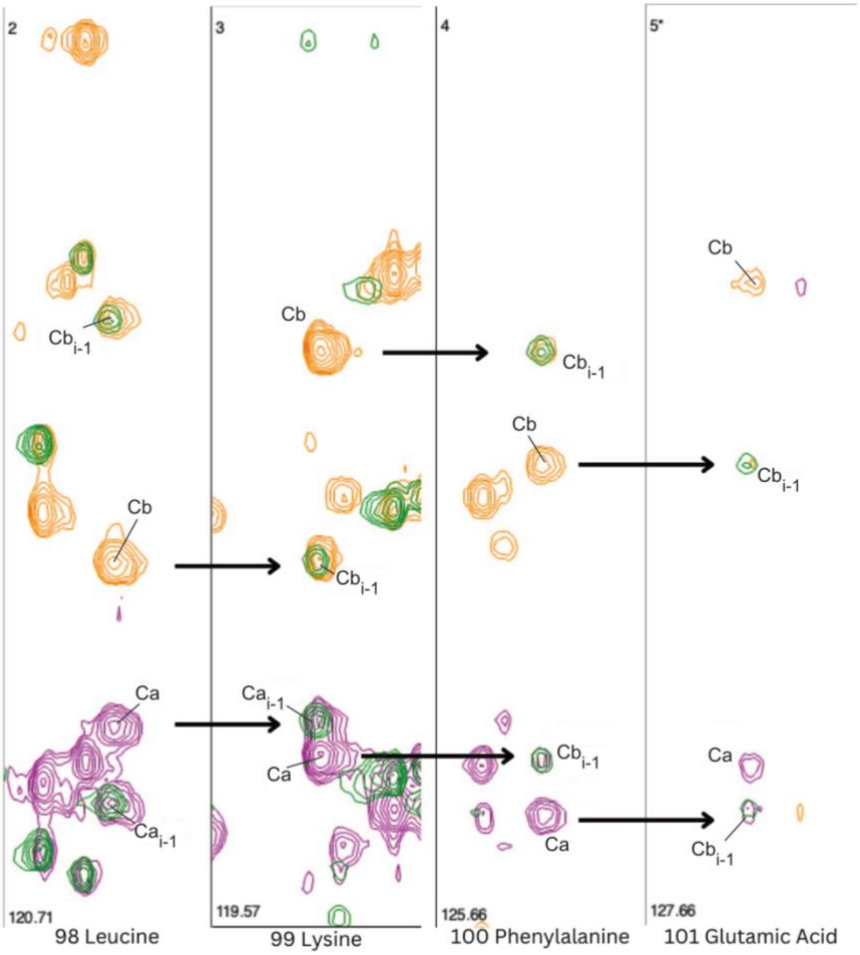

Figure 14. Alpha and beta carbons of amide residues. CBCA(CO)NH/HN(CO)CACB (green) and CBCANH/HNCACB (purple and yellow) of residues 98-101 in unbound Slr1p displayed using CcpNMR. CBCANH/HNCACB shows the alpha and beta carbons of the selected amide within the strip, while the CBCA(CO)NH/HN(CO)CACB highlights the alpha and beta carbons from the preceding amide.

4.3.3 Beta sheet network of Slr1p

The predicted AlphaFold structure, along with the resulting 3D ^{15}N- and ^{13}C-edited NOESY spectra of Slr1p, reveals a network of interactions involving residues 36-38, 68-70, and 80-83. The ^{15}N and ^{13}C edited 3D NOESY spectra were used to accurately observe H-bonds, NH-NH bonds, NH-HA bonds, and HA-HA bonds to investigate the accuracy of the predicted structure (Figures 15 & 16). The beta sheet network observed within the NMR spectra is almost identical to the predicted beta-sheet bonds within the AlphaFold structure.

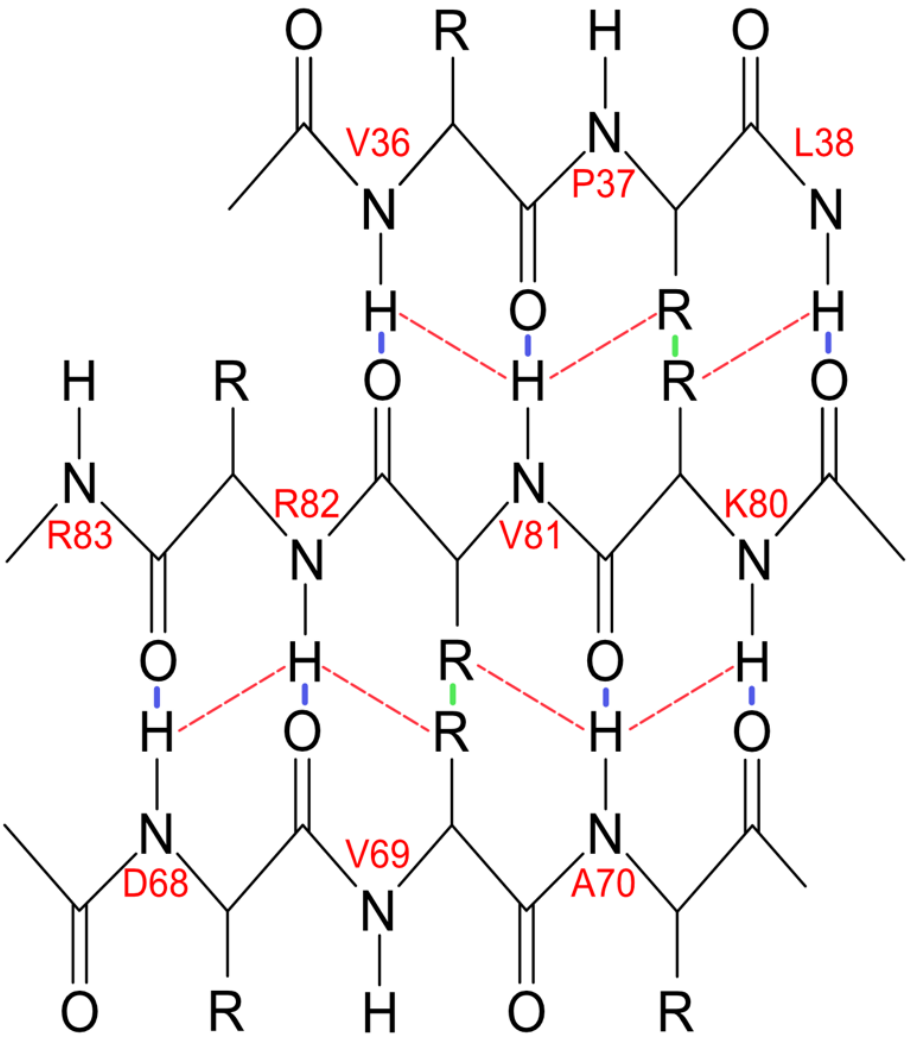

Figure 15. Beta-sheet network within Slr1p. Blue: hydrogen bond, red: NH-NH and NH-HA bonds, green: HA-HA bonds. Connections were observed and verified with the Slr1p AlphaFold predicted structure.

Figure 16. NOE restraints showing beta sheet connections in Slr1p. (A) ^{15}N edited 3D NOESY strips of residues involved in the beta sheet network, showcasing NH-NH and NH-HA/B connections. **(B)** ^{13}C edited 3D NOESY strips of residues involved in the beta sheet network, showcasing HA-HA connections.

4.3.4 Unbound Slf1p Structure

The structure of the unbound Slf1p protein was examined using a combination of computational prediction and experimental validation methods. The predicted AlphaFold structure was analyzed using the STRIDE algorithm, which assesses all residues of a protein in its .pdb format to determine their participation in secondary structures. These assignments were mostly corroborated with data from ^{15}N and ^{13}C edited 3D NOESY NMR spectra, which helped confirm the presence and positioning of various secondary structures. Analysis using these methods revealed that the predicted structure of Slf1p contains several secondary structural elements, including six alpha-helices, four beta-sheet regions, and two 3_{10} alpha helices (Figure 17A).

TALOS+ was used to predict local backbone conformations based on HN, CO, CB, CB, and HA chemical shift assignments from NMR spectra. The analysis indicated that most assigned residues were classified as "good," reflecting high confidence in their conformational stability within the protein structure. There are some regions of the protein that TALOS+ classified as "dynamic", suggesting that it does not conform well to known patterns of secondary structure (Figure 17B). Most often, these residues with a dynamic classification are found within loop regions and flexible N- and C-terminal tails. These areas lack the regular hydrogen bonding and side-chain packing seen in well-folded secondary structures, making their chemical environment more variable and less predictable.

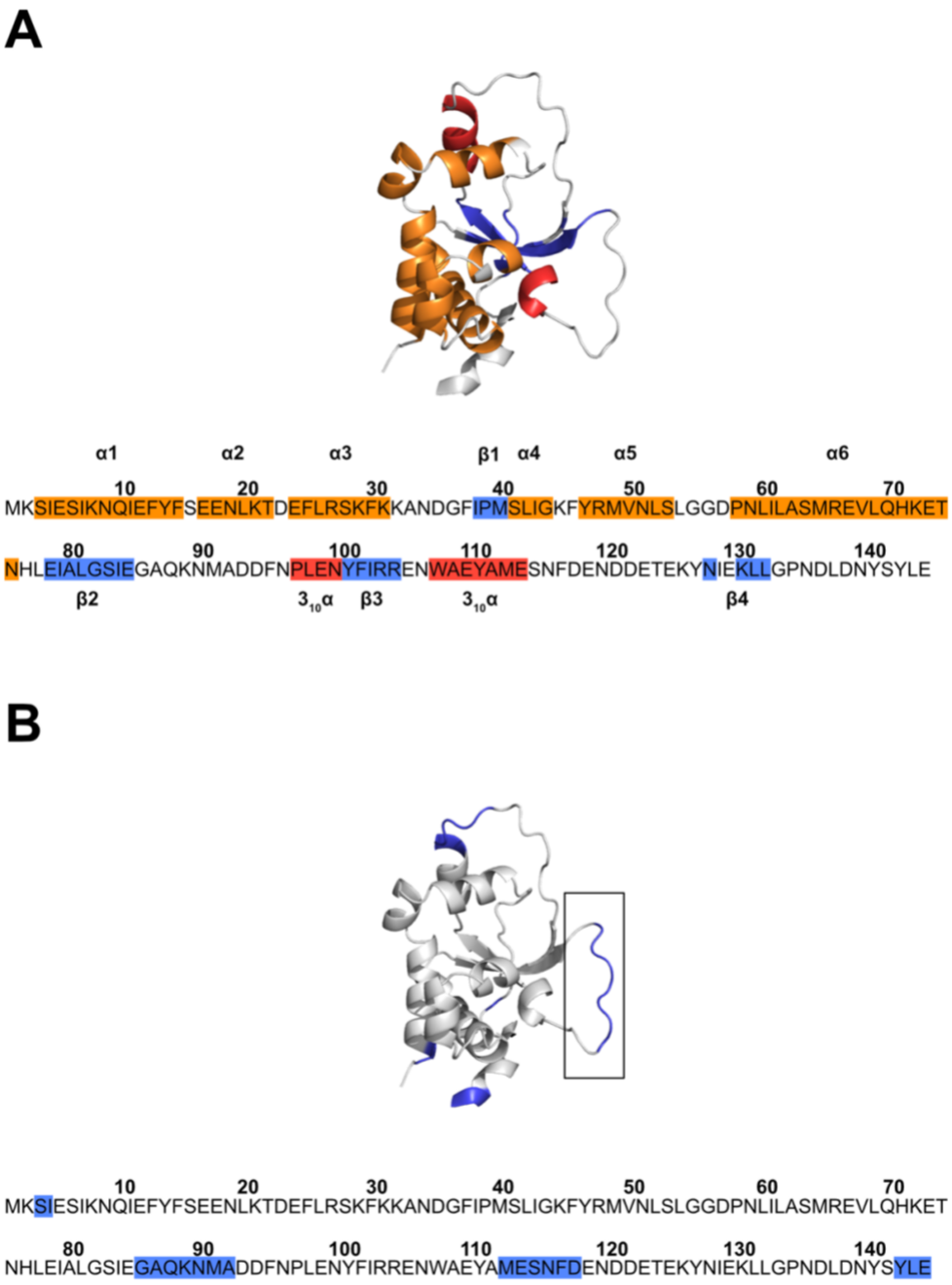

Figure 17. Unbound structure of Slf1p including TALOS+ analysis. (A) The AlphaFold predicted structure of Slf1p provides information on which residues are participating in secondary structures. These structures were confirmed with the use of ^{13}C and ^{15}N edited 3D NOESY spectra. Blue residues are within the beta-sheet structure, orange residues are within alpha-helices, and red residues are within a 3_{10} alpha helix. **(B)** TALOS+ was used to determine the backbone torsion angles using the backbone assignments of identifiable residues within NMR spectra. Some residues, mainly clustered in loop regions or towards the N- and C-terminal tails, were classified as "dynamic". These residues are highlighted in blue, and the loop where most of the dynamic residues reside is outlined with a black box.

4.3.5 Beta sheet network of Slf1p

Analogous NMR experiments to those performed on Slr1p were carried out on Slf1p. An accurate structure of Slf1p could not be calculated because the peaks within the spectra, mainly the ^{15}N-HSQC, were broadened. Changes in the electronic environment alter the local magnetic field experienced by a nucleus, causing small shifts in its precession frequency away from the 700 MHz Larmor frequency of ^{1}H. Other aspects of the structure of Slf1p were accurately determined, including the beta-sheet network. The predicted AlphaFold structure and resulting ^{15}N and ^{13}C edited 3D NOESY spectra of Slf1p reveal that there are a series of connections involving residues: 38-40, 78-85, 101-105, 128, 131-133 (Figures 18 & 19). The extra beta sheet within Slf1p that was predicted to exist in the AlphaFold structure was confirmed with the use of the ^{15}N and ^{13}C edited 3D NOESY spectra, with a bulge and disconnect of the sheet between amide residues of I129 and E130 within Slf1p.

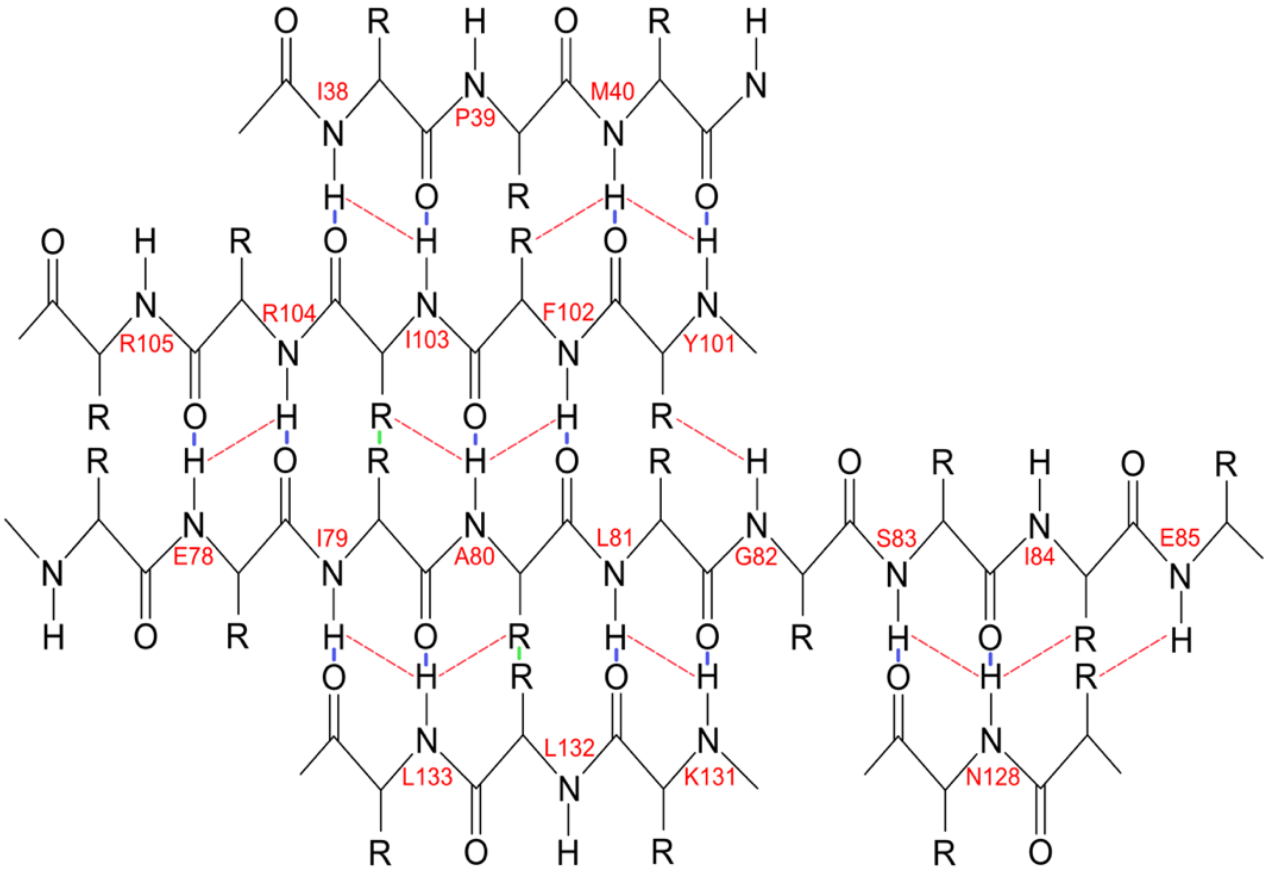

Figure 18. Beta-sheet network within Slf1p. Blue: hydrogen bond, red: NH-NH and NH-HA bonds, green: HA-HA bonds. Connections were observed and verified with the Slr1p AlphaFold predicted structure.

A

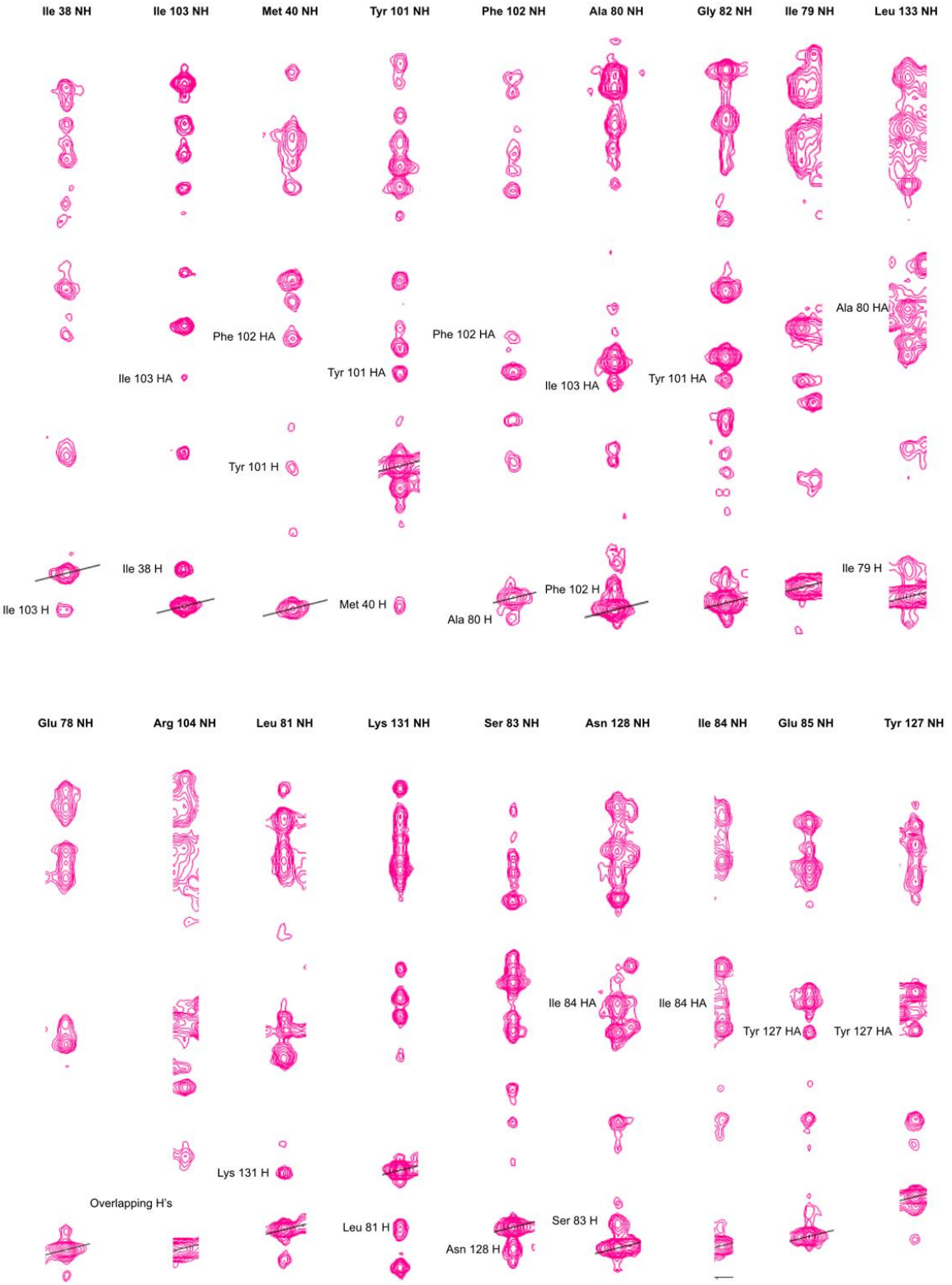
Ile 38 NH
Ile 103 NH
Met 40 NH
Tyr 101 NH
Phe 102 NH
Ala 80 NH
Gly 82 NH
Ile 79 NH
Leu 133 NH
Phe 102 HA
Ile 103 HA
Tyr 101 HA
Tyr 101 H
Phe 102 HA
Ile 103 HA
Tyr 101 HA
Ala 80 HA
Ile 38 H
Ile 103 H
Met 40 H
Ala 80 H
Phe 102 H
Ile 79 H
Glu 78 NH
Arg 104 NH
Leu 81 NH
Lys 131 NH
Ser 83 NH
Asn 128 NH
Ile 84 NH
Glu 85 NH
Tyr 127 NH
Ile 84 HA
Ile 84 HA
Tyr 127 HA
Tyr 127 HA
Lys 131 H
Overlapping H's
Leu 81 H
Asn 128 H
Ser 83 H

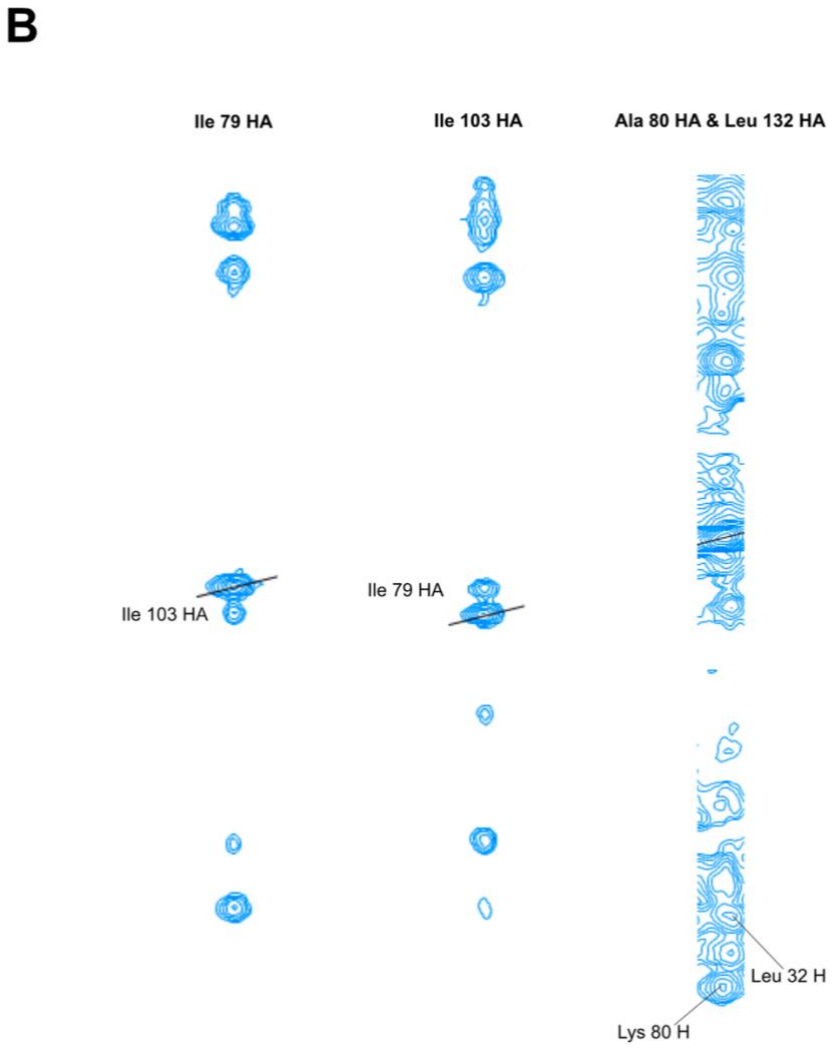

Figure 19. NOE restraints showing beta sheet connections in Slf1p. (A) ^{15}N edited 3D NOESY strips of residues involved in the beta-sheet network, showcasing NH-NH and NH-HA/B connections. **(B)** ^{13}C edited 3D NOESY strips of residues involved in the beta-sheet network showcasing HA-HA connections.

Table 14. Beta-sheet connections within Slr1p and Slf1p.

Protein	# of NH-NH bonds	# of NH-HA bonds	# of HA-HA bonds
Slr1p	3	4	2
Slf1p	7	6	2

4.4 Slr1p, Slf1p and Sro9p all predominately consist of alpha-helical structures

A CD-spectroscopy assay was conducted with all three proteins to investigate their secondary structures in solution by examining the difference in absorbance of right and left circularly polarized light. All CD spectroscopy assays were performed at 20 °C, with the wavelength (nm) measured between 200-250 nm, where secondary structures are typically observed. Optimal protein concentrations for analysis were 10 μM for Slf1p and Sro9p, and 30 μM for Slr1p, all prepared in PBS buffer (10 mM sodium phosphate, 60 mM NaCl, pH 7.4). The CD data indicates that all three proteins, Slr1p, Slf1p, and Sro9p exhibit predominantly alpha-helical structures, as evidenced by a characteristic spectrum featuring a strong negative band around 222 nm and another negative band around 208 nm (Figure 20A-C). This aligns with the predicted structures of all three proteins, which show a higher number of residues participating in alpha-helix structures compared to beta-sheet structures. This finding is further supported by secondary structure analysis using STRIDE. This analysis reveals that all proteins comprise 9%-17% of their structure in the form of beta-sheets, 35%-49% of residues in alpha helices, and 5% of their structure as 3_{10} helices (Figure 20D-F). Both Slf1p and Sro9p contain a greater percentage of their structure dedicated to beta-sheets, which is visually apparent in the predicted structures. Additionally, another dataset was collected following the thermal denaturation of each protein, achieved by melting the proteins up to 90 °C. This reveals that none of the proteins refold, and they lose their secondary structure because they do not exhibit strong negative bands characteristic of them (Figure 20A-C).

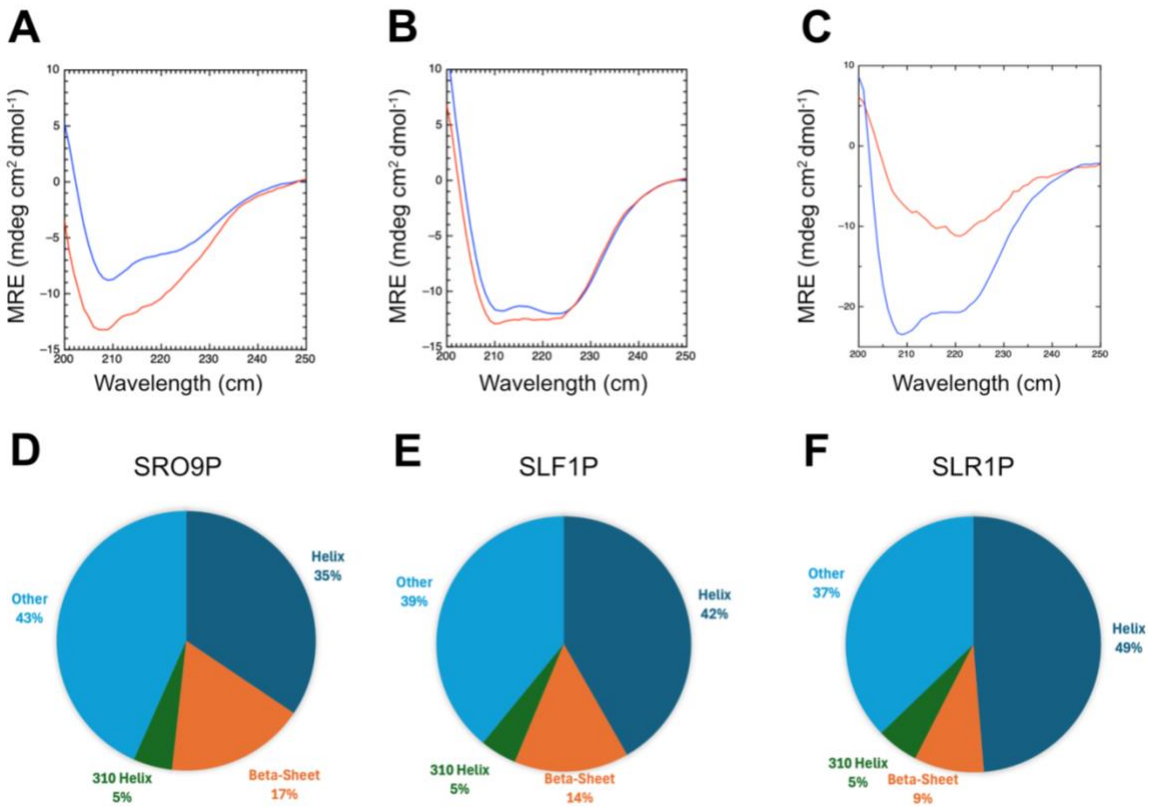

Figure 20. CD spectra and secondary structure composition of Sro9p, Slf1p and Slr1p. CD spectra of: **(A)** Sro9p (blue = post-melt, red = pre-melt), **(B)** Slf1p (blue = pre-melt, red = post-melt), and **(C)** Slr1p (blue = pre-melt, red = post-melt). The CD experiments were conducted at wavelengths between 200 and 250 nm with protein samples consisting of PBS (10 mM sodium phosphate, pH 7.4, 60 mM NaCl). The STRIDE algorithm was used to determine secondary structure composition for **(D)** Sro9p, **(E)** Slf1p and **(F)** Slr1p (Frishman & Argos, 1995).

4.5 Thermostability of Slr1p, Slf1p and Sro9p

DSC was performed on Slr1p, Slf1p, and Sro9p to calculate thermal transition temperatures and derive thermodynamic characteristics, specifically enthalpy. The resulting melting point data show that Sro9p has the lowest melting point with 36.2 ± 0.9 °C, followed by Slf1p at 46.9 ± 0.3 °C and Slr1p at 53.1 ± 0.5 °C (Figure 21). These melting points show that Sro9p is the least thermally stable, while Slr1p has the highest thermal stability. The enthalpy of the reaction was quantitatively determined by measuring the area enclosed by each peak in the data. The enthalpy values of Slr1p are the highest, with a value of 57.8 ± 4.7 kcal/mol, followed

by Slf1p at 50.0 ± 5.6 kcal/mol, and Sro9p has the lowest at 35.5 ± 7.2 kcal/mol (Figure 21A-C). All the enthalpy values show an endothermic transition from a folded to an unfolded state, in which the system takes in heat from the environment, raising the enthalpy value. Entropy values at 20 °C show a similar pattern with Slr1p having the highest at 5.9 ± 0.5 kcal/mol followed by Slf1p (4.2 ± 0.5 kcal/mol) and Sro9p (1.9 ± 0.4 kcal/mol). Strong intermolecular forces and secondary structures within the protein have significant stabilizing interactions (hydrogen bonds, van der Waals forces, hydrophobic interactions, and disulfide bonds) that must be broken to denature it, thus increasing the enthalpy value and the melting point. Sro9p has the lowest percentage of secondary structures out of the three proteins (57%), followed by Slf1p (61%) and then Slr1p (63%) (Figure 20D-F). This follows the same order of the melting points and enthalpy values of the protein, further supporting the role of secondary structures within the thermal stability of the proteins.

An additional set of DSC experiments was conducted with 6A to examine the stability of the proteins when they are bound. All melting points and enthalpy values increased when the proteins were bound to 6A. The melting point for Slr1p + 6A was the highest at 65.0 ± 1.1 °C, followed by Slf1p + 6A (54.8 ± 0.3 °C) and Sro9p + 6A (45.4 ± 0.6 °C) (Figure 21D-F). The enthalpy values follow the same pattern with Slr1p + 6A showing the highest enthalpy value of 95.2 ± 9.7 kcal/mol, followed by Slf1p + 6A (73.1 ± 6.6 kcal/mol) and Sro9p + 6A (58.1 ± 8.8 kcal/mol) (Figure 21). The same pattern is seen with the entropy values with Slr1p + 6A at 12.7 ± 1.3 kcal/mol followed by Slf1p + 6A (7.8 ± 0.7 kcal/mol) and Sro9p + 6A (4.6 ± 0.7 kcal/mol). The increase in both the melting point and enthalpy values of the proteins bound to 6A indicates that the binding event has a stabilizing effect on all proteins, with Slr1p + 6A showing the greatest stabilizing effect when in its bound form.

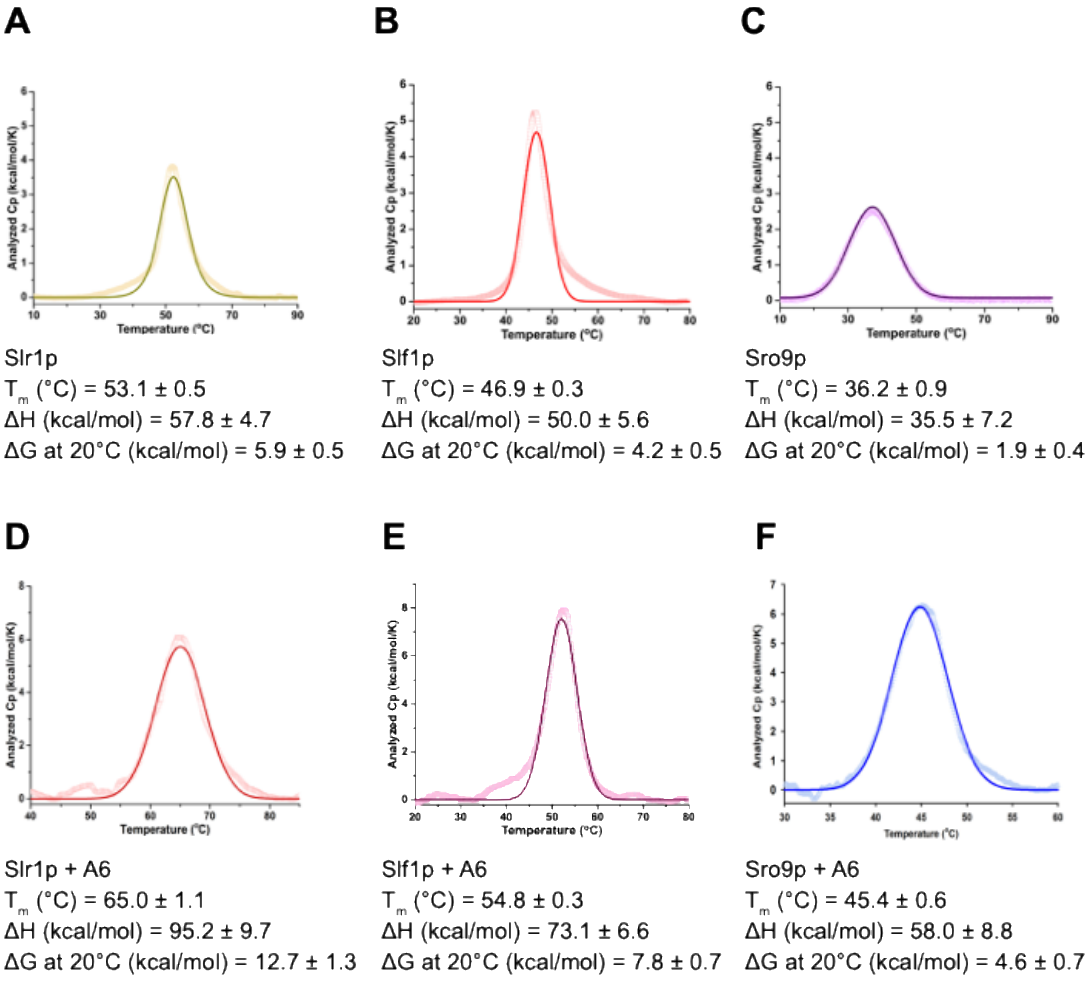

Figure 21. Differential scanning calorimetry of Slr1p, Slf1p and Sro9p to test for T_m and enthalpy. Specific heat capacity was measured over a temperature range (10 °C - 90 °C), and enthalpy, Tm values, and entropy value at 20 °C (protein is intrinsically stable at this temperature) were accounted for **(A)** Slr1p, **(B)** Slf1p, **(C)** Sro9p, **(D)** Slr1p + 6A, **(E)** Slf1p + 6A, and **(F)** Sro9p + 6A.

4.6 Residues participating in binding are shared between RNA6 and RNA15

4.6.1 Binding titrations of Slr1p with RNA6 and RNA15

A 1:1 molar ratio titration of RNA6 and RNA15 with Slr1p was performed, and a series of NMR spectra were collected, including a ^{15}N-HSQC. This titration was done to examine the specific residues that participate in ligand binding through CSP. The CSP data from the ^{15}N-

HSQC spectra was obtained by exporting the weighted chemical shift perturbations of assigned residues of the unbound and bound spectra. Using the CSP formula, a value in ppm was obtained from each assigned residue. Significant perturbations in the protein's resonances were observed upon ligand binding. Residues with a CSP value equal to or greater than 0.1 ppm are considered significant. The residues with high CSP values when the titrated with RNA6 are: L7, T8, S9, F15, S16, E18, K22, L41, I47, S49, F50, S51, and L57 (Figure 22). Notably, residues exhibiting large chemical shift changes are concentrated in the alpha-helices, particularly the first one, suggesting that these areas directly contribute to the binding interface. The distribution of CSPs across the protein sequence also highlights areas where ligand binding might induce conformational changes in distal regions.

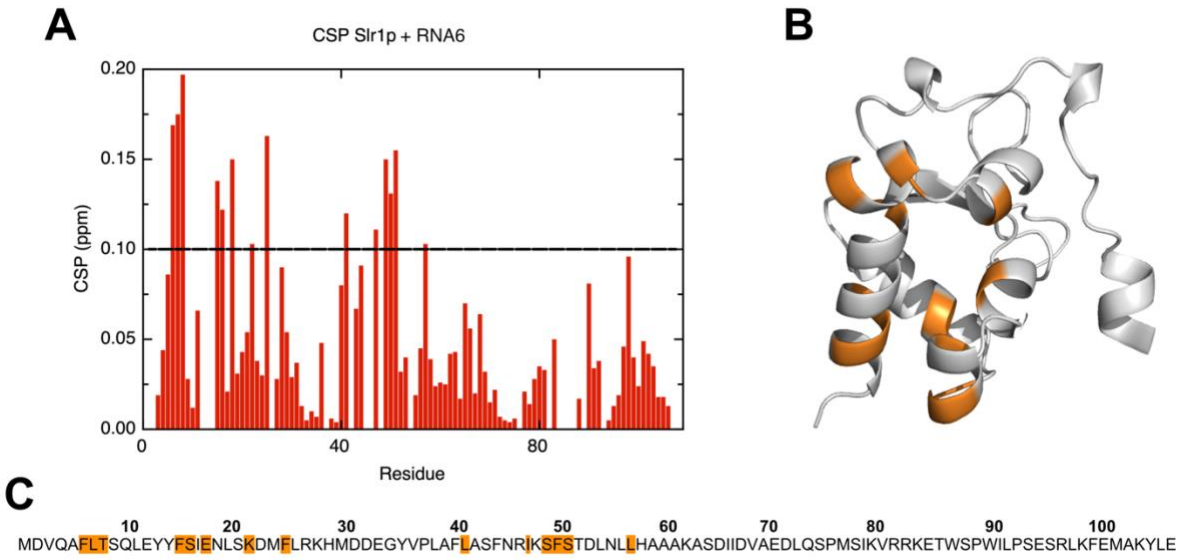

Figure 22. CSP of Slr1p and RNA6, derived from the assigned amide resonances in ^{15}N-HSQC NMR spectra. (A) CSP values corresponding to each amide resonance observed and assigned on the NMR spectra. **(B)** Residues with CSP values of 0.1 ppm and greater are highlighted in orange on the predicted AlphaFold structure of Slr1p and **(C)** the Slr1p sequence chain. Residues with significant CSP are highlighted.

Comparing the two ^{15}N-HSQC spectra between titrations of RNA6 and RNA15 shows little difference in the chemical shifts of the peaks between the bound and unbound residues. Many amide peaks with large CSP values from the RNA6 titration are also observed to be active in the binding of RNA15, including F6, L7, T8, F15, S16, E18, F22, F25, F40, L41, K48, S49, S51, and L57 (Figures 22 - 25). Residues with significant CSP have lines traced between their unbound and bound peaks.

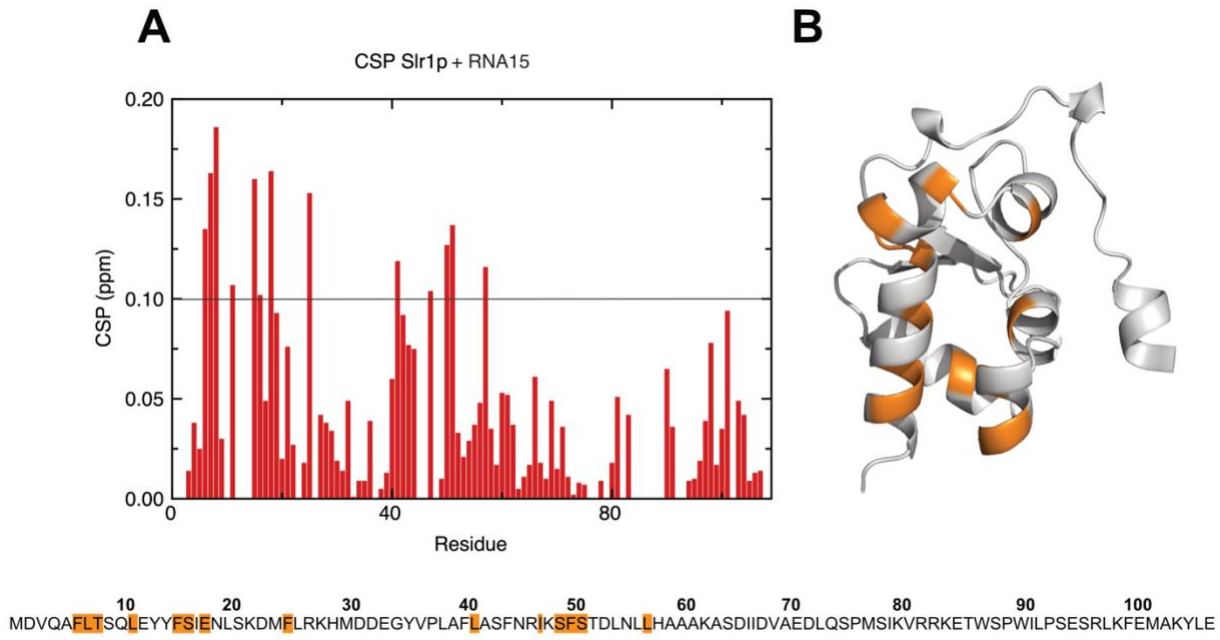

Figure 23. CSP of Slr1p and RNA15, derived from the assigned amide resonances in ^{15}N-HSQC NMR spectra. (A) CSP values corresponding to each amide resonance observed and assigned on the NMR spectra. **(B)** Residues with CSP values of 0.1 ppm and greater are highlighted in orange on the predicted AlphaFold structure of Slr1p and **(C)** the Slr1p LaM sequence chain. Residues with significant CSP are highlighted.

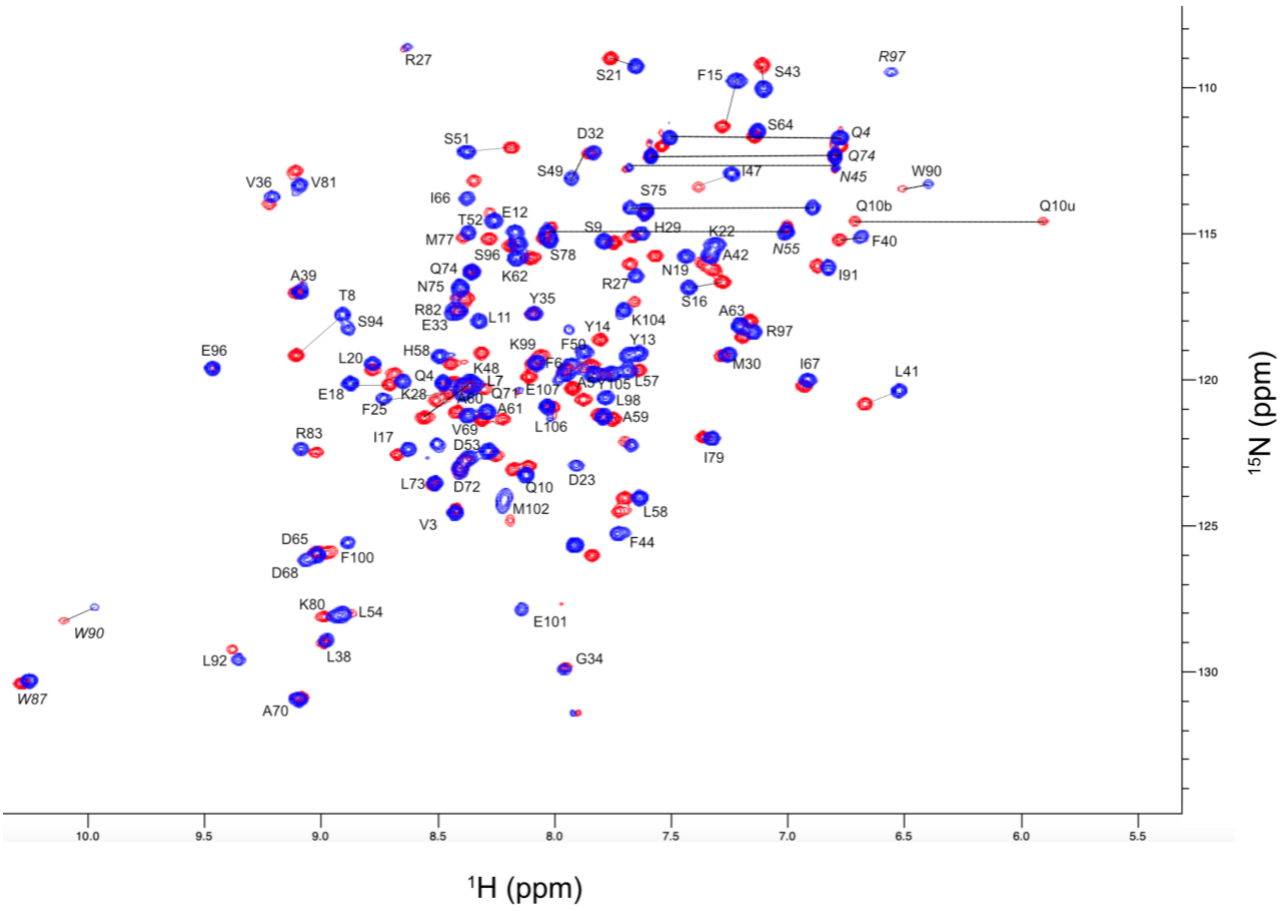

Figure 24. ^{15}N-HSQC of Slr1p with amino acid residues labelled (red = unbound, blue = bound to RNA15 at 1:1 ratio). The experiment was carried out at 298 K. Afterwards, the spectral data was processed and displayed using CcpNMR.

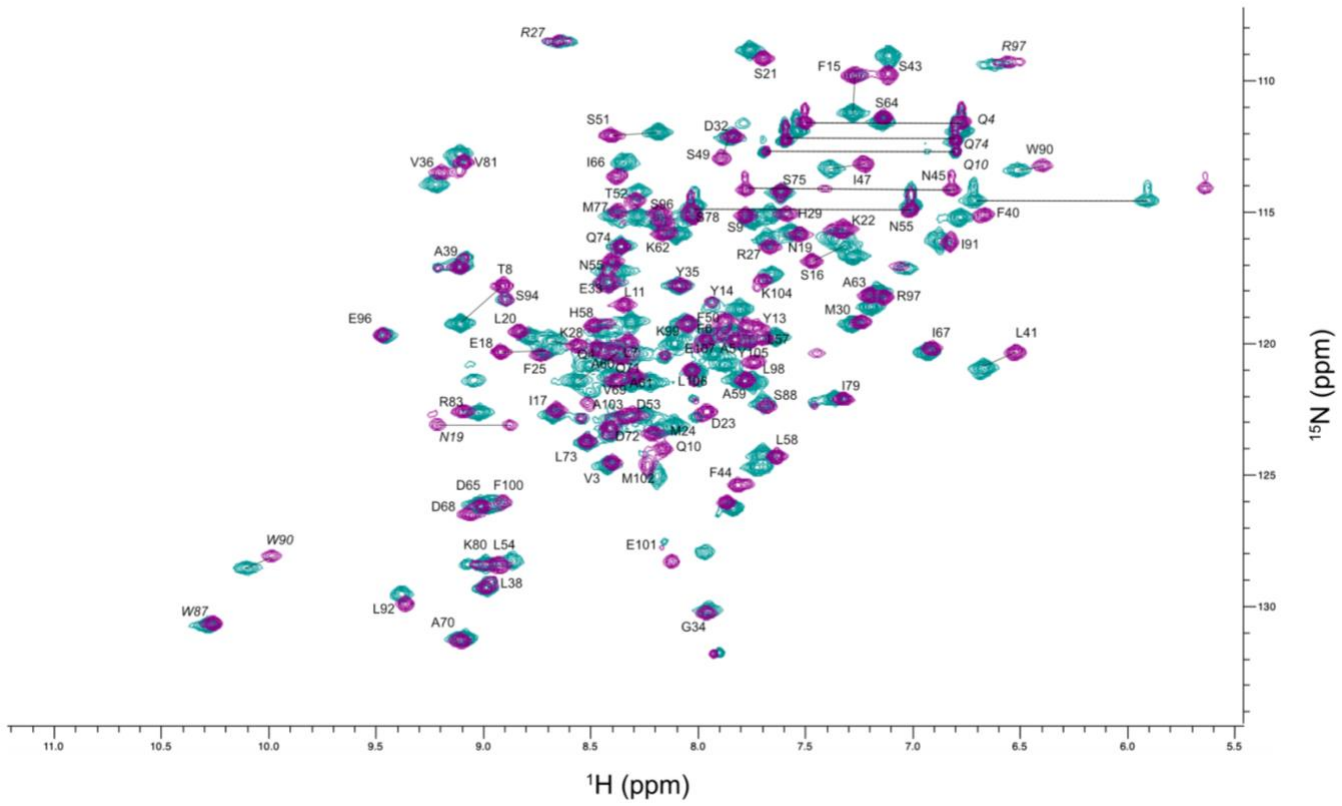

Figure 25. ^{15}N-HSQC of Slr1p with amino acid residues labelled (blue = unbound, purple = bound to RNA6 at 1:1 ratio). The experiment was carried out at 298 K. Afterwards, the spectral data was processed and displayed using CcpNMR.

Weighted chemical shift perturbations were also observed with the methyl carbons in ^{13}C-HSQC NMR datasets (Slr1p + RNA6, Slr1p + RNA15) (Figures 26 & 27). Near identical CSP are seen in the NMR spectra between Slr1p + RNA6 and Slr1p + RNA15. There are six methyl carbon resonances that have significant CSP values (CSP ≥ 0.2 ppm): L11HD2, L26HD2, L41HD2, I47HD1, L57HD2, and V81HG2 (Figure 28A-B). This suggests that the methyl carbons interacting with RNA6 are also the same when Slr1p is bound to RNA15. These methyl carbons are clustered in the central alpha-helical dominant core (Figure 28C).

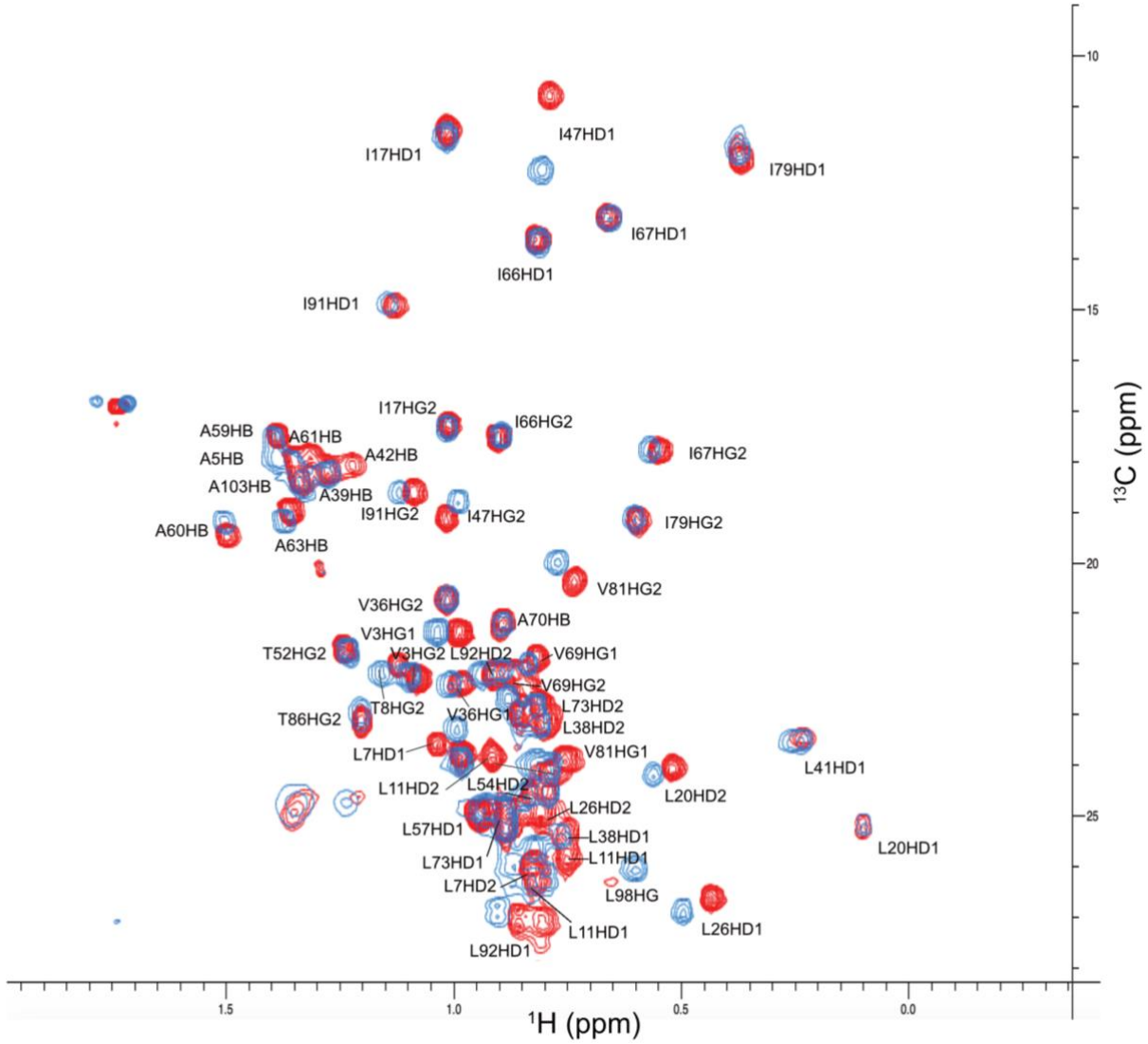

Figure 26. ^{13}C-HSQC spectra of Slr1p in the free (red) form and the bound (blue) form to RNA6. The experiment was carried out at 298 K. Afterwards, the spectral data was processed and displayed using CcpNMR.

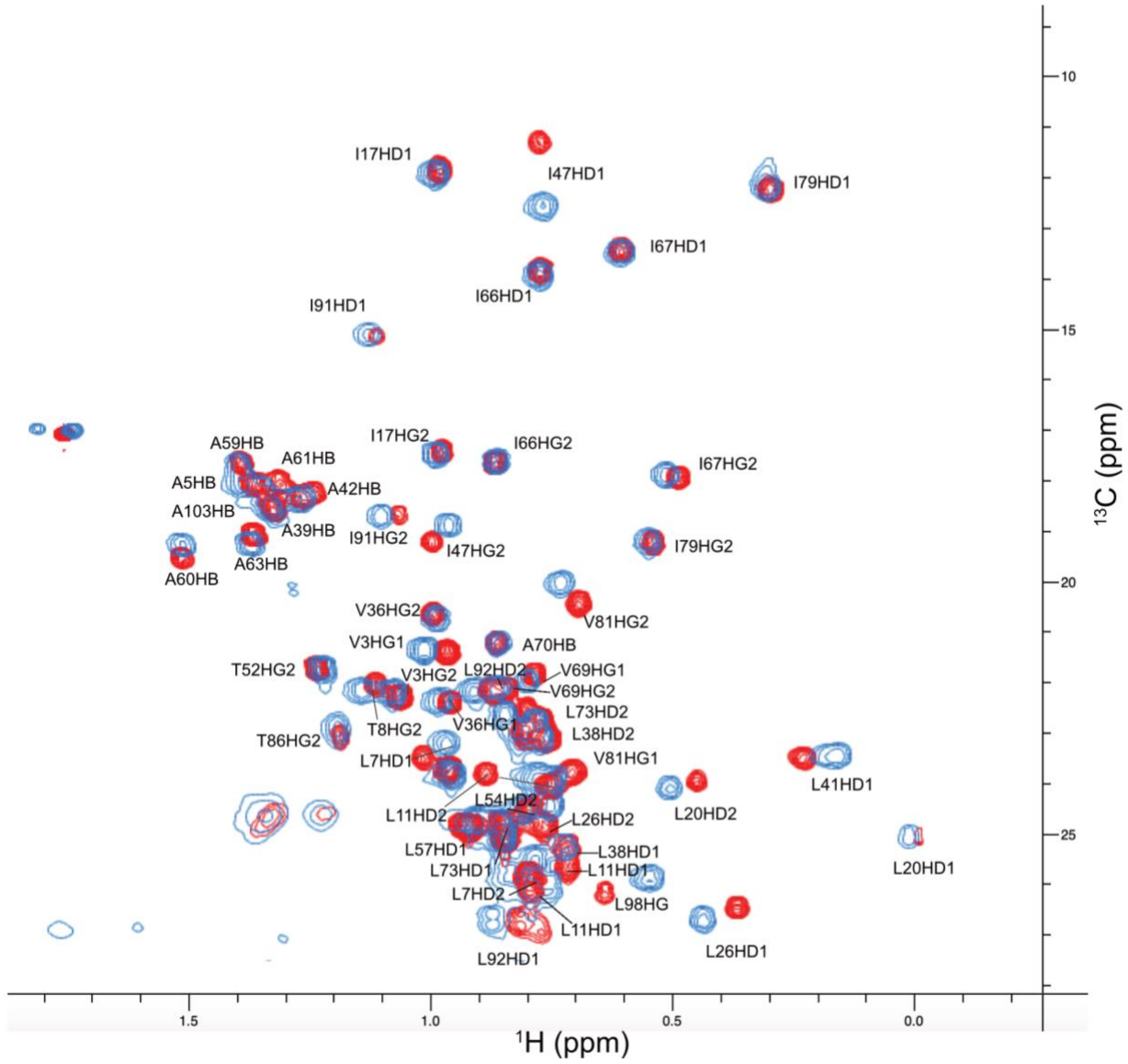

Figure 27. ^{13}C-HSQC spectra of Slr1p in the free (red) form and the bound (blue) form to RNA15. The experiment was carried out at 298 K. Afterwards, the spectral data was processed and displayed using CcpNMR.

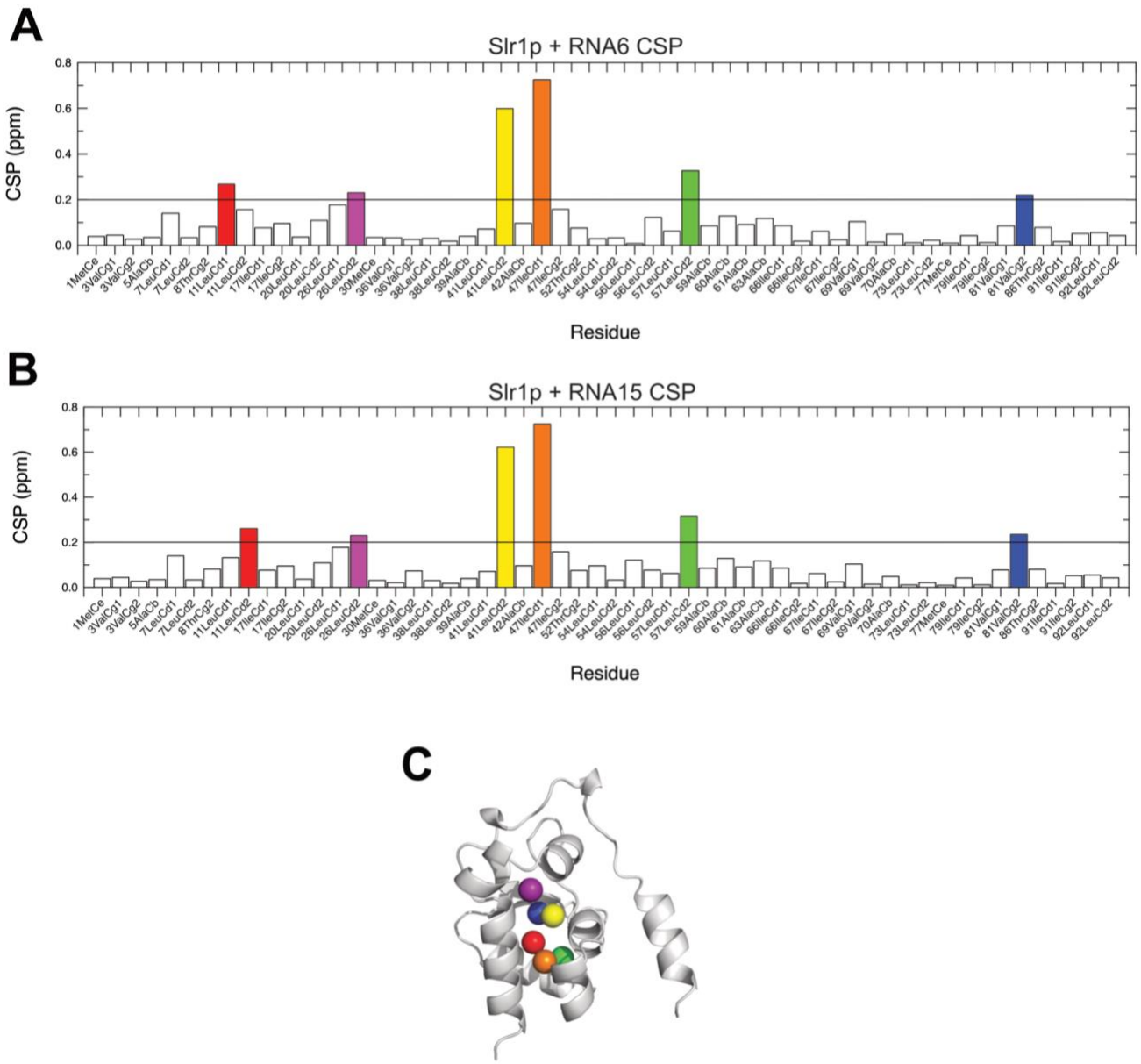

Figure 28. CSP of methyl carbons of Slr1p when titrated with RNA15 and RNA6. CSP (ppm) of all observed methyl carbon resonances (significant CSP are coloured, methyl carbons exhibiting significant CSP values are 0.2 ppm or greater). **(A)** Slr1p + RNA6 and **(B)** Slr1p + RNA15 CSP graphs with significant methyl residues mapped to **(C)** AlphaFold predicted structure of Slr1p with methyl carbons resonances that have significant CSP coloured.

4.6.2 Slf1p titration with RNA6 reveals residues participating in binding

A 1:1 molar ratio titration of RNA6 with Slf1p was performed just as was done to Slr1p previously, and identical NMR spectra was acquired. Due to line broadening, several amide resonances could not be accurately identified. Visual inspection and analysis of the ^{15}N-HSQC spectrum reveals a series of amide resonances exhibiting significant CSPs. These residues include: S16, E18, N19, L20, K21, T22, E24, I38, A63, L69, F102, I103 R105 (Figures 29 & 30).

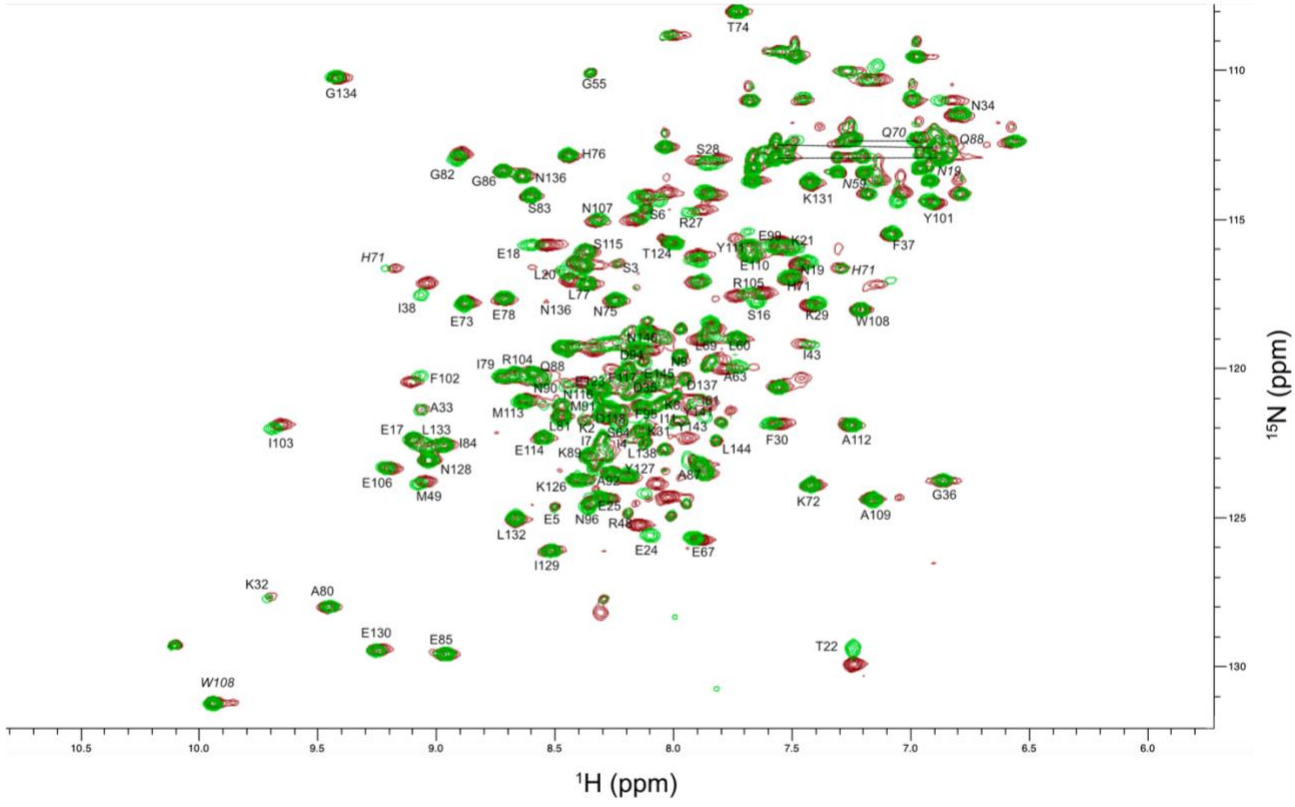

Figure 29. ^{15}N-HSQC of Slf1p with amino acid residues labelled (brown = unbound, green = bound to RNA6 at 1:1 ratio). The experiment was carried out at 298 K. Afterwards, the spectral data was processed and displayed using CcpNMR.

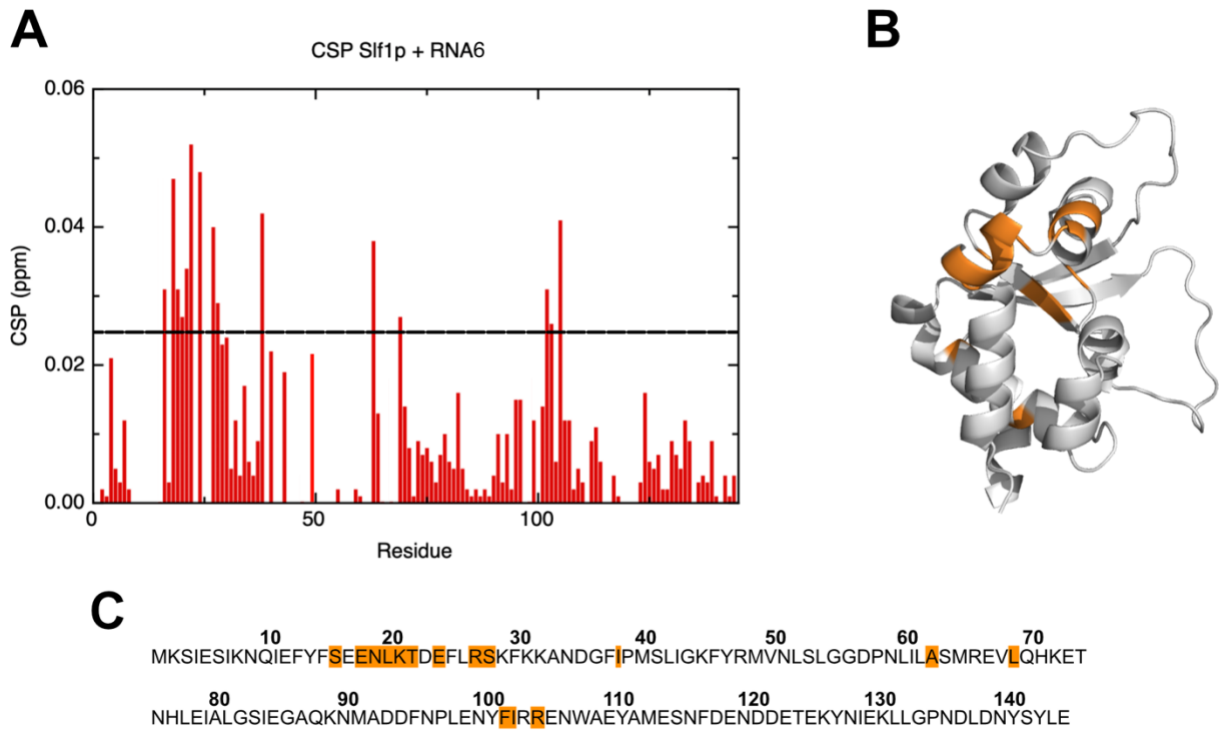

Figure 30. CSP of Slf1p and RNA6, derived from the assigned amide resonance in ^{15}N-HSQC NMR spectra. (A) CSP plot of CSP values corresponding to each amide resonance that was observed and assigned on the NMR spectra. **(B)** Residues with CSP values of 0.025 ppm and greater are highlighted in orange on the predicted AlphaFold structure of Slf1p and **(C)** the Slf1p LaM sequence chain. Residues with significant CSP are highlighted.

Methyl carbon CSP were also observed in Slf1p. Three methyl carbons were measured to have significant CSP (CSP ≥ 0.05 ppm): I38CG2, L81CD1, and A109HB (Figures 31 & 32). Due to the prominent line broadening in several different peaks within the Slf1p 3D NMR spectra, some methyl residues were impossible to identify, just as was seen within the ^{15}N-HSQC. Unidentifiable methyl residues with large chemical shifts were highlighted with blue boxes in the methyl ^{13}C-HSQC. These peaks are likely associated with leucine, alanine and isoleucines (Figure 31).

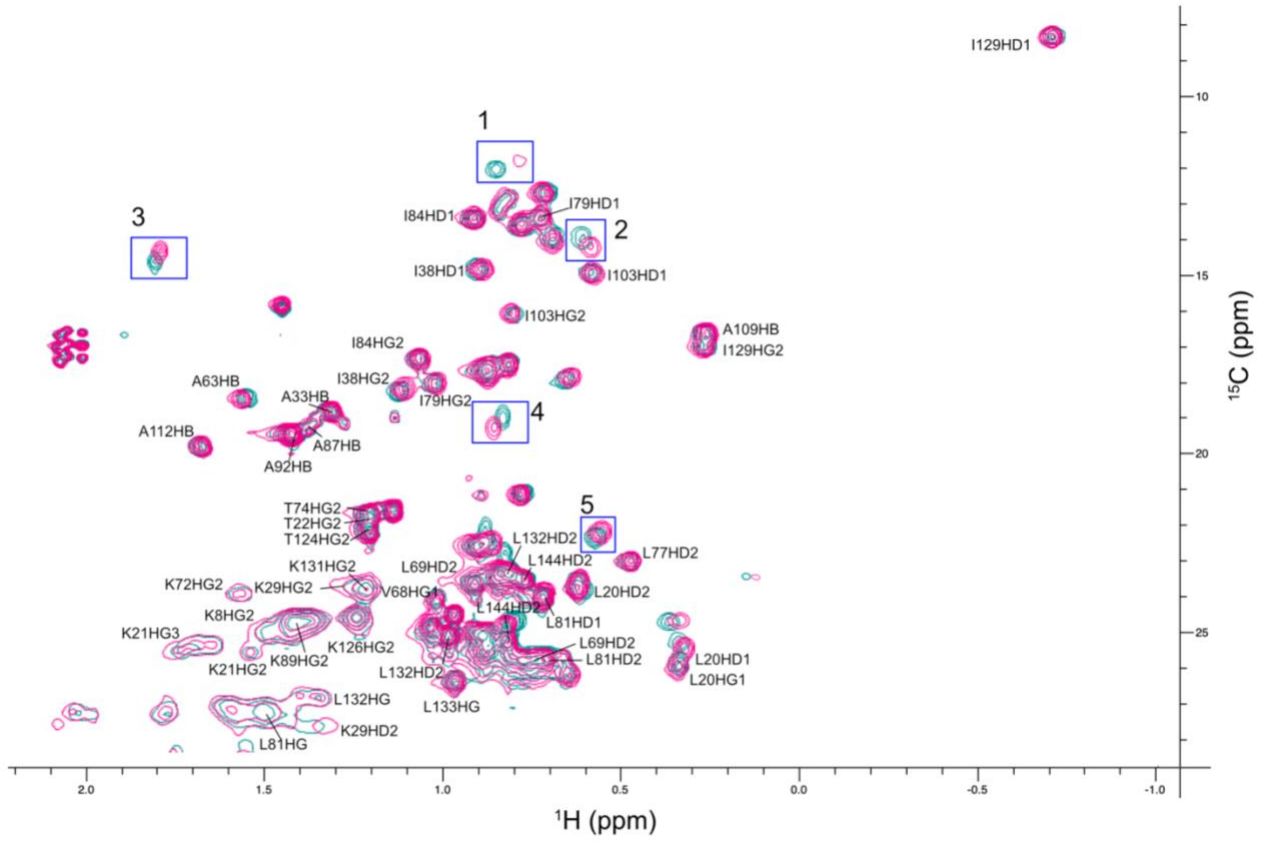

Figure 31. ^{13}C-HSQC spectra of Slf1p in the free (teal) form and the bound (magenta) form to RNA6. The experiment was carried out at 298 K. Afterwards, the spectral data was processed and displayed using CcpNMR. The residues highlighted in blue boxes are peaks that had large chemical shifts but are unidentifiable due to line broadening. Residues 1, 2, and 4 are likely methyls that are associated with isoleucines. Residue 3 is likely the HB of an alanine, and residue 5 is likely associated with a leucine.

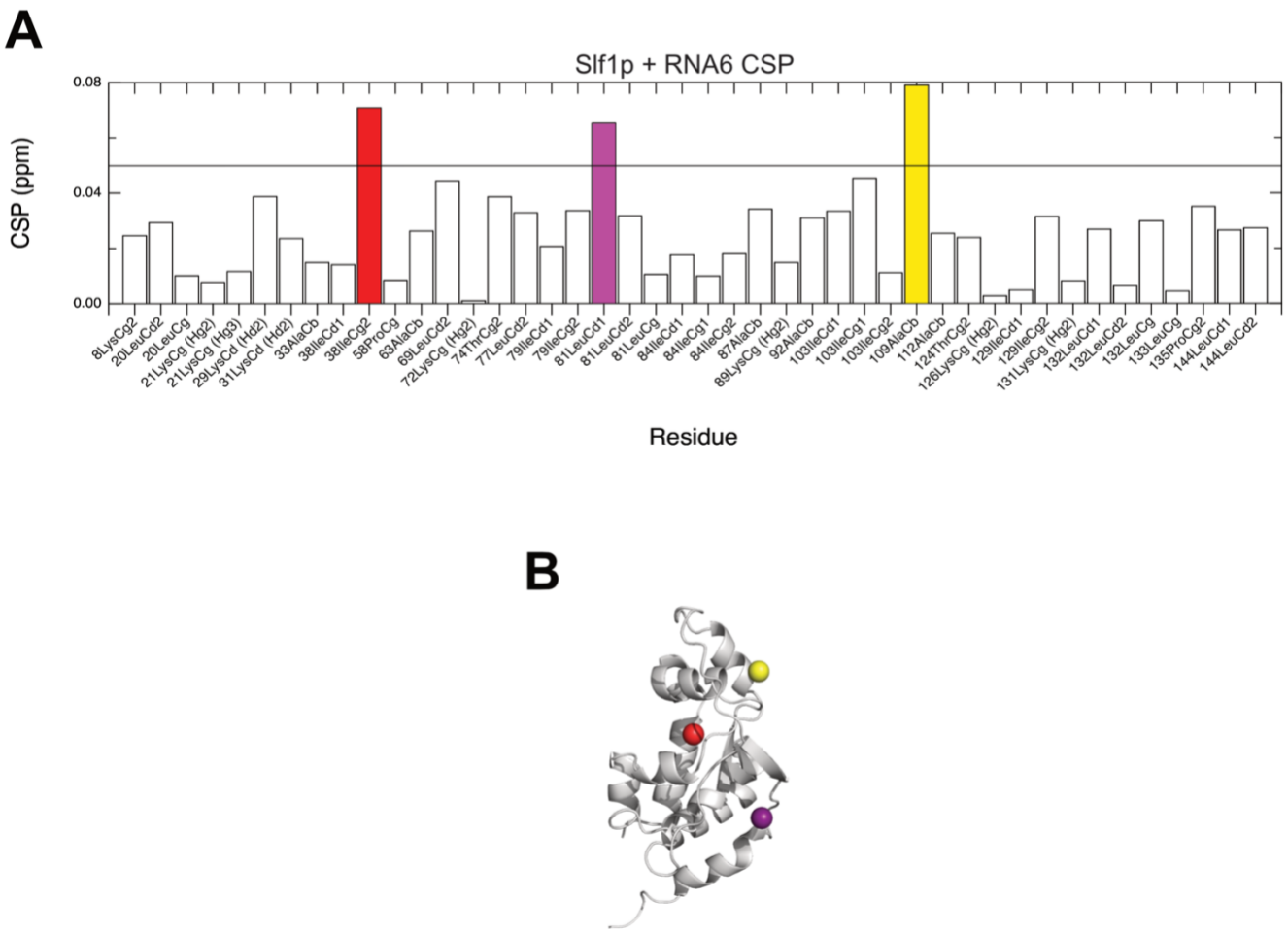

Figure 32. CSP of methyl carbons of Slf1p when titrated with RNA6. CSP (ppm) of all observed methyl carbon resonances (significant CSP are coloured, methyl carbons exhibiting significant CSP values are 0.05 ppm or greater). **(A)** Slf1p + RNA6, methyl carbons exhibiting **(B)** AlphaFold predicted structure of Slf1p, with atoms exhibiting significant CSP being coloured.

4.7 Conformational Exchange Observed Near Binding Site

The ^{13}C edited 3D NOESY spectra of Ile17 HA reveal distinct RNA-binding effects. In the unbound state, strong NOEs are observed between Ile17 HA and nearby protons. Upon binding RNA15, the Ile17 amide resonance is retained, but the Ser21 amide disappears (Figure 33). However, in the RNA6-bound form, both the Ile17 and Ser21 amide resonances are absent and show a new leucine amide proton resonance (Leu20 H). The cause of these differing observations indicates that, despite similar overall binding and CSPs, RNA15 and RNA6 could induce unique local structural or dynamic adjustments around Ile17. Given that Ile17 is flanked by residues showing significant CSPs and is located near the RNA-binding interface, the absence of the Ile17 amide resonance in the RNA15-bound spectrum likely indicates conformational changes, as alpha carbons are particularly susceptible to backbone rearrangements. Notably, the new leucine resonance in RNA6 binding suggests a specific, unique local interaction.

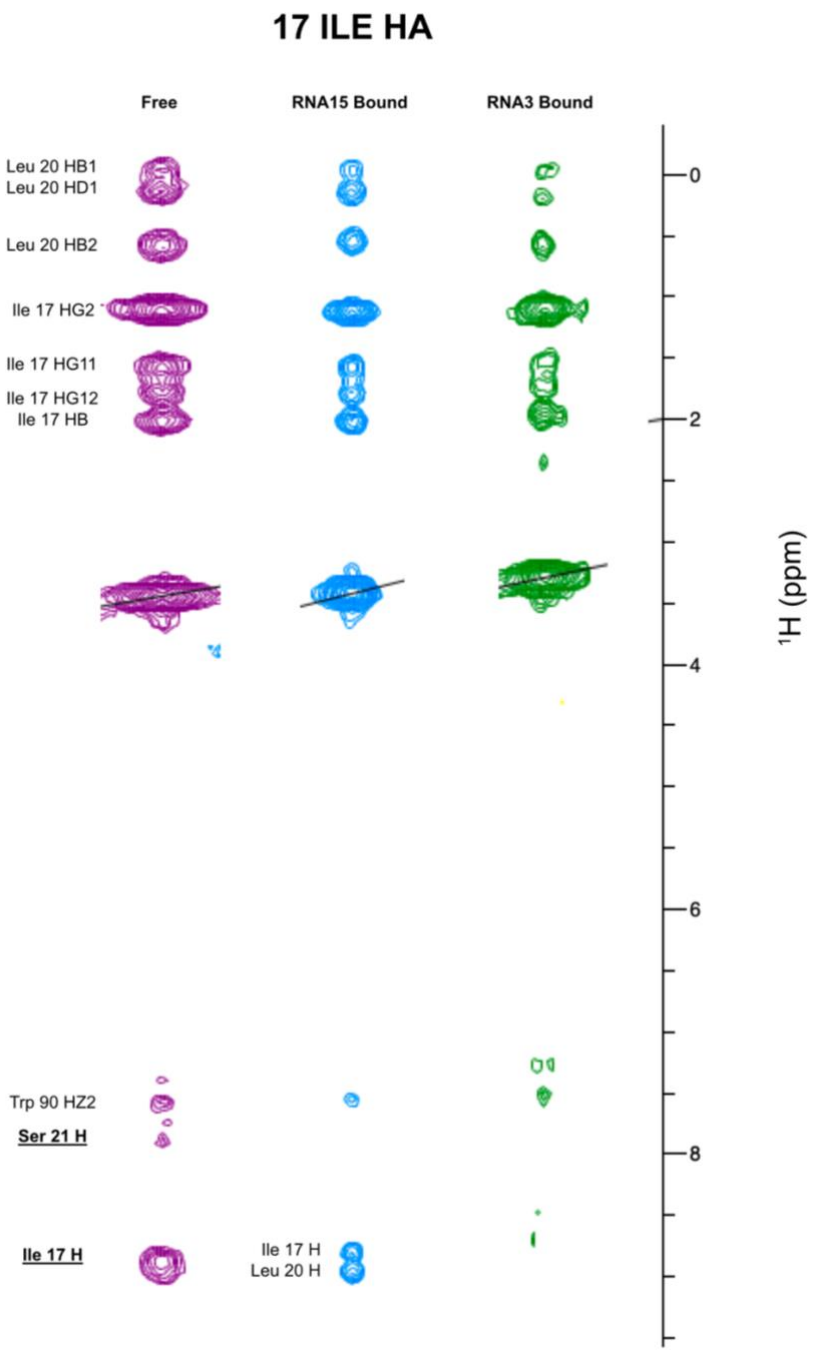

Figure 33. ^{13}C edited 3D NOESY strips centred on Ile17 HA in the free, RNA15-bound, and RNA6-bound protein states. The Ile17 amide resonance is present in the free and RNA15-bound forms but absent in RNA6-bound. The Ser21 amide peak disappears in both bound forms, indicating local structural or dynamic changes near Ile17 upon RNA binding. Peaks with labels that are bolded and underlined represent those peaks disappearing or changing between the free and bound forms. The two amide resonances within the RNA15 bound form are appropriately labeled.

4.8 Slr1p participates in the binding of a known stress-signalling molecule

Ap4a serves as a signalling molecule in various cellular processes, including cell growth, differentiation, and responses to stress. In yeast, this class of molecules can accumulate up to 4 µM when exposed to heavy metals or heat stress (Baltzinger et al., 1986). To investigate the potential binding of Ap4a on Slr1p, an ITC experiment was used to determine if binding occurs. Using 100 µM of Slr1p protein and 1.56 mM of Ap4a (both ligand and titrant were suspended in PBS, 10 mM sodium phosphate pH 7.4, 60 mM NaCl), and ITC thermogram reveals that the K_d is 754 ± 168 µM, suggesting binding is present but is weak (Figure 34).

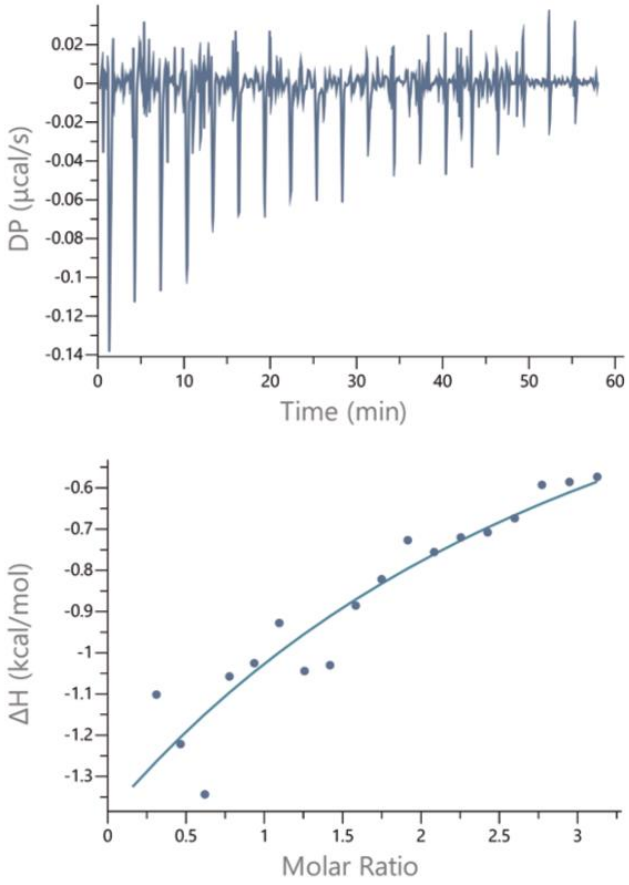

Figure 34. Isothermal titration calorimetry of Slr1p with Ap4a. Isotherm of Slr1p with Ap4a. Ap4a solutions were at a concentration of 1.56 mM while the Slr1p sample was 100 µM. This isothermal titration calorimetry experiment was conducted by fellow researcher Emily Hoi Pui Chao from the Johnson Lab, using the purified and concentrated protein sample that I prepared.

4.9 Slr1p, Slf1p, and Sro9p show similar affinity and thermodynamics when binding to RNA15 and RNA6

To investigate the thermodynamics, enthalpy, and kinetics of the RNA and protein interactions, a series of titrations was performed involving Slr1p, Slf1p and Sro9p with RNA15, RNA6 and 6A (Figure 35). The buffer used for the ligand and proteins was PBS buffer, consisting of 150 mM NaP and 20 mM NaCl to maintain the stability of the protein for storage and during the duration of the experiment. ITC analysis shows that the difference in binding between the proteins is not significant in value. The RNA15, RNA6 and 6A ligands show relatively similar binding, within the low micromolar K_d range. Slf1p shows the best binding to all ligands when compared to the other two proteins. Slf1p + RNA15 shows the best binding while Slr1p + RNA6 shows the weakest (Table 15). RNA15 shows the greatest discrimination of binding affinities between the proteins, varying up to 475% between Slf1p + RNA15 and Slr1p + RNA15. All data points for all isotherms are close to the curve fit. ΔH, ΔG and $-T\Delta S$ are all negative, indicating that the binding event between the proteins of study and the ligands is exothermic, spontaneous, and disordered. Among all the titrations, the binding between Sro9p + RNA6 was the most exothermic, with a ΔH of -22.5 ± 2.0 kcal/mol, showing a strong enthalpic contribution to the interaction (Table 16). The negative ΔG values confirm the thermodynamic favourability of the binding process, while the positive $-T\Delta S$ values suggest an increase suggests increased order upon complex formation.

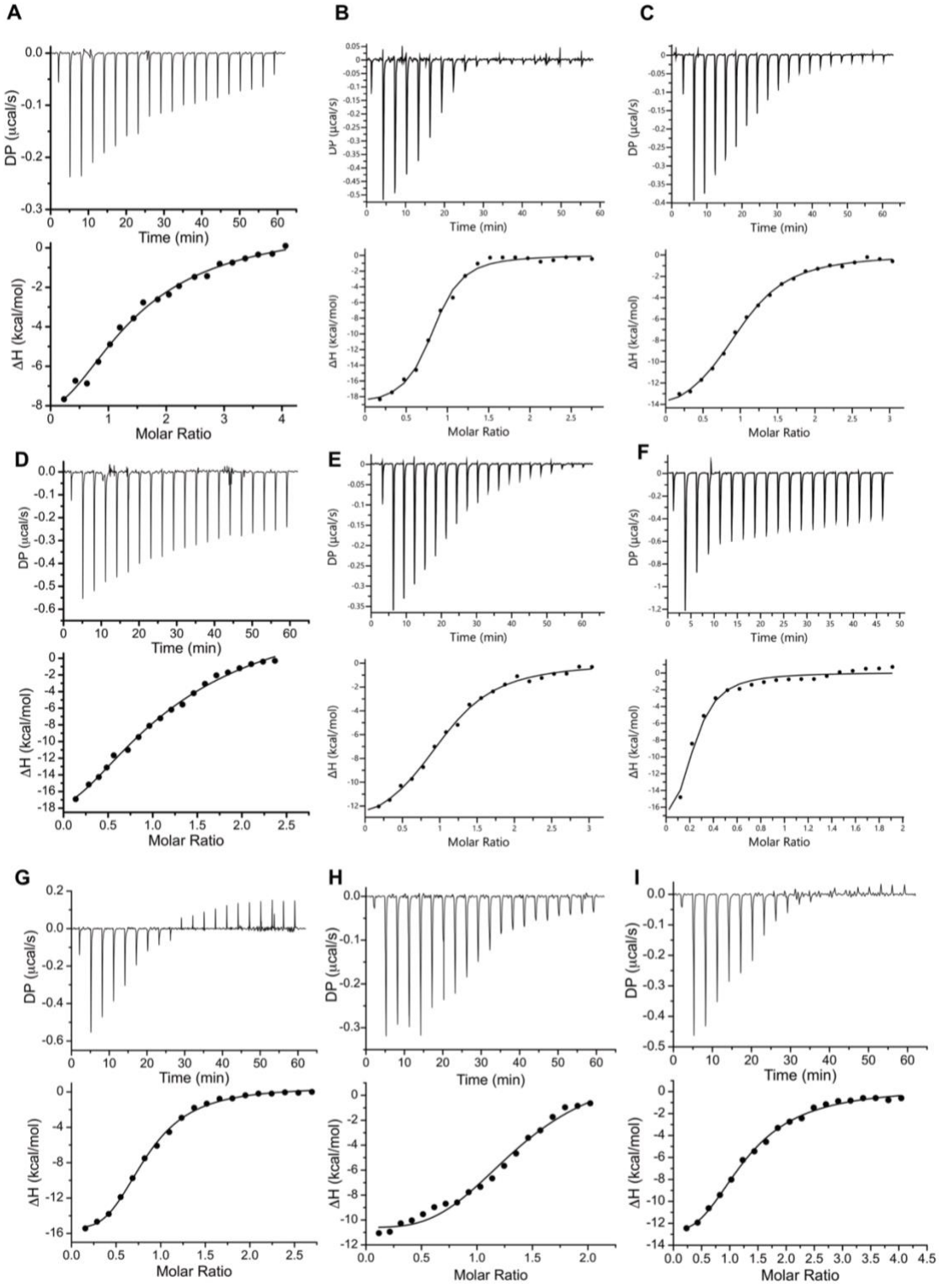

Figure 35. Thermograms and their respective isotherms of Slr1p, Slf1p and Sro9p obtained from ITC. (A) Thermogram and isotherm from Slr1p + RNA15 binding event. **(B)** Thermogram and isotherm from the Slf1p + RNA15 binding event. **(C)** Thermogram and isotherm from Sro9p

+ RNA15 binding event. **(D)** Thermogram and isotherm from Slr1p + RNA6 binding event. **(E)** Thermogram and isotherm from the Slf1p + RNA6 binding event. **(F)** Thermogram and isotherm from Sro9p + RNA6 binding event. **(G)** Thermogram and isotherm of Slr1p + 6A binding interaction. **(H)** Thermogram and isotherm of Slf1p + 6A binding interaction. **(I)** Thermogram and isotherm of Sro9p + 6A binding interaction.

Table 15. Individual K_d values of Slr1p, Sro9p, and Slf1p with RNA6, RNA15 and 6A were calculated with ITC (values rounded to the nearest tenth).

	Slr1p	**Sro9p**	**Slf1p**
RNA6	2.9 ± 0.3 μM	2.2 ± 0.6 μM	1.7 ± 0.3 μM
RNA15	2.3 ± 0.3 μM	1.4 ± 0.2 μM	0.4 ± 0.1 μM
6A	1.3 ± 0.2 μM	2.6 ± 0.7 μM	1.1 ± 0.3 μM

Table 16. Thermodynamic and enthalpy values from ITC binding experiments (values rounded to the nearest tenth).

	ΔH (kcal/mol)	**ΔG (kcal/mol)**	**−TΔS (kcal/mol)**
Slr1p + RNA15	-13.0 ± 1.4	-7.7	5.3
Slr1p + RNA6	-17.4 ± 1.2	-7.6	9.8
Slr1p + 6A	-17.8 ± 0.8	-8.0	9.8
Slr1p + Ap4a	-11.6 ± 1.9	-4.2	7.4
Slf1p + RNA15	-19.4 ± 0.7	-8.7	10.7
Slf1p + RNA6	-14.4 ± 0.7	-7.9	6.5
Slf1p + 6A	-14.2 ± 1.2	-8.1	6.0
Sro9p + RNA15	-15.7 ± 0.5	-8.0	7.7
Sro9p + RNA6	-22.5 ± 2.0	-7.7	14.8
Sro9p + 6A	-15.6 ± 1.5	-7.6	8.0

5. DISCUSSION

5.1 Structural and Functional Relationship Between Slr1p, Sro9p and Slf1p

The detailed structural analyses of Slr1p, Slf1p, and Sro9p presented in this thesis offer valuable insights into the evolutionary relationships and functional diversification within the LARP protein family. The high degree of structural similarity between Slf1p and Sro9p (RMSD 1.2 Å) supports their proposed paralogous relationship, as recently confirmed by Jennings et al. (2023), who identified shared evolutionary origins linking LARP1 and LARP4 proteins. The observed structural differences between these two paralogs and Slr1p, particularly the absence of a loop in the winged helix region and a missing beta-strand in Slr1p, suggest functional divergence that may have occurred following gene duplication events. These paralogs are phylogenetically and evolutionarily connected to Slr1p as they are all LARP1 yeast proteins.

The beta-sheet network analysis presented in this thesis provides novel structural insights that may produce some structural understanding of recent findings. NMR spectroscopy and the structural model predicted by AlphaFold confirmed the presence of an extra beta-sheet in Slf1p. The relevance of this structural aspect may relate to the capacity of Slf1p to maintain the correct reading frame of ribosomes during stress conditions, as recently pointed out by Jennings et al. (2023). The structural evidence provided in this work presents a tangible basis from which to understand how those proteins could interact with ribosomes and RNA targets.

5.2 RNA-binding Properties and Mechanisms

The RNA-binding characteristics of Slr1p, Slf1p, and Sro9p described in this thesis display remarkable consistency in their affinity for various RNA targets with similar K_d values

across the three proteins. Thermodynamic analysis of the protein-oligonucleotide interactions reveals striking parallels with hLARP1 RNA binding characteristics reported by Kozlov et al. (2022, 2024), supporting evolutionary conservation in protein-RNA complex formation. In contrast, Kozlov et al. 2022 and Kozlov et al. 2024 reported that hLARP1 LaM binds to poly(A) RNAs with significantly tighter affinities in the low micromolar to nanomolar range, particularly when poly(A) tails contain internal uridine, cytosine, or guanine substitutions (K_d ranging from 0.070 μM – 0.297 μM). Comparative analysis of A6 binding demonstrates striking consistency with Kozlov et al.'s (2022, 2024) poly(A) recognition studies. The ITC titration experiments reported K_d ranging between 1.1 ± 0.3 μM and 2.6 ± 0.7 μM (across the three proteins experimented) while Kozlov et al. 2022 & 2024 showed K_d of 0.24 ± 0.024 μM and 0.250 ± 0.015 μM, respectively. The consistently higher affinity could result from either the evolutionary refinement of the LaM domain in hLARP1 or from the experimental parameters, such as temperature and concentration of the ITC binding experiment.

The CSP data identifying specific RNA-binding residues offers valuable insight into the relationship between protein structure and binding interactions. The observation that many of the same residues in Slr1p are involved in binding both RNA6 and RNA15 suggests a conserved binding interface. The only residue that was not shared as a significant CSP between the two titrations was the amide of L11. Titration of Slr1p with RNA6 and RNA15 induced substantial chemical shift perturbations, predominantly affecting residues in the β-sheet network and neighbouring loops. This aligns with recent findings by Vinayak et al. (2018) that human La (hLa) interacts with poly(A) RNA through a conserved winged-helix face of the La motif. This work provides evidence for the evolutionary conservation of the recognition mechanism among LARP family proteins.

The conformational exchange observed near the binding site, particularly the disappearance of certain NOEs in the bound conformation as seen with Ile17 in Slf1p, indicates dynamic structural changes upon RNA-binding. The conformational flexibility observed in this thesis may facilitate these complex protein-RNA-ribosome interactions during regular and stress-induced binding conditions.

5.3 Protein-Binding Conformations and Dynamics

The NMR and DSC analyses in this thesis highlight how protein conformations and their inherent plasticity are central to LARP1's capacity to recognize RNA and regulate its function. The findings on CSP, line broadening, and variations in protein flexibility and structure are relevant to high-resolution studies of LARP1 and other related LARP families.

Dynamic conformational changes are a hallmark of LARP1-RNA interactions. The NMR spectroscopy data of the RNA6 titration with Slf1p, where intermediate-to-slow exchange kinetics produced line broadening of binding-associated resonances, align with recent findings by Cassidy et al. (2019). Their work demonstrated that the α7-α8 bridge in hLARP1 toggles between open and closed states, regulating access to the m7G cap and thereby controlling ribosome biogenesis in response to cellular demands. These parallels suggest that conformational switching is a conserved regulatory strategy in both yeast and human LARP1 systems.

The conformational exchange of Slf1p upon binding to RNA6, as observed with NMR spectroscopy, along with the TALOS+ predicted dynamic residues of Slf1p, echoes how intrinsically disordered regions (IDRs) may influence binding within LARP1 through structural rearrangement. Kozlov et al. (2022) revealed that flexible loops and adjacent linkers in LARP1

retain conformational dynamics, facilitating RNA recognition even in the absence of an RRM1 domain. Complementing these findings, Mattijssen et al. (2020) observed that the strong specificity and structural adaptability of 3′-end binding imply the presence of a highly dynamic interaction surface. Collectively, these studies underscore how LARP1 proteins exploit both ordered and disordered structural features to achieve functional versatility.

The DSC data presented in this thesis suggest a stabilization mechanism, as the binding of 6A to Slf1p, Slr1p, and Sro9p resulted in elevated melting points and increased enthalpy. Saba et al. (2024) reinforces the notion that RNA-induced stabilization is a conserved feature of LARP1. In their study, they demonstrated the functional importance of dynamic regions utilizing cryo-electron microscopy (cryo-EM) studies of hLARP1 bound to a ribosome. Their findings revealed that flexible ribosome-binding elements became ordered upon their association with the 40S ribosome, suggesting a similar stabilization mechanism that was seen within the DSC data. This evidence confirms the view that RNA-binding induced stabilization is a shared functional property within the LARP1 lineage.

Together, these findings support a model where LARP1 proteins may utilize dynamic and structural flexibility to bind diverse RNAs and regulate translation.

5.4 Role in Cellular Stress Response

The thesis finding on the weak but observable binding of Slr1p to Ap4a provides a possible molecular link between LARP proteins and cellular stress response mechanisms. This result is particularly relevant in the context of recent research by Jennings et al. (2023), which demonstrated that Slf1p plays an essential role in maintaining the correct reading frame of ribosomes during oxidative stress. The detectable binding of Ap4a to Slr1p (K_d of 754 μM)

suggests that this interaction may be part of a stress-sensing system that helps cells adapt to unfavourable conditions. Notably, Ap4a accumulates to around 4 μM in yeast cells under heat stress, a 50-fold increase from its basal levels (Brevet et al., 1987; Ferguson et al., 2020). While in human cells, Ap4A levels in human cells reach up to ~25 μM (also a 50-fold increase) in response to oxidative-like DNA damage (Marriot et al., 2015). This disparity suggests yeast LARPs may have evolved to conserve a similar stress response (both show a similar increase in Ap4a), but mammalian cells need higher amounts of the alarmone. This difference may reflect biological distinctions, such as the greater cellular volume and signalling complexity of mammalian systems. Ap4A levels have also been shown to differ between other cell types, as evidenced by their stability in proliferating thyroid cells (Perret et al., 1990) in contrast to their apoptosis-inducing role in HL60 cells (Vartanian et al., 1999). The findings on the association between Ap4a and Slr1p also complement recent research on LARP1's role in endoplasmic reticulum (ER) stress in humans. Yang et al. (2024) revealed that human LARP1 is upregulated in esophageal squamous cell carcinoma cells upon ER stress through the ERN1-XBP1 pathway. This variability in Ap4A concentrations across systems, combined with its compartment-specific roles in stress response and apoptosis, highlights the context-dependent nature of Ap4A signaling and its evolutionary adaptation to cellular needs.

The yeast LARP proteins examined in this thesis, therefore, may represent evolutionary precursors to the more intricate stress response systems found in humans. The observed interaction between Ap4a and Slr1p in yeast provides a tangible example of how these conserved mechanisms might operate at a molecular level, offering valuable insights into the fundamental principles governing cellular resilience across diverse biological systems.

Recent observations by Röther et al. (2010) and Jennings et al. (2023) have established that Sro9p specifically plays a role in stress granule formation, while Slf1p helps in the regulation of ribosome frameshifting during stress. The thermostability data presented in this thesis, showing that Sro9p has the lowest melting point (36.2°C), followed by Slf1p (46.5°C) and Slr1p (53.1°C), may provide a physical explanation for these functional differences. This thermostability pattern is the same when these proteins are bound to 6A. Binding to 6A increases the thermostability of the proteins, confirming LARP1's stabilizing effect upon RNA interaction. This enhanced stability likely helps the proteins resist denaturation under stress conditions, enabling them to maintain their functional roles when other cellular components may be compromised. Recent findings from Hou et al. (2024) show that there is a negative correlation between millisecond dynamics and thermal stability, suggesting the thermal stability of Sro9p may allow it to undergo structural reorganization during stress conditions, potentially contributing to its role in stress granule assembly. Furthermore, results from Kershaw et al. (2015) reveal that yeast cells lacking Sro9p or Slf1p show little to no sensitivity to growth when exposed to different temperature levels and at high salt concentrations. These findings suggest that it is likely that the different thermostability profile of Sro9p may not be related to its function with heat shock or temperature-related cellular functions.

5.5 Methodological Considerations and Limitations

While this thesis provides valuable insights into the structure and function of LARP proteins, several methodological limitations should be acknowledged. The in vitro nature of the experiments, while allowing for precise molecular characterization of structure and binding, may not fully capture the complexity of LARP protein functions in the cellular environment.

Interactions with other cellular components, post-translational modifications, and compartmentalization might all influence LARP protein behaviour in vivo.

The structural analysis of Slf1p was limited by peak broadening in the NMR spectra, which prevented the calculation of a complete structure. This technical challenge highlights the difficulties in studying proteins with dynamic regions or conformational heterogeneity. Future studies can employ complementary techniques such as chemical exchange saturation transfer (CEST) NMR, dark-state exchange saturation transfer (DEST) NMR, or X-ray crystallography to overcome this limitation.

The RNA-binding experiments focused on specific RNA sequences (RNA6 and RNA15), which do not represent the full spectrum of physiological RNA targets. New research by Kozlov et al. (2022) has shown that LARP1 can distinguish a wide range of RNA structures, including 3'-poly(A) tails and specific stem-loops. Additionally, Jennings et al. (2023) employed photoactivatable ribonucleoside-enhanced crosslinking and immunoprecipitation (PAR-CLIP) to identify transcriptome-wide mRNA targets of Slf1p and Sro9p in *S. cerevisiae*. Their findings revealed preferential binding within coding sequences, especially of mRNAs related to translation and stress responses. Building on this, structural and binding studies (NMR, ITC) using diverse, physiologically relevant RNA ligands identified in previous research would offer a more nuanced insight into RNA-binding preferences and contribute to a more complete understanding of LARP protein function.

Despite these limitations, the multi-technique approach employed in this thesis by combining computational predictions using AlphaFold, NMR spectroscopy, DSC, and binding assays provides a strong foundation for understanding the structure-function relationships of

these proteins. Each method compensates for limitations in others, resulting in a comprehensive characterization that advances the understanding of LARP protein biology while acknowledging the boundaries of current methodological approaches.

5.6 Considerations for Future Research

Based on the findings presented in this thesis and recent advances in the field, several promising directions for future research can be identified. First, the structural and functional relationships between yeast LARP proteins and their human counterparts (e.g. hLARP1) should be further explored. Comparative studies could provide insight into the evolution of LARP protein functions and the identification of conserved mechanisms that can be targeted therapeutically.

Another critical area of future research includes the interaction of LARP proteins with the translational machinery, particularly under conditions of cellular stress. This can build off the previously mentioned findings that show Slf1p interaction with colliding ribosomes to maintain translation of stress-regulated mRNAs. Following the results of that study and the one described in this thesis, future studies could explore how the structural features can contribute to these interactions and how they might be regulated for therapeutic purposes.

The findings of this thesis provide a framework for exploring how the intrinsically disordered segments of yeast LARP proteins, such as Slf1p and Sro9p, contribute to their functional roles in stress responses. Future studies could focus on identifying specific protein–protein interaction partners of these intrinsically disordered regions and elucidating how such interactions are modulated under stress conditions. These insights may, in turn, inform a broader

understanding of how LARP family proteins function in higher eukaryotes, where similar disordered regions have been implicated in regulating flexibility and adapting to cellular stress.

5.7 Contributions

To clarify the scope of my contribution to this project, I was involved in all aspects of protein expression, protein purification, protein quantification, preparation for structural and binding experiments, and statistical analysis. Dr. Donaldson initialized all NMR experiments with the TopSpin software. I did all NMR residue assignments utilizing CcpNMR to display spectra and make assignments while using NMRtist for assistance to help expedite residue identification. All differential scanning calorimetry and isothermal titration calorimetry experiments and their results were carried out and collected externally by fellow researchers: Dr. Shoara and Emily Hoi Pui Chao. All figures were created by me, except Figures 21, 34, and 35, which are data and results shared with me by Dr. Shoara or Emily Hoi Pui Chao and compiled and incorporated within this thesis. All RNA sequencing was done by external companies like GenScript, Bio-synthesis, and Horizon Biosciences.

5.8 Conclusion

Overall, this thesis provides valuable structural and functional insights into the yeast LARP1 protein family, focusing on Slr1p, Slf1p, and Sro9p from *Schizosaccharomyces pombe* and *Saccharomyces cerevisiae*, respectively. The findings shed light on how these proteins interact with RNA, respond to cellular stress, and potentially modulate various physiological and pathological processes. By integrating recent findings on higher eukaryotic LARP proteins with yeast studies from this thesis, it was shown that conserved structural frameworks have been functionally diversified across evolution while maintaining core RNA recognition principles.

The structural analysis of these proteins, particularly the identification of specific residues involved in RNA-binding and the testing of thermostability, provides a foundation for understanding their molecular functions. The observation of the potential association between Slr1p and Ap4a establishes a possible link between LARP proteins and cellular stress response mechanisms, which may have implications for various stress-related pathologies.

Future research building on these findings could enhance understanding of how LARP proteins function under stress by further characterizing their structural dynamics and interactions, particularly those mediated by intrinsically disordered regions. Investigating how these regions contribute to protein–protein and protein–RNA interactions in yeast may offer insights into the general principles of LARP protein function that are conserved across eukaryotes. Such work could eventually inform broader models of RNA-binding protein regulation in stress adaptation, laying a foundation for studies in more complex systems.

REFERENCES

Alfano, C., Sanfelice, D., Babon, J., Kelly, G., Jacks, A., Curry, S., & Conte, M. R. (2004). Structural analysis of cooperative RNA binding by the la motif and central RRM domain of human La protein. *Nature Structural & Molecular Biology*, *11*(4), 323–329. https://doi.org/10.1038/nsmb747

Baltzinger, M., Ebel, J.-P., & Remy, P. (1986). Accumulation of dinucleoside polyphosphates in saccharomyces cerevisiae under stress conditions. high levels are associated with cell death. *Biochimie*, *68*(10–11), 1231–1236. https://doi.org/10.1016/s0300-9084(86)80069-4

Berman, A. J., Thoreen, C. C., Dedeic, Z., Chettle, J., Roux, P. P., & Blagden, S. P. (2020). Controversies around the function of LARP1. *RNA Biology*, *18*(2), 207–217. https://doi.org/10.1080/15476286.2020.1733787

Blagden, S. P., Gatt, M. K., Archambault, V., Lada, K., Ichihara, K., Lilley, K. S., Inoue, Y. H., & Glover, D. M. (2009). Drosophila LARP associates with poly(a)-binding protein and is required for male fertility and syncytial embryo development. *Developmental Biology*, *334*(1), 186–197. https://doi.org/10.1016/j.ydbio.2009.07.016

Bousquet-Antonelli, C., & Deragon, J.-M. (2009). A comprehensive analysis of the LA-motif protein superfamily. *RNA*, *15*(5), 750–764. https://doi.org/10.1261/rna.1478709

Bray, F., Laversanne, M., Sung, H., Ferlay, J., Siegel, R. L., Soerjomataram, I., & Jemal, A. (2024). Global cancer statistics 2022: Globocan estimates of incidence and mortality worldwide for 36 cancers in 185 countries. *CA: A Cancer Journal for Clinicians*, *74*(3), 229–263. https://doi.org/10.3322/caac.21834

Brevet, A., Coste, H., Fromant, M., Plateau, P., & Blanquet, S. (1987). Yeast diadenosine 5',5'''-P1,P4-tetraphosphate .alpha.,.beta.-phosphorylase behaves as a dinucleoside tetraphosphate synthetase. *Biochemistry*, *26*(15), 4763–4768. https://doi.org/10.1021/bi00389a025

Cassidy, K. C., Lahr, R. M., Kaminsky, J. C., Mack, S., Fonseca, B. D., Das, S. R., Berman, A. J., & Durrant, J. D. (2019). Capturing the mechanism underlying top mrna binding to LARP1. *Structure*, *27*(12). https://doi.org/10.1016/j.str.2019.10.006

Cavanagh, J., Fairbrother, W. J., Palmer, I. A. G., Skelton, N. J., & Rance, M. (2010). *Protein NMR spectroscopy: Principles and practice*. Elsevier Science.

Chauvet, S., Merabet, S., Bilder, D., Scott, M. P., Pradel, J., & Graba, Y. (2000). Distinct Hox protein sequences determine specificity in different tissues. *Proceedings of the National Academy of Sciences*, *97*(8), 4064–4069. https://doi.org/10.1073/pnas.070046997

Cruz-Gallardo, I., Martino, L., Kelly, G., Atkinson, R. A., Trotta, R., De Tito, S., Coleman, P., Ahdash, Z., Gu, Y., Bui, T. T., & Conte, M. R. (2019). LARP4A recognizes Polya RNA

via a novel binding mechanism mediated by disordered regions and involving the PAM2W motif, revealing interplay between PABP, LARP4A and mrna. *Nucleic Acids Research*, *47*(8), 4272–4291. https://doi.org/10.1093/nar/gkz144

De Gaudenzi, J., Frasch, A. C., & Clayton, C. (2005). RNA-binding domain proteins in kinetoplastids: A comparative analysis. *Eukaryotic Cell*, *4*(12), 2106–2114. https://doi.org/10.1128/ec.4.12.2106-2114.2005

Frishman D, Argos P. (1995). Knowledge-Based Protein Secondary Structure Assignment Proteins: Structure, Function, and Genetics 23:566-579

Ferguson, F., McLennan, A. G., Urbaniak, M. D., Jones, N. J., & Copeland, N. A. (2020). Re-evaluation of diadenosine tetraphosphate (ap4a) from a stress metabolite to bona fide secondary messenger. *Frontiers in Molecular Biosciences*, *7*. https://doi.org/10.3389/fmolb.2020.606807

Fonseca, B. D., Zakaria, C., Jia, J.-J., Graber, T. E., Svitkin, Y., Tahmasebi, S., Healy, D., Hoang, H.-D., Jensen, J. M., Diao, I. T., Lussier, A., Dajadian, C., Padmanabhan, N., Wang, W., Matta-Camacho, E., Hearnden, J., Smith, E. M., Tsukumo, Y., Yanagiya, A., … Damgaard, C. K. (2015). La-related protein 1 (LARP1) represses terminal oligopyrimidine (top) mrna translation downstream of mTOR complex 1 (mtorc1). *Journal of Biological Chemistry*, *290*(26), 15996–16020. https://doi.org/10.1074/jbc.m114.621730

He, N., Jahchan, N. S., Hong, E., Li, Q., Bayfield, M. A., Maraia, R. J., Luo, K., & Zhou, Q. (2008). A la-related protein modulates 7SK SNRNP integrity to suppress P-tefb-dependent transcriptional elongation and tumorigenesis. *Molecular Cell*, *29*(5), 588–599. https://doi.org/10.1016/j.molcel.2008.01.003

Hou, X.-N., Song, B., Zhao, C., Chu, W.-T., Ruan, M.-X., Dong, X., Meng, L.-S., Gong, Z., Weng, Y.-X., Zheng, J., Wang, J., & Tang, C. (2024). Connecting protein millisecond conformational dynamics to protein thermal stability. *JACS Au*, *4*(8), 3310–3320. https://doi.org/10.1021/jacsau.4c00649

Iadevaia, V., Caldarola, S., Tino, E., Amaldi, F., & Loreni, F. (2008). All translation elongation factors and the E, F, and H subunits of translation initiation factor 3 are encoded by 5′-terminal oligopyrimidine (top) mrnas. *RNA*, *14*(9), 1730–1736. https://doi.org/10.1261/rna.1037108

Ichihara, K., Shimizu, H., Taguchi, O., Yamaguchi, M., & H. Inoue, Y. (2007). A drosophila orthologue of LARP protein family is required for multiple processes in male meiosis. *Cell Structure and Function*, *32*(2), 89–100. https://doi.org/10.1247/csf.07027

Ighodaro, O. M., & Akinloye, O. A. (2018). First Line defence antioxidants-superoxide dismutase (SOD), catalase (CAT) and glutathione peroxidase (GPX): Their fundamental role in the entire antioxidant defence grid. *Alexandria Journal of Medicine*, *54*(4), 287–293. https://doi.org/10.1016/j.ajme.2017.09.001

Jennings, M. D., Srivastava, P., Kershaw, C. J., Talavera, D., Grant, C. M., & Pavitt, G. D. (2023). Interaction of the LA-related protein SLF1 with colliding ribosomes maintains translation of oxidative-stress responsive mrnas. *Nucleic Acids Research*, *51*(11), 5755–5773. https://doi.org/10.1093/nar/gkad272

Jumper, J., Evans, R., Pritzel, A., Green, T., Figurnov, M., Ronneberger, O., Tunyasuvunakool, K., Bates, R., Žídek, A., Potapenko, A., Bridgland, A., Meyer, C., Kohl, S. A., Ballard, A. J., Cowie, A., Romera-Paredes, B., Nikolov, S., Jain, R., Adler, J., … Hassabis, D. (2021). Highly accurate protein structure prediction with alphafold. *Nature*, *596*(7873), 583–589. https://doi.org/10.1038/s41586-021-03819-2

Kozlov, G., Jiang, J., Rutherford, T., Noronha, A. M., Wilds, C. J., & Gehring, K. (2024). Enhanced binding of guanylated poly(a) RNA by the LAM domain of LARP1. *RNA Biology*, *21*(1), 764–773. https://doi.org/10.1080/15476286.2024.2379121

Kozlov, G., Mattijssen, S., Jiang, J., Nyandwi, S., Sprules, T., Iben, J. R., Coon, S. L., Gaidamakov, S., Noronha, A. M., Wilds, C. J., Maraia, R. J., & Gehring, K. (2022). Structural basis of 3′-end poly(a) RNA recognition by LARP1. *Nucleic Acids Research*, *50*(16), 9534–9547. https://doi.org/10.1093/nar/gkac696

Krishnamurthy, H. K., Pereira, M., Rajavelu, I., Jayaraman, V., Krishna, K., Wang, T., Bei, K., & Rajasekaran, J. J. (2024). Oxidative stress: Fundamentals and advances in quantification techniques. *Frontiers in Chemistry*, *12*. https://doi.org/10.3389/fchem.2024.1470458

Liu, Y., Li, Y., Yin, L., Wang, Y., Sun, Y., Zhou, S., Li, P., & Qin, H. (2018). Reactive Oxygen Species-Mediated Damage and Its Role in Alzheimer's Disease. *Oxidative Medicine and Cellular Longevity*, *2018*, Article ID 5848529. https://doi.org/10.1155/2018/5848529

Lobo, V., Patil, A., Phatak, A., & Chandra, N. (2010). Free radicals, antioxidants and Functional Foods: Impact on human health. *Pharmacognosy Reviews*, *4*(8), 118. https://doi.org/10.4103/0973-7847.70902

Mansouri-Noori, F., Pircher, A., Bilodeau, D., Siniavskaia, L., Grigull, J., Rissland, O. S., & Bayfield, M. A. (2023). The LARP1 homolog slr1p controls the stability and expression of proto-5′top mrnas in fission yeast. *Cell Reports*, *42*(10), 113226. https://doi.org/10.1016/j.celrep.2023.113226

Maraia, R. J., Mattijssen, S., Cruz-Gallardo, I., & Conte, M. R. (2017). The la and related rna-binding proteins (larps): Structures, functions, and evolving perspectives. *WIREs RNA*, *8*(6). https://doi.org/10.1002/wrna.1430

Marriott, A. S., Copeland, N. A., Cunningham, R., Wilkinson, M. C., McLennan, A. G., & Jones, N. J. (2015). Diadenosine 5′, 5‴-P1,P4-tetraphosphate (AP4A) is synthesized in response to DNA damage and inhibits the initiation of DNA replication. *DNA Repair*, *33*, 90–100. https://doi.org/10.1016/j.dnarep.2015.06.008

Martino, L., Pennell, S., Kelly, G., Busi, B., Brown, P., Atkinson, R. A., Salisbury, N. J. H., Ooi, Z.-H., See, K.-W., Smerdon, S. J., Alfano, C., Bui, T. T. T., & Conte, M. R. (2014). Synergic interplay of the la motif, RRM1 and the interdomain linker of LARP6 in the recognition of collagen mrna expands the RNA binding repertoire of the la module. *Nucleic Acids Research*, *43*(1), 645–660. https://doi.org/10.1093/nar/gku1287

Mattijssen, S., Kozlov, G., Gaidamakov, S., Ranjan, A., Fonseca, B. D., Gehring, K., & Maraia, R. J. (2020). The isolated la-module of LARP1 mediates 3' poly(a) protection and mrna stabilization, dependent on its intrinsic pam2 binding to pabpc1. *RNA Biology*, *18*(2), 275–289. https://doi.org/10.1080/15476286.2020.1860376

McLennan, A. G. (2005). The NUDIX hydrolase superfamily. *Cellular and Molecular Life Sciences CMLS*, *63*(2), 123–143. https://doi.org/10.1007/s00018-005-5386-7

Nykamp, K., Lee, M.-H., & Kimble, J. (2008). *C. elegans* la-related protein, LARP-1, localizes to germline P bodies and attenuates Ras-MAPK signaling during oogenesis. *RNA*, *14*(7), 1378–1389. https://doi.org/10.1261/rna.1066008

Ogami, K., Oishi, Y., Sakamoto, K., Okumura, M., Yamagishi, R., Inoue, T., Hibino, M., Nogimori, T., Yamaguchi, N., Furutachi, K., Hosoda, N., Inagaki, H., & Hoshino, S. (2022). MTOR- and LARP1-dependent regulation of top mrna poly(a) tail and ribosome loading. *Cell Reports*, *41*(4), 111548. https://doi.org/10.1016/j.celrep.2022.111548

Perret, J., Hepburn, A., Cochaux, P., Vansande, J., & Dumont, j. (1990). Diadenosine 5′,5‴-P1,P4-tetraphosphate (AP4A) levels under various proliferative and cytotoxic conditions in several mammalian cell types. *Cellular Signalling*, *2*(1), 57–65. https://doi.org/10.1016/0898-6568(90)90033-7

Pizzino, G., Irrera, N., Cucinotta, M., Pallio, G., Mannino, F., Arcoraci, V., Squadrito, F., Altavilla, D., & Bitto, A. (2017). Oxidative stress: Harms and benefits for human health. *Oxidative Medicine and Cellular Longevity*, *2017*(1). https://doi.org/10.1155/2017/8416763

Ruscetti, M., Quach, B., Dadashian, E. L., Mulholland, D. J., & Wu, H. (2015). Tracking and functional characterization of epithelial–mesenchymal transition and mesenchymal tumor cells during prostate cancer metastasis. *Cancer Research*, *75*(13), 2749–2759. https://doi.org/10.1158/0008-5472.can-14-3476

Röther, S., Burkert, C., Brünger, K. M., Mayer, A., Kieser, A., & Sträßer, K. (2010). Nucleocytoplasmic shuttling of the la motif-containing protein SRO9 might link its nuclear and cytoplasmic functions. *RNA*, *16*(7), 1393–1401. https://doi.org/10.1261/rna.2089110

Saba, J. A., Huang, Z., Schole, K. L., Ye, X., Bhatt, S. D., Li, Y., Timp, W., Cheng, J., & Green, R. (2024). LARP1 binds ribosomes and top mrnas in repressed complexes. *The EMBO Journal*, *43*(24), 6555–6572. https://doi.org/10.1038/s44318-024-00294-z

Scarpin, M. R., Leiboff, S., & Brunkard, J. O. (2020). Parallel global profiling of plant Tor Dynamics reveals a conserved role for LARP1 in translation. *eLife*, *9*. https://doi.org/10.7554/elife.58795

Sipiczki, M. (2000). *Genome Biology*, *1*(2). https://doi.org/10.1186/gb-2000-1-2-reviews1011

Sobel, S. G., & Wolin, S. L. (1999). Two yeast la motif-containing proteins are RNA-binding proteins that associate with polyribosomes. *Molecular Biology of the Cell*, *10*(11), 3849–3862. https://doi.org/10.1091/mbc.10.11.3849

Stavraka, C., & Blagden, S. (2015). The LA-related proteins, a family with connections to cancer. *Biomolecules*, *5*(4), 2701–2722. https://doi.org/10.3390/biom5042701

Tcherkezian, J., Cargnello, M., Romeo, Y., Huttlin, E. L., Lavoie, G., Gygi, S. P., & Roux, P. P. (2014). Proteomic analysis of Cap-dependent translation identifies LARP1 as a key regulator of 5′top mrna translation. *Genes & Development*, *28*(4), 357–371. https://doi.org/10.1101/gad.231407.113

Teplova, M., Yuan, Y.-R., Phan, A. T., Malinina, L., Ilin, S., Teplov, A., & Patel, D. J. (2006). Structural basis for recognition and sequestration of UUUOH 3′ Temini of nascent RNA polymerase III transcripts by LA, a rheumatic disease Autoantigen. *Molecular Cell*, *21*(1), 75–85. https://doi.org/10.1016/j.molcel.2005.10.027

Vartanian, A., Alexandrov, I., Prudowski, I., McLennan, A., & Kisselev, L. (1999). Ap44A induces apoptosis in human cultured cells. *FEBS Letters, 456*(2), 175–180. https://doi.org/10.1016/S0014-5793(99)00956-4

Vinayak, J., Marrella, S. A., Hussain, R. H., Rozenfeld, L., Solomon, K., & Bayfield, M. A. (2018). Human la binds mrnas through contacts to the poly(a) tail. *Nucleic Acids Research*, *46*(8), 4228–4240. https://doi.org/10.1093/nar/gky090

Werneck-de-Castro, J. P., Peçanha, F. L., Silvestre, D. H., & Bernal-Mizrachi, E. (2021). The RNA-binding protein LARP1 is dispensable for pancreatic β-cell function and mass. *Scientific Reports*, *11*(1). https://doi.org/10.1038/s41598-021-81457-4

Yang, R., Gaidamakov, S. A., Xie, J., Lee, J., Martino, L., Kozlov, G., Crawford, A. K., Russo, A. N., Conte, M. R., Gehring, K., & Maraia, R. J. (2011). LA-related protein 4 binds poly(a), interacts with the poly(a)-binding protein MLLE domain via a variant PAM2W motif, and can promote mrna stability. *Molecular and Cellular Biology*, *31*(3), 542–556. https://doi.org/10.1128/mcb.01162-10

Yang, X., Lu, J., Su, F., Wu, J., Wang, X., Hu, Z., Yan, Z., Xu, H., Shang, X., & Guo, W. (2024). Induction of LARP1B under endoplasmic reticulum stress and its regulatory role in proliferation of esophageal squamous cell carcinoma. *Translational Oncology*, *50*, 102141. https://doi.org/10.1016/j.tranon.2024.102141

Yoo, C. J., & Wolin, S. L. (1997). The yeast La protein is required for the 3′ endonucleolytic cleavage that matures trna precursors. *Cell*, *89*(3), 393–402. https://doi.org/10.1016/s0092-8674(00)80220-2

Young, M. K., & Wang, J. D. (2024). From dusty shelves toward the spotlight: Growing evidence for AP4A as an alarmone in maintaining RNA stability and proteostasis. *Current Opinion in Microbiology*, *81*, 102536. https://doi.org/10.1016/j.mib.2024.102536

Zhu, L., Chang, Y., Li, Y., Qiao, M., & Liu, L. (2023). Biosensors based on the binding events of nitrilotriacetic acid–metal complexes. *Biosensors*, *13*(5), 507. https://doi.org/10.3390/bios13050507

7. SUPPLEMENTARY INFORMATION

7.1 Amino Acid Sequences of Slr1p, Slf1p and Sro9p

7.1.1 Complete LaM sequence of Slr1p (mutant)

10	20	30	40	50
MDVQAFLTSQ	LEYYFSIENL	SKDMFLRKHM	DDEGYVPLAF	LASFNRIKSF
60	70	80	90	100
STDLNLLHAA	AKASDIIDVA	EDLQSPMSIK	VRRKETWSPW	ILPSESRLKF
110				
EMAKYLEHHH	HHH			

7.1.2 Complete LaM sequence of Slf1p (wildtype)

10	20	30	40	50
MKSIESIKNQ	IEFYFSEENL	KTDEFLRSKF	KKANDGFIPM	SLIGKFYRMV
60	70	80	90	100
NLSLGGDPNL	ILASMREVLQ	HKETNHLEIA	LGSIEGAQKN	MADDFNPLEN
110	120	130	140	150
YFIRRENWAE	YAMESNFDEN	DDETEKYNIE	KLLGPNDLDN	YSYLEHHHHH
H				

7.1.3 Complete LaM sequence of Sro9p (wildtype)

10	20	30	40	50
MAINNIARQI	EYYFSEENLT	VDNYLRSKLS	KDGFAPLSLI	SKFYRVVNMS
60	70	80	90	100
FGGDTNLILA	ALREIVANEA	ATVNVAEGTL	LGSIEGAQKN	AAKEGDNVTG
110	120	130	140	150
EAKEPSPLDK	YFVRSKSWSN	WLPETFETEI	NIEKELVGDA	LDQFMILEHH
HHHH				

7.2 Coordinates of free and bound peaks and their corresponding CSP value

Table S1: Coordinates of free and bound peaks (in ppm) and their calculated CSP (in ppm) for the assigned amide resonances of Slr1p and bound to RNA15.

Amide resonance		free-1H (ppm)	free-15N (ppm)	bound-1H (ppm)	bound-15N (ppm)	1H-13N CSP (ppm)
3ValH	3ValN	8.44305	124.52445	8.42275	124.51308	0.014
4GlnH	4GlnN	8.43430	120.27030	8.48268	120.11952	0.038
5AlaH	5AlaN	7.85120	119.57263	7.83497	119.79566	0.025
6PheH	6PheN	8.10902	119.96878	7.92814	119.54692	0.135
7LeuH	7LeuN	8.56865	121.24887	8.38400	120.26121	0.163
8ThrH	8ThrN	9.09544	119.09442	8.90774	117.77156	0.186
9SerH	9SerN	7.74977	115.37444	7.78942	115.26168	0.03
11LeuH	11LeuN	8.32104	119.08745	8.32598	118.00303	0.107
15PheH	15PheN	7.28816	111.31533	7.21920	109.77749	0.16
16SerH	16SerN	7.27865	116.66532	7.42103	116.86572	0.102
17IleH	17IleN	8.68173	122.67197	7.42103	116.86572	0.049
18GluH	18GluN	9.04383	121.25662	8.87168	120.14249	0.164
19AsnH	19AsnN	7.57019	115.79321	7.43774	115.74746	0.093
20LeuH	20LeuN	8.77461	119.68013	8.78376	119.49205	0.02
21SerH	21SerN	7.75633	109.01946	7.65438	109.27147	0.076
22LysH	22LysN	7.2797	116.6740	7.32400	115.6500	0.106
24MetH	24MetN	8.12421	123.06384	8.12625	123.24802	0.018
25PheH	25PheN	8.52037	120.78558	8.73569	120.66603	0.153

27ArgH	27ArgN	7.68777	116.12822	7.65027	116.45590	0.042
28LysH	28LysN	8.69550	119.81335	8.65220	120.03856	0.038
29HisH	29HisN	7.67569	115.10386	7.63003	115.01879	0.034
30MetH	30MetN	7.28256	119.19164	7.25810	119.12771	0.019
31AspH	31AspN	8.38961	122.80734	8.37388	122.73061	0.014
32AspH	32AspN	7.79281	111.85039	7.83497	112.24577	0.049
33GluH	33GluN	8.41722	117.62006	8.41942	117.61665	0.001
34GlyH	34GlyN	7.96251	129.88196	7.95625	129.95285	0.009
35TyrH	35TyrN	8.10283	117.77112	8.09051	117.75132	0.009
36ValH	36ValN	9.23119	114.14066	9.21388	113.76384	0.039
38LeuH	38LeuN	8.98929	128.98869	8.98807	128.94080	0.005
39AlaH	39AlaN	9.10973	117.03670	9.09244	117.02264	0.013
40PheH	40PheN	6.77423	115.18719	6.69040	115.11999	0.06
41LeuH	41LeuN	6.67963	120.84584	6.52453	120.37584	0.119
42AlaH	42AlaN	7.31962	116.28057	7.29858	115.36288	0.092
43SerH	43SerN	7.11183	109.24321	7.11040	110.02038	0.077
44PheH	44PheN	7.71985	124.51502	7.72696	125.27212	0.075
47IleH	47IleN	7.37814	113.37773	7.24313	112.95696	0.104
49SerH	49SerN	7.78572	111.73361	7.89078	113.04603	0.150
50PheH	50PheN	8.05767	119.10282	7.87798	119.04675	0.104
51SerH	51SerN	8.18802	112.06441	8.38008	112.24046	0.137
52ThrH	52ThrN	8.28044	114.26300	8.26256	114.57348	0.033
53AspH	53AspN	8.25780	122.59360	8.28280	122.48772	0.021

54LeuH	54LeuN	8.86792	127.99831	8.90900	128.02363	0.029
55AsnH	55AsnN	8.39228	117.22106	8.40424	116.86072	0.037
56LeuH	56LeuN	7.70769	124.04806	7.63999	124.03868	0.048
57LeuH	57LeuN	7.84844	119.53190	7.68569	119.69446	0.116
58HisH	58HisN	8.46337	119.46319	8.49280	119.18843	0.035
59AlaH	59AlaN	7.81586	121.21421	7.79195	121.25302	0.017
60AlaH	60AlaN	8.39440	121.00446	8.39159	120.46362	0.053
61AlaH	61AlaN	8.23537	121.42853	8.29292	121.11133	0.052
62LysH	62LysN	8.14357	116.19909	8.16388	115.84867	0.037
63AlaH	63AlaN	7.20623	118.08143	7.20749	118.13590	0.005
64SerH	64SerN	7.12034	111.48071	7.13570	111.49685	0.011
65AspH	65AspN	9.01114	126.15350	9.02024	126.00034	0.017
66IleH	66IleN	8.33030	113.29017	8.38147	113.78408	0.061
67IleH	67IleN	6.92943	120.19082	6.91725	120.02675	0.018
68AspH	68AspN	9.05241	126.11466	9.06537	126.15506	0.01
69ValH	69ValN	8.31175	121.34189	8.37894	121.23277	0.049
70AlaH	70AlaN	9.08396	130.89176	9.10272	130.96491	0.015
71GluH	71GluN	8.30206	120.30678	8.35172	120.24941	0.036
72AspH	72AspN	8.41098	123.01397	8.40876	123.12449	0.011
73LeuH	73LeuN	8.51429	123.58396	8.51367	123.56429	0.002
74GlnH	74GlnN	8.36200	116.36607	8.35617	116.29397	0.008
75SerH	75SerN	7.62173	114.30498	7.61484	114.24963	0.007
78SerH	78SerN	8.03727	115.20050	8.02473	115.18071	0.009

80LysH	80LysN	8.96745	128.07599	8.94063	128.08689	0.018
81ValH	81ValN	9.10735	112.82600	9.09497	113.33878	0.051
83ArgH	83ArgN	9.03412	122.53336	9.08991	122.38651	0.042
90TrpH	90TrpN	6.49332	113.41664	6.40197	113.31854	0.065
91IleH	91IleN	6.87531	116.13857	6.82450	116.15228	0.036
94SerH	94SerN	8.89673	118.27017	8.88497	118.23711	0.009
95GluH	95GluN	9.45506	119.64696	9.46943	119.61349	0.01
96SerH	96SerN	8.18384	115.41954	8.15882	115.34264	0.019
97ArgH	97ArgN	7.19791	118.56992	7.15183	118.35855	0.039
98LeuH	98LeuN	7.76684	121.40573	7.78099	120.62477	0.078
99LysH	99LysN	8.09743	119.55439	8.08039	119.43133	0.017
100PheH	100PheN	8.93589	125.68744	8.88916	125.58774	0.035
101GluH	101GluN	8.01106	127.64877	8.14206	127.83387	0.094
103AlaH	103AlaN	8.50628	121.77423	8.50545	122.26507	0.049
104LysH	104LysN	7.65983	117.34219	7.70593	117.60963	0.042
105TyrH	105TyrN	7.76570	119.80519	7.75400	119.79566	0.009
106LeuH	106LeuN	8.01421	120.84942	8.03232	120.88868	0.013
107GluH	107GluN	7.94069	119.65015	7.95388	119.75518	0.014

Table S2: Coordinates of free and bound peaks (in ppm) and their calculated CSP (in ppm) for the assigned amide resonances of Slr1p and bound to RNA6.

Amide resonance		free-1H (ppm)	free-15N (ppm)	bound-1H (ppm)	bound-15N (ppm)	1H-13N CSP (ppm)
3ValH	3ValN	8.42337	124.46176	8.40062	124.36766	0.019
4GlnH	4GlnN	8.45604	120.47119	8.47406	120.11003	0.044
5AlaH	5AlaN	7.9236	120.31477	7.82873	119.76679	0.086
6PheH	6PheN	8.10946	119.91702	7.88217	119.37376	0.169
7LeuH	7LeuN	8.55969	121.32199	8.36422	120.24934	0.175
8ThrH	8ThrN	9.10754	119.18896	8.90994	117.78633	0.197
9SerH	9SerN	7.74645	115.33051	7.77957	115.17901	0.028
10GlnH	10GlnN	8.11445	122.99592	8.16625	123.86377	0.012
11LeuH	11LeuN	8.3138	119.10929	8.3446	118.48224	0.066
15PheH	15PheN	7.2806	111.3577	7.27738	109.96572	0.138
16SerH	16SerN	7.31759	116.27814	7.47041	116.86333	0.122
17IleH	17IleN	8.6768	122.5931	8.66179	122.41343	0.021
18GluH	18GluN	8.70836	120.18495	8.92017	120.25492	0.150
19AsnH	19AsnN	7.56866	115.78293	7.5285	115.87949	0.031
20LeuH	20LeuN	8.78188	119.68191	8.83576	119.48034	0.043
21SerH	21SerN	7.76063	109.02425	7.69699	109.32786	0.054
22LysH	22LysN	7.27974	116.674	7.32807	115.68672	0.103
23AspH	23AspN	8.00686	122.66711	7.96044	122.47534	0.038

24MetH	24MetN	8.17603	123.09921	8.21047	123.28306	0.030
25PheH	25PheN	8.50840	120.7460	8.73280	120.3678	0.163
27ArgH	27ArgN	7.67847	116.0686	7.66612	116.33475	0.028
28LysH	28LysN	8.68696	119.80829	8.56261	119.99551	0.090
29HisH	29HisN	7.66634	115.11437	7.58871	115.10329	0.054
30MetH	30MetN	7.2813	119.19641	7.24108	119.12633	0.029
31AspH	31AspN	8.38349	122.79893	8.33571	122.64544	0.037
32AspH	32AspN	7.85194	112.2796	7.83464	112.23432	0.013
33GluH	33GluN	8.41365	117.63934	8.42072	117.65524	0.005
34GlyH	34GlyN	7.95369	129.86238	7.96195	129.95124	0.010
35TyrH	35TyrN	8.09203	117.78211	8.0828	117.75261	0.007
36ValH	36ValN	9.22264	114.01615	9.19552	113.57216	0.048
38LeuH	38LeuN	8.9888	129.03424	8.98537	128.98216	0.006
39AlaH	39AlaN	9.10992	117.04536	9.11178	117.08693	0.004
40PheH	40PheN	6.77959	115.21659	6.66712	115.12596	0.08
41LeuH	41LeuN	6.66982	120.85094	6.52247	120.26721	0.120
43SerH	43SerN	7.11134	109.22681	7.11571	109.90146	0.067
44PheH	44PheN	7.7257	124.53502	7.81493	125.19544	0.091
47IleH	47IleN	7.38417	113.42624	7.22912	113.24101	0.111
49SerH	49SerN	7.78572	111.73361	7.89078	113.04603	0.150
50PheH	50PheN	8.05833	119.19288	7.87396	119.07805	0.131
51SerH	51SerN	8.18551	112.07614	8.40536	112.19489	0.155
52ThrH	52ThrN	8.27861	114.29472	8.29147	114.6083	0.032

53AspH	53AspN	8.25426	122.61971	8.31061	122.59617	0.04
55AsnH	55AsnN	8.38658	117.23129	8.40108	116.86584	0.019
56LeuH	56LeuN	7.69932	124.07724	7.6351	124.12222	0.045
57LeuH	57LeuN	7.84712	119.52906	7.7042	119.72423	0.103
58HisH	58HisN	8.446	119.47455	8.49014	119.24202	0.039
59AlaH	59AlaN	7.75145	121.37839	7.78254	121.30448	0.024
60AlaH	60AlaN	8.43228	120.14111	8.39771	120.22791	0.026
61AlaH	61AlaN	8.31172	121.38503	8.29725	121.16022	0.025
62LysH	62LysN	8.1052	115.87187	8.16412	115.85109	0.042
63AlaH	63AlaN	7.19456	118.55506	7.20061	118.12732	0.043
64SerH	64SerN	7.14346	111.69231	7.13621	111.52595	0.017
65AspH	65AspN	9.01819	125.93157	9.01138	125.98576	0.07
66IleH	66IleN	8.34829	113.22274	8.38189	113.73113	0.056
67IleH	67IleN	6.93158	120.251	6.91112	120.11442	0.02
68AspH	68AspN	8.98699	125.9495	9.06487	126.26795	0.064
69ValH	69ValN	8.41846	121.1207	8.38164	121.32096	0.032
70AlaH	70AlaN	9.08647	130.90646	9.10136	131.01056	0.015
71GluH	71GluN	8.3723	120.23435	8.35619	120.4208	0.022
72AspH	72AspN	8.40843	123.10235	8.41234	123.04168	0.007
73LeuH	73LeuN	8.52207	123.61014	8.51881	123.56018	0.005
74GlnH	74GlnN	8.36017	116.30113	8.35988	116.33396	0.004
75SerH	75SerN	7.61283	114.3161	7.61531	114.26006	0.006
77MetH	77MetN	8.39394	115.17435	8.37729	115.00315	0.021

78SerH	78SerN	8.04557	115.18018	8.02588	115.18136	0.014
79IleH	79IleN	7.36306	121.99024	7.3235	121.99899	0.028
80LysH	80LysN	8.988	128.1276	8.93877	128.16071	0.035
81ValH	81ValN	9.1109	112.87136	9.09198	113.17421	0.033
83ArgH	83ArgN	9.02259	122.50571	9.09431	122.45229	0.05
88SerH	88SerN	7.69873	122.14941	7.68151	122.27602	0.017
90TrpH	90TrpN	6.50927	113.4721	6.39631	113.32078	0.081
91IleH	91IleN	6.87521	116.12607	6.82705	116.18158	0.034
92LeuH	92LeuN	9.38127	129.25439	9.36372	129.61841	0.038
94SerH	94SerN	8.90035	118.29927	8.8932	118.29957	0.005
95GluH	95GluN	9.45625	119.64161	9.47329	119.60707	0.013
96SerH	96SerN	8.18882	115.44557	8.16261	115.38628	0.019
97ArgH	97ArgN	7.16364	118.01236	7.13543	118.20734	0.046
98LeuH	98LeuN	7.87739	120.71188	7.74136	120.64004	0.096
99LysH	99LysN	8.09139	119.48237	8.05193	119.18757	0.04
101GluH	101GluN	8.15787	127.29538	8.17027	127.52148	0.024
102MetH	102MetN	8.19125	124.85159	8.23534	124.47467	0.049
103AlaH	103AlaN	8.50272	121.71429	8.51561	122.13179	0.042
104LysH	104LysN	7.65777	117.35238	7.69827	117.5674	0.035
105TyrH	105TyrN	7.78303	119.87146	7.76033	119.80089	0.018
106LeuH	106LeuN	8.00843	120.96434	8.03236	120.89064	0.018
107GluH	107GluN	7.95304	119.67166	7.96432	119.77899	0.013

Table S3: Coordinates of free and bound peaks (in ppm) and their calculated CSP (in ppm) for the assigned amide resonances of Slf1p and bound to RNA6.

Amide resonance		free-1H (ppm)	free-15N (ppm)	bound-1H (ppm)	bound-15N (ppm)	1H-13N CSP (ppm)
2LysH	2LysN	8.37743	121.7441	8.37776	121.72316	0.002
3SerH	3SerN	8.23811	116.44	8.23725	116.42669	0.001
4IleH	4IleN	8.16801	122.34489	8.1952	122.42128	0.021
5GluH	5GluN	8.50186	124.62331	8.50299	124.66989	0.005
6SerH	6SerN	8.11618	114.59084	8.11885	114.61609	0.003
7IleH	7IleN	8.3102	122.51139	8.30756	122.39098	0.012
8LysH	8LysN	7.99467	120.92127	7.99791	120.92035	0.002
16SerH	16SerN	7.6266	117.42929	7.64888	117.70444	0.031
17GluH	17GluN	9.09838	122.37	9.10009	122.34795	0.003
18GluH	18GluN	8.53569	115.79547	8.60166	115.79997	0.047
19AsnH	19AsnN	7.47652	116.46673	7.43509	116.37718	0.031
20LeuH	20LeuN	8.43945	116.9771	8.44885	116.71895	0.027
21LysH	21LysN	7.54958	115.78925	7.50356	115.87836	0.034
22ThrH	22ThrN	7.24072	129.94021	7.24411	129.41657	0.052
24GluH	24GluN	8.14644	125.25541	8.09803	125.60133	0.048
27ArgH	27ArgN	7.87598	114.62453	7.93245	114.70927	0.04
28SerH	28SerN	7.81145	112.90579	7.84759	113.04024	0.029
29LysH	29LysN	7.42534	117.84568	7.39433	117.76471	0.023

30PheH	30PheN	7.55339	121.83052	7.58747	121.82059	0.024
31LysH	31LysN	8.1368	122.08071	8.13263	122.04178	0.005
32LysH	32LysN	9.70008	127.65913	9.71419	127.72132	0.012
33AlaH	33AlaN	9.0616	121.34805	9.06713	121.3708	0.004
34AsnH	34AsnN	6.81068	111.40593	6.78848	111.36007	0.017
35AspH	35AspN	8.11626	120.51943	8.12327	120.49157	0.006
36GlyH	36GlyN	6.8655	123.76195	6.86167	123.72524	0.004
37PheH	37PheN	7.08602	115.45435	7.07459	115.40497	0.009
38IleH	38IleN	9.03926	117.08364	9.06312	117.47568	0.042
40MetH	40MetN	9.04695	123.77433	9.07386	123.87446	0.022
43IleH	43IleN	7.45636	119.13255	7.42961	119.18161	0.019
49MetH	49MetN	9.0470	123.7743	9.0739	123.8745	0.021
55GlyH	55GlyN	8.34987	109.98791	8.35306	109.99783	0.002
59AsnH	59AsnN	8.6373	113.47574	8.63913	113.4896	0.002
60LeuH	60LeuN	7.73034	118.98105	7.72988	118.9898	0.001
63AlaH	63AlaN	7.78388	119.97389	7.73139	119.91157	0.038
64SerH	64SerN	7.89762	116.15737	7.89761	116.29179	0.013
69LeuH	69LeuN	7.88624	118.99799	7.85449	118.85607	0.027
70GlnH	70GlnN	7.90378	117.04881	7.88372	117.02702	0.014
71HisH	71HisN	7.50342	116.94535	7.50801	116.86672	0.008
72LysH	72LysN	7.41786	123.89969	7.4202	123.89899	0.001
73GluH	73GluN	8.87547	117.74276	8.88395	117.80242	0.009
74ThrH	74ThrN	7.73652	107.92506	7.72688	107.94041	0.007

75AsnH	75AsnN	8.25115	117.68615	8.2418	117.6351	0.008
76HisH	76HisN	8.44162	112.8037	8.44569	112.75423	0.006
77LeuH	77LeuN	8.36346	117.12879	8.36651	117.12033	0.003
78GluH	78GluN	8.71707	117.63153	8.71277	117.56171	0.007
79IleH	79IleN	8.71037	120.28061	8.72266	120.23981	0.01
80AlaH	80AlaN	9.45777	128.00959	9.44998	127.99074	0.006
81LeuH	81LeuN	8.47328	121.53996	8.47241	121.59513	0.005
82GlyH	82GlyN	8.8981	112.7459	8.91126	112.87393	0.016
83SerH	83SerN	8.60559	114.1475	8.59958	114.13111	0.005
84IleH	84IleN	8.96977	122.52812	8.97017	122.54548	0.002
85GluH	85GluN	8.96116	129.61689	8.96051	129.6079	0.001
86GlyH	86GlyN	8.72084	113.31426	8.71843	113.31121	0.002
87AlaH	87AlaN	7.89065	123.20329	7.8909	123.20962	0.001
88GlnH	88GlnN	8.59158	120.13666	8.59229	120.16187	0.002
89LysH	89LysN	8.35111	122.92416	8.35194	122.92068	0.001
90AsnH	90AsnN	8.56813	120.35073	8.56398	120.32298	0.004
91MetH	91MetN	8.4746	121.19062	8.47283	121.29219	0.01
92AlaH	92AlaN	8.26358	123.48355	8.26445	123.51227	0.003
93AspH	93AspN	8.10619	118.71841	8.11997	118.73331	0.01
94AspH	94AspN	8.12655	119.72476	8.1301	119.72404	0.002
95PheH	95PheN	8.13433	121.2374	8.11349	121.26492	0.015
96AsnH	96AsnN	8.34969	124.50402	8.35987	124.63729	0.015
99GluH	99GluN	7.55655	115.77985	7.57226	115.84633	0.012

101TyrH	101TyrN	6.89931	114.3976	6.91513	114.31762	0.014
102PheH	102PheN	9.10636	120.42169	9.07151	120.22535	0.031
103IleH	103IleN	9.65602	121.85733	9.68802	121.9928	0.026
104ArgH	104ArgN	8.66844	120.20066	8.67067	120.14137	0.006
105ArgH	105ArgN	7.73542	117.51856	7.67823	117.4502	0.041
106GluH	106GluN	9.19641	123.33667	9.213	123.31897	0.012
107AsnH	107AsnN	8.32964	115.01113	8.31666	114.94114	0.012
108TrpH	108TrpN	7.21268	117.98011	7.21019	117.9823	0.002
109AlaH	109AlaN	7.16484	124.37928	7.1578	124.40155	0.005
110GluH	110GluN	7.67603	116.15557	7.67485	116.13067	0.003
112AlaH	112AlaN	7.25841	121.87549	7.24494	121.86819	0.009
113MetH	113MetN	8.62459	121.03197	8.63768	121.08369	0.011
114GluH	114GluN	8.55526	122.31399	8.54689	122.3169	0.006
117PheH	117PheN	8.20823	120.15869	8.20408	120.13439	0.004
118AspH	118AspN	8.27041	121.41832	8.27159	121.41895	0.001
123GluH	123GluN	8.31577	120.68202	8.31308	120.65883	0.003
124ThrH	124ThrN	8.01789	115.69493	7.99679	115.7512	0.016
125GluH	125GluN	8.30022	124.36267	8.30872	124.36999	0.006
126LysH	126LysN	8.40232	123.69684	8.4052	123.73848	0.005
127TyrH	127TyrN	8.1999	123.65701	8.19617	123.5935	0.007
128AsnH	128AsnN	9.03267	123.06262	9.03163	123.07855	0.002
129IleH	129IleN	8.51909	126.11819	8.5156	126.1292	0.002
130GluH	130GluN	9.2419	129.45566	9.2546	129.48021	0.009

131LysH	131LysN	7.42406	113.72469	7.42325	113.65337	0.007
132LeuH	132LeuN	8.66647	125.05906	8.66663	125.00499	0.005
133LeuH	133LeuN	9.0323	122.66102	9.04582	122.59888	0.012
134GlyH	134GlyN	9.41587	110.15351	9.4279	110.11912	0.009
136AsnH	136AsnN	8.53674	117.7058	8.53754	117.67251	0.003
137AspH	137AspN	7.9511	120.30802	7.95246	120.34992	0.004
138LeuH	138LeuN	8.11641	122.44558	8.11983	122.46384	0.003
139AspH	139AspN	8.15452	119.38809	8.15489	119.29821	0.009
140AsnH	140AsnN	8.11021	118.35104	8.11009	118.36066	0.001
142SerH	142SerN	8.15719	117.23625	8.1615	117.24376	0.004
143TyrH	143TyrN	7.96212	121.7196	7.9618	121.72618	0.001
144LeuH	144LeuN	7.81968	122.41485	7.82223	122.37839	0.004

Table S4: Coordinates of free and bound peaks (in ppm) and their calculated CSP for the assigned methyl resonances of Slf1p bound to RNA6.

Methyl resonance		**free-1H (ppm)**	**free-13C (ppm)**	**bound-1H (ppm)**	**bound-13C (ppm)**	**1H-13C CSP**
8LysHg2	8LysCg2	1.488	24.978	1.502	24.941	0.024631281
20LeuHd2	20LeuCd2	0.617	23.695	0.624	23.747	0.029329166
20LeuHg	20LeuCg	0.337	25.939	0.341	25.922	0.010134101
21LysHg2	21LysCg	1.54	25.564	1.539	25.55	0.007733046
21LysHg3	21LysCg	1.735	25.518	1.742	25.501	0.011649034
29LysHd2	29LysCd	1.361	27.633	1.328	27.596	0.03872596
31LysHd2	31LysCd	1.747	28.349	1.757	28.388	0.023586013
33AlaHb	33AlaCb	1.315	18.791	1.308	18.815	0.014892951
38IleHd1	38IleCd1	0.903	14.822	0.889	14.819	0.014096099
38IleHg2	38IleCg2	1.123	18.295	1.107	18.169	0.070843489
58ProHg2	58ProCg	2.074	27.567	2.082	27.572	0.008455767
63AlaHb	63AlaCb	1.547	18.481	1.565	18.446	0.026296388
69LeuHd2	69LeuCd2	0.912	23.66	0.91	23.579	0.044410584
72LysHg2	72LysCg	1.575	23.937	1.576	23.937	0.001

74ThrHg2	74ThrCg2	1.206	21.567	1.201	21.637	0.03866523
77LeuHd2	77LeuCd2	0.474	23.06	0.473	23	0.032878564
79IleHd1	79IleCd1	0.727	13.424	0.723	13.387	0.020656718
79IleHg2	79IleCg2	1.024	18.09	1.017	18.03	0.033600595
81LeuHd1	81LeuCd1	0.72	24.067	0.717	23.948	0.065247988
81LeuHd2	81LeuCd2	0.705	25.736	0.719	25.788	0.031736414
81LeuHg	81LeuCg	1.501	27.255	1.492	27.265	0.010535654
84IleHd1	84IleCd1	0.913	13.427	0.912	13.395	0.017555626
84IleHg13	84IleCg1	1.933	28.169	1.926	28.1819	0.009946004
84IleHg2	84IleCg2	1.067	17.36	1.063	17.328	0.017977764
87AlaHb	87AlaCb	1.373	19.2143	1.378	19.276	0.03414787
89LysHg2	89LysCg	1.412	24.742	1.413	24.715	0.014822281
92AlaHb	92AlaCb	1.418	19.484	1.425	19.429	0.030927334
103IleHd1	103IleCd1	0.584	14.914	0.578	14.974	0.033406586
103IleHg12	103IleCg1	0.34	28.395	0.3351	28.4773	0.045343103
103IleHg2	103IleCg2	0.799	16.059	0.81	16.062	0.01112205
109AlaHb	109AlaCb	0.263	16.743	0.259	16.599	0.078973413
112AlaHb	112AlaCb	1.677	19.852	1.674	19.806	0.025373214
124ThrHg2	124ThrCg2	1.206	22.032	1.21	22.075	0.023889328
126LysHg2	126LysCg	1.243	24.581	1.243	24.576	0.002738613
129IleHd1	129IleCd1	-0.71	8.316	-0.707	8.323	0.004868265
129IleHg2	129IleCg2	0.262	17.026	0.269	16.97	0.031461087
131LysHg2	131LysCg	1.215	23.795	1.215	23.78	0.008215838
132LeuHd1	132LeuCd1	0.985	25.142	0.984	25.093	0.026857029
132LeuHg	132LeuCg	1.349	26.819	1.347	26.808	0.006348228
132LeuHd2	132LeuCd2	0.814	23.356	0.81	23.41	0.029846273
133LeuHg	133LeuCg	0.963	26.423	0.966	26.417	0.004449719
135ProHg2	135ProCg2	1.98	27.315	1.982	27.379	0.035111252
144LeuHd2	144LeuCd2	0.769	23.573	0.774	23.524	0.027300183
144LeuHd1	144LeuCd1	0.816	25.321	0.82	25.273	0.026593232

Table S5: Coordinates of free and bound peaks (in ppm) and their calculated CSP for the assigned methyl resonances of Slr1p and bound to RNA15.

Methyl resonance		**free-1H (ppm)**	**free-13C (ppm)**	**bound-1H (ppm)**	**bound-13C (ppm)**	**1H-13C CSP**
1MetHe	1MetCe	1.7643	17.0418	1.7825	17.1051	0.03915746
3ValHg1	3ValCg1	1.051	21.601	1.008	21.582	0.04424138
3ValHg2	3ValCg2	1.117	22.423	1.104	22.466	0.02690167
5AlaHb	5AlaCb	1.417	18.182	1.395	18.133	0.03470303
7LeuHd1	7LeuCd1	1.006	23.465	1.055	23.705	0.14028899
7LeuHd2	7LeuCd2	0.876	26.169	0.843	26.159	0.03345146
8ThrHg2	8ThrCg2	1.178	22.393	1.153	22.252	0.0811745

11LeuHd1	11LeuCd1	0.833	24.25	0.925	24.077	0.13207081
11LeuHd2	11LeuCd2	0.801	26.477	0.76	26.007	0.26067413
17IleHd1	17IleCd1	1.029	11.834	1.021	11.695	0.0765526
17IleHg2	17IleCg2	1.027	17.595	1.015	17.422	0.09551283
20LeuHd1	20LeuCd1	0.068	25.388	0.05	25.33	0.03651301
20LeuHd2	20LeuCd2	0.553	24.363	0.498	24.191	0.10908804
26LeuHd1	26LeuCd1	0.485	27.072	0.417	26.773	0.17732541
26LeuHd2	26LeuCd2	0.794	24.729	0.809	25.148	0.22998543
30MetHe	30MetCe	1.764	17.042	1.785	17.084	0.03114803
36ValHg1	36ValCg1	1.02	22.598	0.999	22.592	0.02125559
36ValHg2	36ValCg2	1.025	20.928	1.035	20.795	0.07353027
38LeuHd1	38LeuCd1	0.767	25.613	0.76	25.559	0.03039408
38LeuHd2	38LeuCd2	0.8174	23.3101	0.8021	23.327	0.0178822
39AlaHb	39AlaCb	1.363	18.671	1.358	18.599	0.03975173
41LeuHd1	41LeuCd1	0.213	23.695	0.284	23.697	0.07100845
41LeuHd2	41LeuCd2	0.5943	26.2232	0.8133	27.2846	0.62123425
42AlaHb	42AlaCb	1.305	18.476	1.312	18.3	0.09665299
47IleHd1	47IleCd1	0.81	12.44	0.82	11.117	0.72470594
47IleHg2	47IleCg2	1.002	18.993	1.037	19.274	0.15783948
52ThrHg2	52ThrCg2	1.253	22.007	1.268	21.872	0.07544866
54LeuHd1	54LeuCd1	0.796	24.175	0.7921	24.351	0.09634447
54LeuHd2	54LeuCd2	0.846	24.779	0.838	24.837	0.03275973
56LeuHd1	56LeuCd1	0.944	24.932	0.963	25.152	0.12160871
56LeuHd2	56LeuCd2	0.995	24.135	1.002	23.996	0.07664593
57LeuHd1	57LeuCd1	0.944	25.044	0.963	25.152	0.06213051
57LeuHd2	57LeuCd2	0.827	25.846	0.8371	26.4233	0.3163615
59AlaHb	59AlaCb	1.426	17.839	1.424	17.683	0.08546812
60AlaHb	60AlaCb	1.541	19.398	1.541	19.633	0.1287148
61AlaHb	61AlaCb	1.383	18.238	1.346	18.086	0.09110543
63AlaHb	63AlaCb	1.403	19.378	1.397	19.163	0.1179131
66IleHd1	66IleCd1	0.818	13.893	0.817	13.736	0.08599826
66IleHg2	66IleCg2	0.903	17.721	0.908	17.69	0.01770028
67IleHd1	67IleCd1	0.652	13.422	0.656	13.31	0.0614752
67IleHg2	67IleCg2	0.561	17.992	0.537	17.982	0.02461707
69ValHg1	69ValCg1	0.84	22.197	0.828	22.009	0.1036687
69ValHg2	69ValCg2	0.903	22.318	0.889	22.313	0.01426534
70AlaHb	70AlaCb	0.897	21.423	0.905	21.336	0.04831873
73LeuHd1	73LeuCd1	0.897	25.153	0.889	25.167	0.01108152
73LeuHd2	73LeuCd2	0.8251	23.0503	0.8155	23.0152	0.02148867

77MetHe	77MetCe	2.0374	17.26	2.0335	17.2755	0.00934264
79IleHd1	79IleCd1	0.357	12.014	0.351	12.09	0.0420571
79IleHg2	79IleCg2	0.597	19.356	0.586	19.35	0.01148042
81ValHg1	81ValCg1	0.8121	24.1292	0.7521	24.04	0.07737566
81ValHg2	81ValCg2	0.774	20.166	0.738	20.59	0.23500808
86ThrHg2	86ThrCg2	1.227	23.164	1.221	23.31	0.08019227
91IleHd1	91IleCd1	1.165	15.081	1.149	15.07	0.01709678
91IleHg2	91IleCg2	1.139	18.804	1.106	18.73	0.05226662
92LeuHd1	92LeuCd1	0.914	26.907	0.859	26.91	0.05502454
92LeuHd2	92LeuCd2	0.951	22.386	0.9137	22.3483	0.04263422

Table S6: Coordinates of free and bound peaks (in ppm) and their calculated CSP for the assigned methyl resonances of Slr1p and bound to RNA6.

Methyl resonance		**free-1H (ppm)**	**free-13C (ppm)**	**bound-1H (ppm)**	**bound-13C (ppm)**	**1H-13C CSP**
1MetHe	1MetCe	1.7643	17.0418	1.7825	17.1051	0.03915746
3ValHg1	3ValCg1	1.051	21.601	1.008	21.582	0.04424138
3ValHg2	3ValCg2	1.117	22.423	1.104	22.466	0.02690167
5AlaHb	5AlaCb	1.417	18.182	1.395	18.133	0.03470303
7LeuHd1	7LeuCd1	1.006	23.465	1.055	23.705	0.14028899
7LeuHd2	7LeuCd2	0.876	26.169	0.843	26.159	0.03345146
8ThrHg2	8ThrCg2	1.178	22.393	1.153	22.252	0.0811745
11LeuHd1	11LeuCd1	0.833	26.477	0.76	26.007	0.26757989
11LeuHd2	11LeuCd2	0.801	24.25	0.925	24.077	0.15605992
17IleHd1	17IleCd1	1.029	11.834	1.021	11.695	0.0765526
17IleHg2	17IleCg2	1.027	17.595	1.015	17.422	0.09551283
20LeuHd1	20LeuCd1	0.068	25.388	0.05	25.33	0.03651301
20LeuHd2	20LeuCd2	0.553	24.363	0.498	24.191	0.10908804
26LeuHd1	26LeuCd1	0.485	27.072	0.417	26.773	0.17732541
26LeuHd2	26LeuCd2	0.794	24.729	0.809	25.148	0.22998543
30MetHe	30MetCe	2.1627	19.2206	2.1284	19.2242	0.03435663
36ValHg1	36ValCg1	1.02	22.598	0.995	22.5591	0.03284757
36ValHg2	36ValCg2	1.025	20.928	1.0306	20.8831	0.02522227
38LeuHd1	38LeuCd1	0.767	25.613	0.76	25.559	0.03039408
38LeuHd2	38LeuCd2	0.8174	23.3101	0.8021	23.327	0.0178822
39AlaHb	39AlaCb	1.363	18.671	1.358	18.599	0.03975173
41LeuHd1	41LeuCd1	0.213	23.695	0.284	23.697	0.07100845
42AlaHb	42AlaCb	1.305	18.476	1.312	18.3	0.09665299

47IleHd1	47IleCd1	0.81	12.44	0.82	11.117	0.72470594
47IleHg2	47IleCg2	1.002	18.993	1.037	19.274	0.15783948
52ThrHg2	52ThrCg2	1.253	22.007	1.268	21.872	0.07544866
54LeuHd2	54LeuCd2	0.846	24.779	0.838	24.837	0.03275973
57LeuHd1	57LeuCd1	0.944	25.044	0.963	25.152	0.06213051
59AlaHb	59AlaCb	1.426	17.839	1.424	17.683	0.08546812
60AlaHb	60AlaCb	1.541	19.398	1.541	19.633	0.1287148
61AlaHb	61AlaCb	1.383	18.238	1.346	18.086	0.09110543
63AlaHb	63AlaCb	1.403	19.378	1.397	19.163	0.1179131
66IleHd1	66IleCd1	0.818	13.893	0.817	13.736	0.08599826
66IleHg2	66IleCg2	0.903	17.721	0.908	17.69	0.01770028
67IleHd1	67IleCd1	0.652	13.422	0.656	13.31	0.0614752
67IleHg2	67IleCg2	0.561	17.992	0.537	17.982	0.02461707
69ValHg1	69ValCg1	0.84	22.197	0.828	22.009	0.1036687
69ValHg2	69ValCg2	0.903	22.318	0.889	22.313	0.01426534
70AlaHb	70AlaCb	0.897	21.423	0.905	21.336	0.04831873
73LeuHd1	73LeuCd1	0.897	25.153	0.889	25.167	0.01108152
73LeuHd2	73LeuCd2	0.8251	23.0503	0.8155	23.0152	0.02148867
77MetHe	77MetCe	2.0374	17.26	2.0335	17.2755	0.00934264
79IleHd1	79IleCd1	0.357	12.014	0.351	12.091	0.0425993
79IleHg2	79IleCg2	0.597	19.356	0.586	19.347	0.01205404
81ValHg1	81ValCg1	0.8121	24.1292	0.752	24.019	0.08517759
81ValHg2	81ValCg2	0.774	20.166	0.738	20.562	0.21986541
86ThrHg2	86ThrCg2	1.227	23.164	1.221	23.306	0.07800769
91IleHd1	91IleCd1	1.165	15.081	1.149	15.077	0.0161493
91IleHg2	91IleCg2	1.139	18.804	1.106	18.732	0.05142179
92LeuHd1	92LeuCd1	0.914	26.907	0.859	26.924	0.05578261
92LeuHd2	92LeuCd2	0.9513	22.3864	0.9137	22.3483	0.04300283

7.3 3D NMR experiment processing script

```
#!/bin/csh                                                    Tells the system to execute this script using the C shell

set expt = 1008                                               Defines the experiment identifier as 1008, which will be used throughout the script to reference data files and directories

# nuslist 481                                                 Documents that this experiment uses 481 non-uniformly sampled (NUS) points

cp {$expt}/nuslist .                                          Copies the NUS list file to the current directory

bruk2pipe -in {$expt}/ser \                                   Points to the serial data file (ser) in the experiment directory containing the raw 3D NMR data
  -bad 0.0 -ext -aswap -AMX -decim 2200 -dspfvs 20 -grpdly 67.986083984375  \   Sampling parameters specific to the experiment
  -xN              1280  -yN                4  -zN              481  \
  -xT               640  -yT                2  -zT              240  \        Complex and total point acquired in each dimension
  -xMODE            DQD  -yMODE          Real  -zMODE          Real  \        - X: DQD (Digital Quadrature Detection)
  -xSW         9090.909  -ySW         1774.308  -zSW        13192.612  \        - Y: Real (real data only) - Z: Real (real data only)
  -xOBS         700.283  -yOBS          70.967  -zOBS         176.092  \        Defines the frequency range covered in each dimension
  -xCAR           4.773  -yCAR         120.078  -zCAR          41.736  \        Specifies the spectrometer frequency for each nucleus being observed
  -xLAB               H  -yLAB               N  -zLAB               C  \        Defines the center of the spectral window in chemical shift units
  -ndim               3  -aq2D          States                          \       Identifies the observed nuclei (H = proton, N = nitrogen, C = carbon)
| nmrPipe -fn MAC -macro $NMRTXT/ranceY.M -noRd -noWr -verb             \       Specifies experiment dimensionality and acquisition method
| pipe2xyz -out proc/data%03d.fid -verb -ov                                    Applies a macro for processing
                                                                               Splits the 3D data into individual 2D planes saved as numbered files
xyz2pipe -in proc/data%03d.fid -x                    \                         Takes the split 2D planes and prepares them for processing along the X (direct) dimension
| nmrPipe -fn SOL  -mode 1 -fl 4 -fs 2          \                             Applies solvent suppression to remove solvent artifacts
| nmrPipe  -fn SP -off 0.45 -end 0.98 -pow 2 -c 1.0   \                       Sine bell apodization
| nmrPipe  -fn ZF -auto                               \                       Automatically zero-fills the data to the next power of 2
| nmrPipe  -fn FT -auto                               \                       Fast Fourier Transform (FTT) to convert from time domain to frequency domain
| nmrPipe  -fn PS -p0 -123.6 -p1 0.0 -di              \                       Applies phase correction
| nmrPipe -fn EXT -x1 5.5ppm -xn 11.0ppm -sw       \                          Extracts a specific region from 5.5 to 11.0 ppm, maintaining spectral width information
| pipe2xyz -ov -out proc/data%03d.ft1 -z                                      Saves the X-processed data as new files

parallel -j 100% 'csh /Applications/Darwin/tools/ist.csh {} 2> /dev/null; echo {}' ::: proc/   Runs the Iterative Soft Thresholding (IST)
data*.ft1                                                                                       reconstruction algorithm on all data files in parallel

xyz2pipe -in proc/data%03d.phf                       \                         Takes the reconstructed data files and prepares for Y-dimension processing
| phf2pipe -user 1 -xproj xz.ft1 -yproj yz.ft1      \                         Converts from phf format and generates projection files for analysis
| pipe2xyz -verb -ov -out proc/test%03d.ft1                                   Save intermediate results


xyz2pipe -in proc/test%03d.ft1 -x                    \                         Reads the test files and sets up for processing along the Y dimension
| nmrPipe  -fn SP -off 0.5 -end 0.98 -pow 2 -c 0.5   \                         Sine bell apodization for Y dimension
| nmrPipe  -fn ZF -auto                              \                         Zero-fills the Y dimension data
| nmrPipe  -fn FT -verb  -neg                       \                         Fourier Transform with negation
| nmrPipe  -fn PS -p0 0 -p1 0.0 -di                 \                         Phase correction for Y dimension
| nmrPipe  -fn TP                                   \                         Transposes the data
| nmrPipe  -fn SP -off 0.5 -end 0.98 -pow 2 -c 0.5   \                        Second sine bell apodization
| nmrPipe  -fn ZF -auto                              \                        Zero-fills after transposition
| nmrPipe  -fn FT -verb -alt                         \                        Performs FFT with alternating sign correction
| nmrPipe  -fn PS -p0 -5.2 -p1 0 -di                 \                        Final phase correction
| nmrPipe  -fn POLY -auto -ord 0                     \                        Applies automatic polynomial baseline correction
| pipe2xyz -ov -out final.ft3 -z                                             Final save of processed data

xyz2pipe -in final.ft3                    \
| nmrPipe -fn ZTP                         \                                  Saves the transposed version as ft.ft3
| pipe2xyz -ov -out ft.ft3

xyz2pipe -in final.ft3                    \
| nmrPipe -fn ZTP \                                                          Converts and saves the data in NMRView format (.nv)
| nmrPipe -fn TP \                                                           for visualization and analysis
| pipe2xyz  -nv -out hncacb.nv


xyz2pipe -in proc/final%03d.ft3          \
| nmrPipe -fn ZTP \                                                          Creates the final output file in NMRPipe format (.pipe)
| nmrPipe -fn TP \
| pipe2xyz   -out hncacb.pipe
```

Figure S1. Bruker 3D NMR processing script. HNCACB processing script with the function and purpose of each section of the script. The final result of the processing script is the output of files that are used for NMR analysis, such as .pipe and .nv.